TU Delft

Delft University of Technology

Document Version
Final published version

Licence
Dutch Copyright Act (Article 25fa)

Citation (APA)
Kim, J., Kim, C. H., Hollmann, F., & Park, C. B. (2026). Principles, Materials, and Devices for Solar-to-Chemical Biotransformation. *Chemical Reviews*, *126*(8), 4857-4899. https://doi.org/10.1021/acs.chemrev.5c01010

Important note
To cite this publication, please use the final published version (if applicable).
Please check the document version above.

Copyright
In case the licence states “Dutch Copyright Act (Article 25fa)”, this publication was made available Green Open Access via the TU Delft Institutional Repository pursuant to Dutch Copyright Act (Article 25fa, the Taverne amendment). This provision does not affect copyright ownership.
Unless copyright is transferred by contract or statute, it remains with the copyright holder.

Sharing and reuse
Other than for strictly personal use, it is not permitted to download, forward or distribute the text or part of it, without the consent of the author(s) and/or copyright holder(s), unless the work is under an open content license such as Creative Commons.

Takedown policy
Please contact us and provide details if you believe this document breaches copyrights.
We will remove access to the work immediately and investigate your claim.

This work is downloaded from Delft University of Technology.

CHEMICAL REVIEWS

pubs.acs.org/CR

Review

Principles, Materials, and Devices for Solar-to-Chemical Biotransformation

Published as part of Chemical Reviews special issue "Semi-artificial Photosynthesis".

Jinhyun Kim,[#] Chang Hyun Kim,[#] Frank Hollmann,[*] and Chan Beum Park[*]

Cite This: *Chem. Rev.* 2026, 126, 4857−4899

Read Online

ACCESS | Metrics & More | Article Recommendations

ABSTRACT: Biosolar conversion harnesses the complementary advantages of photo(electro)catalysis and redox biocatalysis to synthesize fuels and high-value compounds under sunlight. By routing renewable energy inputs through photo(electro)catalytic interfaces to biocatalysts, nature-inspired biosolar systems achieve highly selective and low-carbon chemical synthesis. This integration transcends the intrinsic limits of purely (in)organic or biological catalysis, advancing the frontier of next-generation sustainable chemical synthesis. Here, we introduce a comprehensive conceptual framework for solar-driven biocatalytic devices by elucidating their core mechanisms and thermodynamic foundations across photocatalytic, photoelectrocatalytic, and photovoltaic-photoelectrocatalytic platforms. We further highlight breakthroughs in the design of photobiocatalytic materials and devices, contextualized within coenzyme/mediator recycling, direct electron transfer, and H_2O_2 generation. Finally, we outline future directions toward practical and sustainable biosolar catalysis.

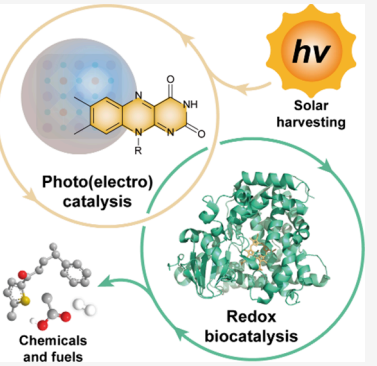

CONTENTS

1. Introduction 4858
2. Mechanisms and Thermodynamics of Photobiocatalysis 4858
 2.1. Components of Photobiocatalysis 4858
 2.2. Charge Flow from Abiotic Catalysts to Biological Catalysts 4859
 2.3. Photocatalysts for Biocatalysis 4860
  2.3.1. Semiconducting Photocatalysts 4860
  2.3.2. Molecular Photocatalysts 4861
 2.4. Photoelectrocatalysis for Biocatalysis 4862
  2.4.1. Principles for Photoelectrochemically Driven Biotransformation 4862
  2.4.2. Device Architectures of Biocatalytic Photoelectrochemical Synthesis 4863
3. Performance Indexes for Biosolar Catalysis 4864
 3.1. Solar-to-Chemical Conversion Efficiency 4865
 3.2. Current and Current Density 4865
 3.3. Faradaic Efficiency 4865
 3.4. Partial Current and Partial Current Density 4865
 3.5. Turnover Frequency 4865
 3.6. Total Turnover Number 4866
 3.7. Turnover Number 4866
 3.8. Product Yield and Conversion Yield 4866
 3.9. Reaction Selectivity 4866
 3.10. Enantiomeric Excess 4866
4. Photocatalytic Enzyme Activation for Sustainable Biosynthesis 4866
 4.1. Mediated Electron Transfer in Abiotic−Biotic Systems 4866
  4.1.1. Nicotinamide Coenzyme Regeneration 4867
  4.1.2. Flavin Coenzyme Recycling 4871
  4.1.3. Redox Cycling of Viologen Mediators 4871
 4.2. Direct Electron Transfer Across Abiotic−Biotic Interfaces 4871
  4.2.1. Material Coupling with Metalloenzymes 4872
  4.2.2. Photoactivation of Flavin Prosthetic Groups 4873
  4.2.3. Electronic Coupling at Material−Bacteria Interfaces 4873
 4.3. Peroxide-Driven Biocatalysis through Photocatalytic H_2O_2 Provision 4876
5. Photoelectrocatalytic System for Redox Biotransformation 4877
 5.1. Mediated Charge Coupling of Abiotic Materials with Biocatalysts 4877
  5.1.1. Photoelectrocatalytic Regeneration of Nicotinamide Coenzymes 4877

Received: November 24, 2025
Revised: March 16, 2026
Accepted: March 18, 2026
Published: April 7, 2026



Downloaded via TU DELFT on May 19, 2026 at 09:51:05 (UTC).
See https://pubs.acs.org/sharingguidelines for options on how to legitimately share published articles.

© 2026 American Chemical Society

5.1.2. Photoelectrocatalytic Recycling of Flavin Coenzymes 4878
5.1.3. Photoelectrocatalytic Rejuvenation of Viologen Mediators 4879
5.2. Photoelectrocatalytic Devices for Direct Activation of Biocatalysts 4879
5.2.1. Photoactivation of Metalloenzymes 4879
5.2.2. Photoelectrochemical Transfer of Electrons to Bacteria 4880
5.3. H_2O_2-Mediated Biocatalysis Enabled by Biosolar Devices 4881
6. Conclusions and Outlook 4882
6.1. Broad-Spectrum Solar Energy Capture and Efficient Charge Transfer 4882
6.2. Tailoring Material-Enzyme Interface for Electron Transfer 4883
6.3. Shielding Redox Biocatalysts from Abiotic Photodamage 4883
6.4. Enhancing Photo(electro)catalyst Stability in Biosolar Devices 4883
6.5. Device-Level Development for Practical Biosolar Conversion 4884
Author Information 4885
Corresponding Authors 4885
Authors 4885
Author Contributions 4885
Notes 4885
Biographies 4885
Acknowledgments 4885
Abbreviations 4885
References 4886

1. INTRODUCTION

Biosolar catalysis—synonymous with photobiocatalysis—refers to solar-driven activation of redox biocatalytic processes. Redox biocatalysts (or oxidoreductases) are emerging alternatives to common catalytic systems for organic synthesis.[1−3] Oxidoreductases enable synthetically valuable molecular transformations (e.g., asymmetric reduction of C═C bonds,[3,4] oxygenation of C−H bonds,[5] Baeyer−Villiger oxidation[6]) and fuel-forming reactions (e.g., CO_2 reduction to formate,[7−10] H_2 evolution[11]) with exceptional selectivity under mild conditions. The high selectivity of oxidoreductase-catalyzed transformation stems from the well-defined three-dimensional architecture of enzyme active sites, which enables precise substrate positioning and thereby affords exceptional selectivity and rate acceleration at levels unachievable by traditional catalysis.

Recent advances have expanded the operational landscape of redox biocatalysis through its integration with abiotic energy transduction systems. Various physical energy inputs, including ultrasound,[12] low-grade heat,[13] electrical currents,[14,15] and electromagnetic radiation[16−19] have been applied to promote biocatalytic redox reactions by providing the necessary redox equivalents. In the context of the transition of energy to renewable energy sources, sunlight-assisted catalytic platforms have garnered particular attention. The practicality of biosolar platforms has been demonstrated recently as integrated devices that harness solar energy across broad spectral ranges to synthesize enzymatic products with higher energy conversion efficiency.[20−22]

This Review provides a panoramic overview of state-of-the-art advances in the development of photocatalytic and photoelectrocatalytic materials and platforms for the activation of redox enzymes, as depicted in Figure 1. Within the broader context of solar-to-chemical conversion, we distill the fundamental mechanistic and thermodynamic principles, as well as the performance metrics, underlying the operation of photocatalytic, photoelectrocatalytic, and photovoltaic-photoelectrocatalytic devices. Here, photovoltaic-photoelectrocatalytic refers to photovoltaic-assisted photoelectrochemical tandems for solar-to-chemical biotransformation; biophotovoltaics[23,24] aimed at light-to-electricity generation are outside the scope of this review. The discussion is organized around three orthogonal mechanistic axes: (i) mediated electron transfer between abiotic materials and biological catalysts; (ii) direct electron transfer (DET) to redox moieties of oxidoreductases; and (iii) peroxide-mediated biocatalysis enabled by solar-driven H_2O_2 generation. We conclude by delineating material- and device-centric research avenues aimed at enhancing the catalytic activity, biocompatibility, and operational robustness in biosolar technologies. The main focus of this contribution is the interface between photochemical energy input and redox biocatalysis. Light-triggered noncanonical catalysis of cofactor-dependent enzymes, as well as photoenzyme- and cyanobacteria-based systems, also fall within the broader concept of photobiocatalysis but are beyond the scope of this review. The interested reader is referred to several excellent recent reviews on these topics. Likewise, approaches in which photochemical steps generate substrates for enzymatic reactions or further transform enzymatic products are not discussed here.

2. MECHANISMS AND THERMODYNAMICS OF PHOTOBIOCATALYSIS

2.1. Components of Photobiocatalysis

Photobiocatalytic platforms rely on the interplay of four key components to facilitate biotransformation (Figure 2a):

(i) Photoactive catalyst, including particulate semiconductors (Figure 2b), semiconducting photoelectrodes, molecular dyes, or photovoltaic-integrated conductive electrodes. The photocatalyst modulates (regenerates) the biocatalyst's redox state through electron transfer processes. However, abiotic photoactive materials cannot provide the substrate recognition and stereochemical control that arise from enzyme active sites. Consequently, the selective bond transformations cannot be achieved by abiotic photocatalysis alone with comparable selectivity under mild, aqueous conditions;
(ii) Electron donor or acceptor, which regenerates the ground-state of the photocatalyst, thereby enabling catalytic turnover (Figure 2c);
(iii) Oxidoreductase enzyme that catalyzes the selective transformation of interest. Oxidoreductases contain a cofactor (coenzyme or prosthetic group) that performs the redox reaction, and a polypeptide scaffold that accelerates the process and imparts selectivity;
(iv) Mediators shuttling electrons between the photocatalyst and the redox-active biocatalyst (Figure 2d).

When the photocatalyst and oxidoreductase can communicate electrochemically, DET is possible (Figure 2a). This is typically observed when the prosthetic group [e.g., heme cofactors in cytochrome P450s (CYP), flavins in ene-reductases, tungsten clusters in formate dehydrogenases

https://doi.org/10.1021/acs.chemrev.5c01010
Chem. Rev. 2026, 126, 4857−4899

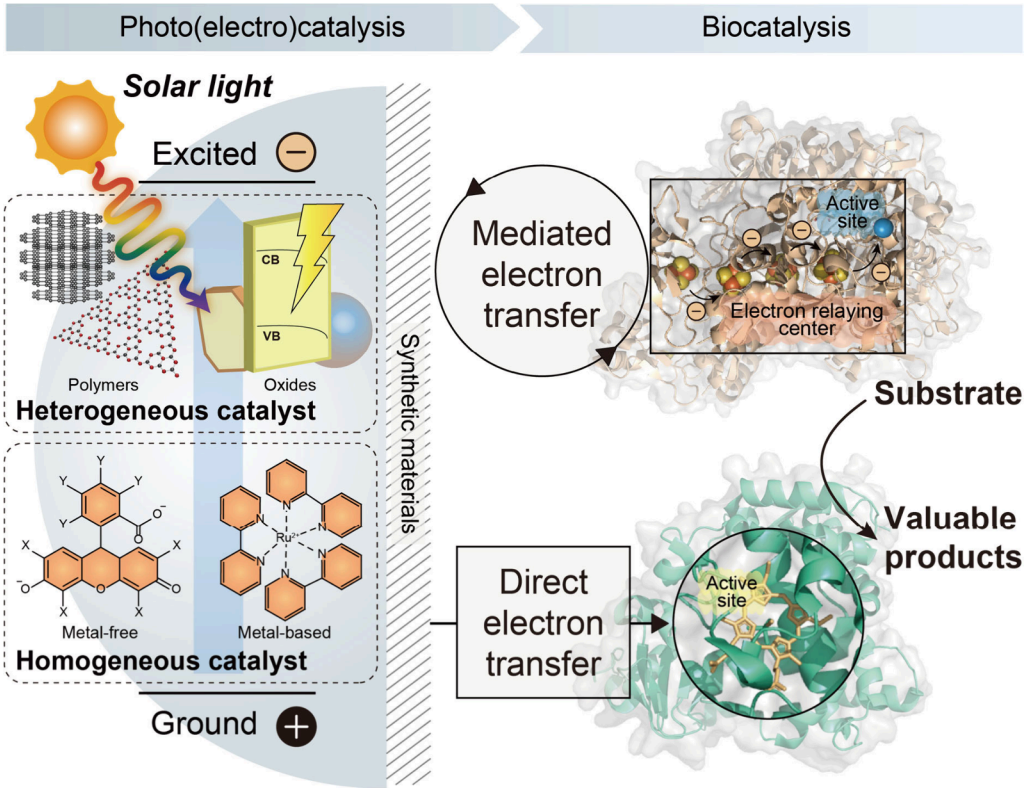

Figure 1. Conceptual overview of biocatalytic artificial photosynthesis. Biohybrid photosynthesis enables solar-to-chemical biotransformation by integrating abiotic photo(electro)catalysis and redox biocatalysis. Heterogeneous and homogeneous photo(electro)catalysts harvest solar light to excite electrons from a ground state to an excited state. The excited charge carriers activate oxidoreductases via mediated or direct electron transfer pathways, enabling the synthesis of valuable chemicals and fuels. Abbreviations: CB, conduction band; VB, valence band.

(FDH)] is surface-exposed or when electron-relay domains (e.g., [FeFe] clusters in hydrogenases (H_2ase),[25,26] [NiFe] clusters in H_2ase[17,27−34]) provide an electrical connection between the prosthetic group and the surface. In most cases, however, the insulating polypeptide shell hinders efficient electron transfer between the photocatalyst and the redox-active prosthetic group. Under such conditions, low-molecular-weight mediators are required to enable electron flow. This approach, known as mediated electron transfer (Figure 2a), employs natural mediators (e.g., nicotinamide or flavin coenzymes) as well as synthetic ones such as viologens or metallocenes.[7−9,35,36]

2.2. Charge Flow from Abiotic Catalysts to Biological Catalysts

Upon light absorption, photoactive materials undergo electronic excitation, resulting in the generation of high-energy electrons and corresponding holes (Figure 2a; a detailed discussion of their thermodynamic mechanisms is provided in the following subsection). These excited charge carriers are transferred to nearby electron acceptors or donors.[37] Such charge transfer initiates directional electron flow that is essential for driving biological catalysis.[38,39]

Depending on the redox directionality, solar-driven catalytic platforms can facilitate either reductive or oxidative enzymatic transformations. When photoexcited electrons are injected into the prosthetic groups of redox enzymes, this can drive not only reductive biotransformations such as asymmetric hydrogenation, reductive amination, and CO_2 fixation but also oxyfunctionalization reactions, since monooxygenases rely on the reductive activation of molecular oxygen. Alternatively, these electrons can be consumed to reduce soluble redox mediators, thereby generating their enzymatically active reduced forms (Figure 2d). These reduced species then serve as essential electron donors for downstream enzymatic processes. In parallel, the oxidized photocatalyst must be regenerated to sustain cyclic operation. This regeneration is achieved by introducing an electron donor that donates electrons to the oxidized photocatalyst. A wide variety of electron donors have been reported, including water, tertiary amines [e.g., triethanolamine (TEOA), ethylenediaminetetraacetic acid (EDTA)], short-chain alcohols (e.g., methanol, ethanol), thiol-containing reductants (e.g., dithiothreitol), and renewable biomass sources (e.g., glucose, lignocellulose) (Figure 2c). Although water represents most attractive electron donor from the environmental and sustainability perspective, its use in biosolar systems remains challenging due to the sluggish kinetics of the four-electron water oxidation reaction and substantial overpotentials.[40] Actually, no single electron donor is universally optimal. Rather, donor selection should be guided by (i) sufficient driving force to reduce the oxidized photocatalyst and suppress back electron transfer, (ii) fast kinetics of donor oxidation (or hole scavenging) relative to charge recombination, and (iii) specific donor−photocatalyst interfacial interactions that can accelerate—or inhibit—charge transfer.[41,42] Given this multifactorial dependence, identifying a suitable electron donor often relies on empirical screening and optimization under the target reaction conditions.

Conversely, for oxidative biocatalysis, photoexcited holes act as potent oxidizing agents. These holes can directly oxidize enzymatically relevant species (e.g., reduced nicotinamide

https://doi.org/10.1021/acs.chemrev.5c01010
Chem. Rev. 2026, 126, 4857−4899

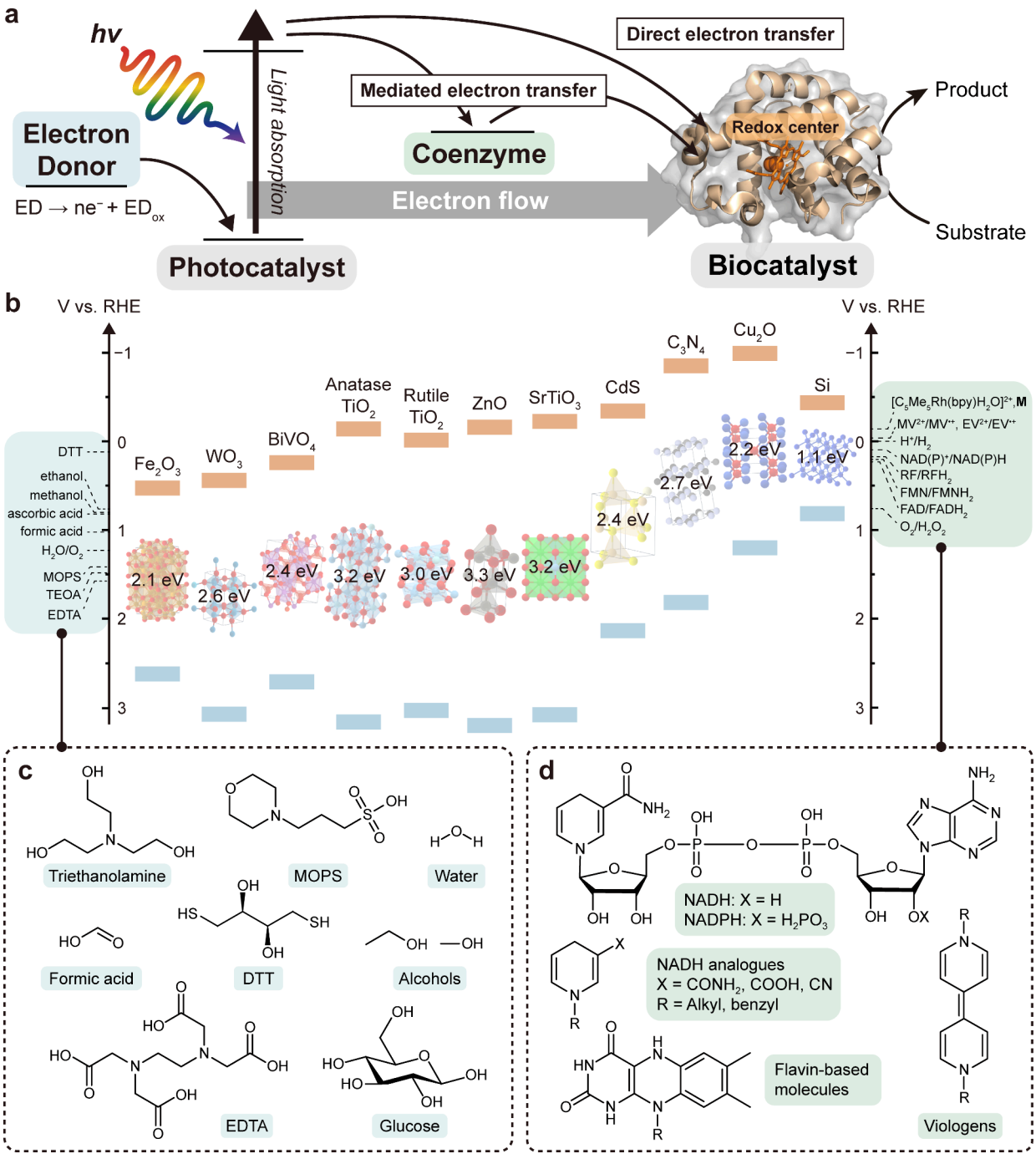

Figure 2. Components of photoexcited electron transfer for oxidoreductase activation. (**a**) Mediated or direct electron transfer to redox biocatalysts by solar-powered devices. Photocatalysts transfer excited electrons to redox biocatalysts either directly or via redox mediators, and electron donors concurrently compensate for the remaining holes to maintain charge balance. (**b**) Band-edge positions of representative semiconductors and thermodynamic redox potentials of electron donors, redox coenzymes, and artificial mediators. The chemical structures of representative (**c**) electron donors and (**d**) coenzymes and mediators. Abbreviations: ED, electron donor; ED_{ox}, oxidized electron donor; MOPS, 3-(*N*-morpholino)propanesulfonic acid; DTT, DL-dithiothreitol; EDTA, ethylenediaminetetraacetic acid; MV, methyl viologen; EV, ethyl viologen; RF, riboflavin; FMN, flavin mononucleotide; FAD, flavin adenine dinucleotide.

coenzymes), converting them into the oxidized forms required for oxidative enzymatic reactions (e.g., alcohol dehydrogenation). To regenerate the photocatalyst, a sacrificial electron acceptor (e.g., molecular oxygen) is introduced to capture the photogenerated electrons. This transfer of electrons to the electron acceptor completes the photoredox cycle and ensures sustained catalytic turnover under continuous light exposure.

2.3. Photocatalysts for Biocatalysis

2.3.1. Semiconducting Photocatalysts. Semiconductor particulates serve as diffusing photocatalysts capable of driving light-activated biological synthesis. Their thermodynamic behavior is governed by the interplay between the material's electronic band structure and the redox potentials of the reactants and products involved in the target reactions. Under illumination with photons of energy ≥ bandgap (E_g), electrons

https://doi.org/10.1021/acs.chemrev.5c01010
Chem. Rev. 2026, 126, 4857−4899

are excited from the valence band (VB) to the conduction band (CB), generating mobile charge carriers (Figure 3a). This photoexcitation process requires spectral alignment between the semiconductor's absorption profile and the solar spectrum. The E_g determines the absorption threshold wavelength according to $\lambda \leq 1240/E_g$ (for λ in nm and E_g in eV), where 1240 is derived from Planck's constant (h), the speed of light (c), and the elementary charge (e) (i.e., 1240 = hc/e).

Under steady-state illumination, photogenerated electrons and holes accumulate in their respective bands, leading to a nonequilibrium distribution of charge carriers. As a result, distinct quasi-Fermi levels are established: $E_{qF,electron}$ near the CB for electrons and $E_{qF,hole}$ near the VB for holes (Figure 3a). These quasi-Fermi levels define the electrochemical potentials of the charge carriers and are critical parameters in determining the driving force for photobiocatalytic reactions. At equilibrium (i.e., in the dark), a single Fermi level (E_F), located within the bandgap, characterizes the system. Illumination decouples this equilibrium, splitting the quasi-Fermi levels ($E_{qF,electron} - E_{qF,hole}$), which directly correlates with the maximum achievable photovoltage (V_{ph}) and the thermodynamic voltage (V_{th}) available for redox reactions.

For productive interfacial electron transfer to occur, $E_{qF,electron}$ must lie at a more negative potential than the reduction potential of the electron acceptor (e.g., molecular oxygen, oxidized coenzymes), while $E_{qF,hole}$ must be more positive than the oxidation potential of the electron donor (e.g., TEOA, EDTA, water) (Figure 3a). Failure to meet these conditions results in inefficient charge utilization, with charge recombination (either radiative or nonradiative) dominating over catalytic processes. Such recombination events dissipate the absorbed photon energy as heat or light, reducing the overall quantum efficiency.

Direct measurement of the quasi-Fermi levels remains challenging due to their dependence on light intensity, carrier density, and surface kinetics. As a result, the CB minimum (E_{CB}) and VB maximum (E_{VB}) are used as thermodynamic surrogates to evaluate the redox feasibility. For a redox reaction to be thermodynamically favorable, E_{CB} must be more negative than the standard reduction potential of the target acceptor, and E_{VB} must be more positive than the oxidation potential of the donor (Figure 3a). This approximation is supported by the Boltzmann-based relations (eqs 1 and 2):

$$E_{qF,\mathrm{electron}} \approx E_{CB} + kT\ln\left(\frac{n}{N_C}\right) \quad (1)$$

$$E_{qF,\mathrm{hole}} \approx E_{VB} - kT\ln\left(\frac{p}{N_V}\right) \quad (2)$$

where k is the Boltzmann constant (8.617×10^{-5} eV K^{-1}), T is the absolute temperature (K), n and p are the free carrier concentrations of electrons and holes, and N_C and N_V are the effective density of states in the CB and VB, respectively. These expressions quantify the energetic positioning of the quasi-Fermi levels relative to the band edges, thereby enabling estimation of the available photodriving force for redox processes under illumination.

2.3.2. Molecular Photocatalysts. Molecular photocatalysts (e.g., transition metal complexes, porphyrins, xanthene derivatives, flavins) operate through discrete frontier molecular orbitals, namely, the highest occupied molecular orbital (HOMO) and lowest unoccupied molecular orbital (LUMO). Unlike semiconductors, which exhibit extended electronic band structures, these systems rely on well-defined molecular orbitals to mediate localized electronic transitions. Upon absorption of a photon with energy equal to or greater than the energy gap between HOMO and LUMO ($E_{HOMO-LUMO}$), the molecular photocatalyst undergoes electronic excitation from the singlet ground state (S_0) to a higher excited singlet state (S_n), which rapidly relaxes to the lowest singlet excited state (S_1) through internal conversion accompanied by vibrational relaxation (Figure 3b).[43] From this S_1 state, the catalyst either almost instantaneously returns to the ground state via fluorescence or nonradiative decay, or undergoes intersystem crossing to the triplet excited state (T_1) which returns to S_0 via phosphorescence. Both S_1 and T_1 are the most likely excited states to participate in photoinduced electron transfer (PET) (Figure 3b).

Upon photoexcitation, the redox properties of a photocatalyst change dramatically, facilitating reactions that are thermodynamically inaccessible from the ground state. The excited state simultaneously becomes a much stronger oxidant and reductant than the ground state. This redox modulation enables the activation of substrates whose redox potentials fall outside the operating window of ground-state catalysis.

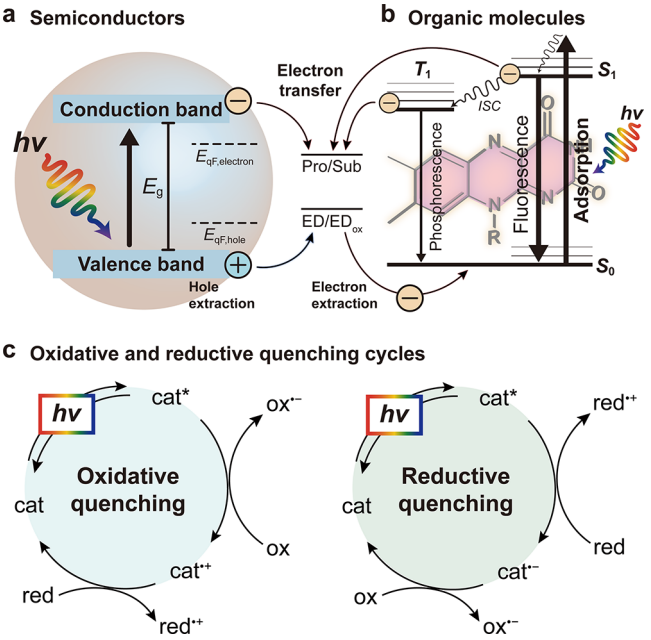

Figure 3. Photocatalytic principles for redox biocatalysis. (**a**) Semiconductors with energy band structures and (**b**) molecules with discrete frontier orbitals. In semiconductor photocatalysts, light absorption promotes electrons from the valence band to the conduction band across the bandgap (E_g), generating electron–hole pairs. The resulting quasi-Fermi levels of electrons and holes ($E_{qF,electron}$ and $E_{qF,hole}$) dictate the reducing and oxidizing power of the system. In molecular systems, excitation from the singlet ground state (S_0), typically involving an electron promotion from the highest occupied molecular orbital to the lowest unoccupied molecular orbital, generates singlet (S_1) or triplet (T_1) excited states with altered redox potentials, thereby enabling photoredox reactions. (**c**) Oxidative and reductive quenching cycles of photoredox catalysts. Abbreviations: Pro, product; Sub, substrate; ED, electron donor; ED$_{ox}$, oxidized electron donor; ISC, intersystem crossing; cat, photoredox catalyst; cat*, excited state of cat; ox, oxidant; red, reductant.

https://doi.org/10.1021/acs.chemrev.5c01010
Chem. Rev. 2026, 126, 4857−4899

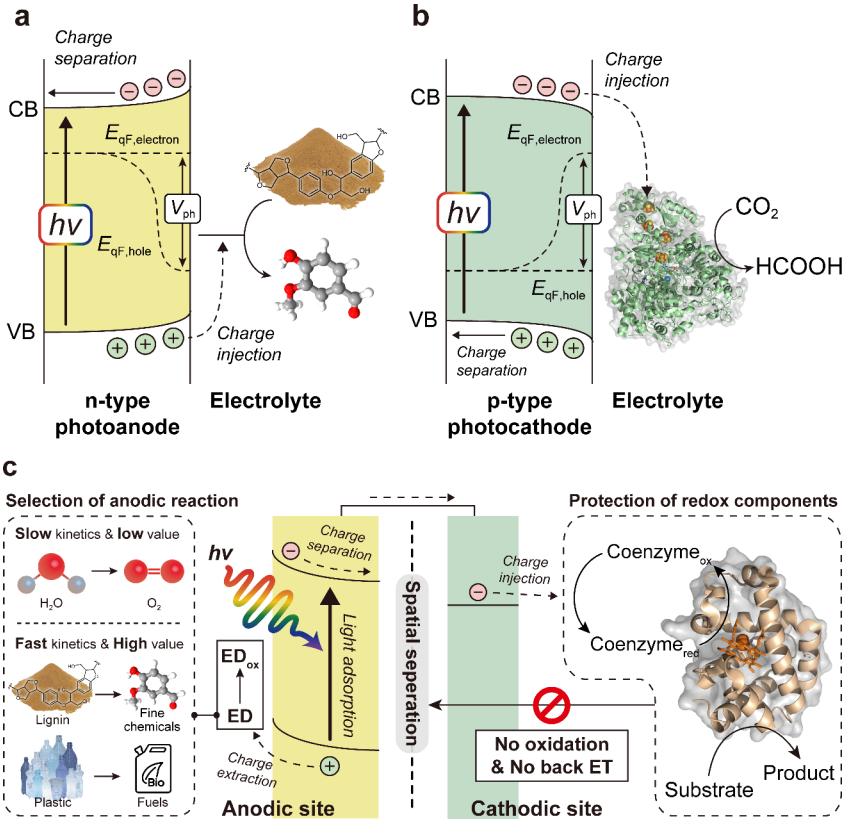

Figure 4. Principles and features of photoelectrocatalytic devices for oxidoreductase activation. Charge transfer mechanisms of (**a**) n-type photoanodes and (**b**) p-type photocathodes for photoelectrochemical redox catalysis. Band bending promotes the minor carriers toward the interface. Photovoltage (V_{ph}) and external bias shift the quasi-Fermi levels to values exceeding the redox potentials of the target half-reactions, thereby enabling thermodynamically favorable charge transfer. (**c**) Photoelectrocatalytic platforms with spatial and energetic separation of oxidation and reduction reactions. This configuration minimizes back electron transfer and protects redox components by physically isolating the biocatalytic site from oxidative species. Abbreviations: CB, conduction band; VB, valence band; ED, electron donor; ED_{ox}, oxidized electron donor.

Two major mechanistic modes are considered in PET: reductive quenching and oxidative quenching (Figure 3c).[43] In reductive quenching, the excited-state catalyst (cat*) acts as an electron acceptor, being reduced by a ground-state donor substrate (sub, for example, TEOA) (Figure 3c). The associated Gibbs free energy change is expressed as eq 3:[43]

$$\Delta G = -F(E^*_{red}(cat^*/cat^-) - E_{ox}(sub^+/sub)) \quad (3)$$

where $E^*_{red}(cat^*/cat^-)$ is the excited-state reduction potential of the catalyst, which can be estimated by eq 4:

$$E^*_{red}(cat^*/cat^-) = E_{red}(cat/cat^-) + E_{0,0} \quad (4)$$

where $E_{0,0}$ is the zero−zero transition energy (in unit of V), and F is the Faraday constant (96,485 C mol^{-1}) used to convert volts to free energy in electron volts or kilojoules. In contrast, oxidative quenching involves oxidation of the excited photocatalyst (cat*) by donating an electron to a substrate (e.g., flavin cofactor), which is thereby reduced (Figure 3c). The corresponding thermodynamic driving force is expressed in eq 5:

$$\Delta G = -F(E_{red}(sub/sub^-) - E^*_{ox}(cat^+/cat^*)) \quad (5)$$

The excited-state oxidation potential is given in eq 6:

$$E^*_{ox}(cat^+/cat^*) = E_{ox}(cat^+/cat) - E_{0,0} \quad (6)$$

These formulations allow for the quantitative evaluation of the driving force for PET, and thus for assessing whether a given catalyst−substrate pair is thermodynamically competent for photoredox chemistry. Productive PET for biocatalysis requires that the substrate's redox potential lies within the excited-state redox window defined by the catalyst. If this condition is not met, charge recombination pathways (e.g., nonradiative relaxation, fluorescence) or back electron transfer will dominate.

Unlike the semiconductor photocatalysis, quasi-Fermi levels are not commonly applied to molecular systems because their discrete electronic structures lack the delocalized band continuum needed to define the Fermi-level-related concepts. However, the analogy can be made in that the excited-state redox potentials serve an equivalent role: they represent the effective electrochemical potentials of the charge carriers under illumination and thereby constitute the thermodynamic driving force for photoredox transformations.

2.4. Photoelectrocatalysis for Biocatalysis

2.4.1. Principles for Photoelectrochemically Driven Biotransformation. Photoelectrocatalytic systems offer an alternative to photocatalytic systems for the activation of biocatalysts by using dual energy inputs: solar and electrical energies. When a semiconductor photoelectrode is immersed in an electrolyte, the absorption of photons with energy greater than (or equal to) the E_g generates electron−hole pairs. These charge carriers are subsequently separated by the built-in electric field at the semiconductor|electrolyte interface, which directs their transport toward energetically favorable regions.[44]

https://doi.org/10.1021/acs.chemrev.5c01010
Chem. Rev. 2026, 126, 4857−4899

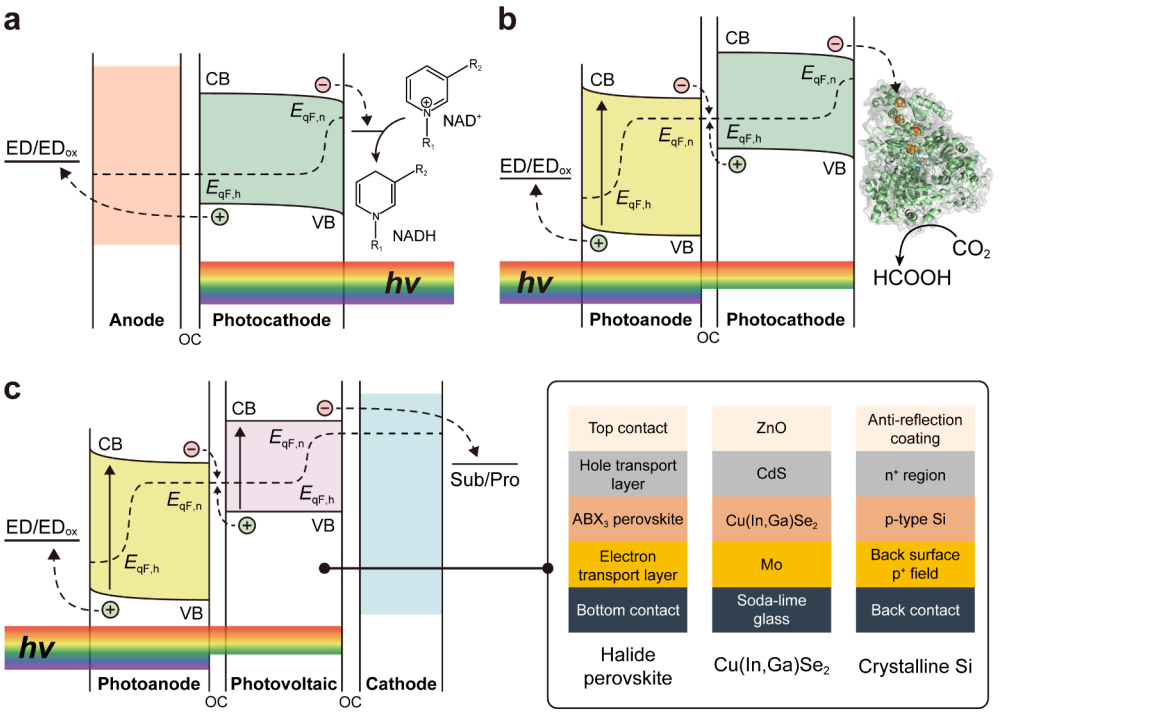

Figure 5. Architecture of biocatalytic photoelectrochemical devices. (**a**) Single light-absorber systems driven by photocathodes. An illuminated photocathode drives reductive processes, whereas a dark anode oxidizes electron donors. Dual light-absorber (**b**) photoelectrocatalytic and (**c**) photovoltaic-photoelectrocatalytic tandem devices for unbiased solar-to-chemical conversion. These systems utilize two light absorbers to generate sufficient photovoltage for unbiased redox biotransformation. The architectures in the outlined box represent structures of photovoltaic modules (e.g., halide perovskites, Cu(In,Ga)Se_2, and crystalline Si). Abbreviations: ED, electron donor; ED_{ox}, oxidized electron donor; OC, ohmic contact; CB, conduction band; VB, valence band; $E_{qF,h}$, quasi-Fermi level of holes; $E_{qF,n}$, quasi-Fermi level of electrons.

In n-type materials (e.g., TiO_2, Fe_2O_3, $BiVO_4$, WO_3),[45−49] upward band bending directs photoexcited holes toward the semiconductor surface,[50,51] facilitating oxidative reactions (e.g., electron extraction from electron donor) (Figure 4a). Conversely, in p-type semiconductors (e.g., Cu_2O, CuO, boron-doped Si),[52−57] downward band-bending drives electrons toward the interface,[50,51] enabling reductive processes (e.g., coenzyme regeneration, transfer of electrons to electron-relay center) (Figure 4b). This fundamental distinction underpins the use of n-type semiconductors as photoanodes and p-type semiconductors as photocathodes. Therefore, the band bending in the space-charge region gives rise to vectorial charge transport, a precondition for selective oxidation at a photoanode or reduction at a photocathode. Application of an anodic (positive) bias to an n-type photoanode increases the extent of band bending and enhances hole extraction, whereas a cathodic (negative) bias on a p-type photocathode facilitates electron extraction by steepening the downward band bending.[44]

Similar to photocatalytic systems (see details in Section 2.3), successful redox biocatalysis in photoelectrocatalytic platforms requires that the $E_{qF,electron}$ and $E_{qF,hole}$ appropriately align with the redox potentials of the respective half-reactions.[58] Specifically, for oxidation reactions, $E_{qF,hole}$ must be more positive than the oxidation potential of the electron donor (e.g., water, TEOA, or biomass) (Figure 4a). Conversely, $E_{qF,electron}$ must be more negative than the reduction potential of the electron acceptor (e.g., cofactors, electron relay proteins) (Figure 4b). A key advantage of photoelectrocatalytic systems over photocatalytic systems lies in the tunability of E_{qF} via external electrical bias, which enables more precise control to meet the thermodynamic requirements of targeted redox reactions. Illumination generates V_{ph} (= $|E_{qF,electron} - E_{qF,hole}|$), arising from the redistribution of minority carriers in the photoelectrodes. The overall V_{ph} of photoelectrocatalytic devices equals the sum of the individual V_{ph} of each photoelectrode. The total driving force for a reaction is the combination of V_{ph} and electrical bias, which must exceed the sum of V_{th} and the overpotentials associated with the reaction.

Another distinctive feature of photoelectrocatalytic systems is the spatial separation of the oxidation and reduction reactions (Figure 4c). Because charge carriers migrate through an external circuit connecting photoanode and photocathode, the two half-reactions can be physically isolated. Although photoelectrocatalytic cells can be constructed in a single-compartment configuration housing both electrodes, two-compartment systems—separated by an ion-exchange membrane or salt bridge—are frequently employed. Such spatial separation offers several advantages: (i) prevention of unwanted reoxidation of reduced coenzymes or mediators by the photoanode; (ii) suppression of the migration of reactive oxygen species that can damage enzymes; and (iii) independent optimization of the electrolyte conditions (e.g., pH, ionic strength) for each half-reaction to maximize catalytic performance.

2.4.2. Device Architectures of Biocatalytic Photoelectrochemical Synthesis. Photoelectrocatalytic devices can be configured in three canonical ways, each balancing light absorption, photovoltage generation, and catalytic compatibility: (i) single-photoelectrode assembly (i.e., photoanode|cathode or anode|photocathode), (ii) dual-photoelectrode systems (i.e., photoanode|photocathode), and (iii)

https://doi.org/10.1021/acs.chemrev.5c01010
Chem. Rev. 2026, 126, 4857−4899

Table 1. Comparative Analysis of Solar-to-Chemical Conversion Efficiencies between Natural and Semiartificial Photosynthesis

System	Photoactive material	Biocatalyst	Light source	Product	Solar-to-chemical conversion efficiency	ref.
Natural photosynthesis	Chlorophylls	Rubisco	Natural sunlight	Carbohydrate (C_3 cycle)	2.9%	100
		Rubisco, malic enzyme, phosphoenolpyruvate carboxykinase		Carbohydrate (C_4 cycle)	4.2%	
Semiartificial photosynthesis	CoPi/PV/Co−P	*Ralstonia eutropha*	Not reported	Biomass	9.7%	104
				Bioplastic	7.6%	
				Fusel alcohols	7.1%	
	Pt/Si PV/Si nanowire	*Sporomusa ovata*	Xe lamp (25 mW cm^{-2})	Acetate	∼3.6%	105
	TiO_2 nanowire/Si nanowire	*Sporomusa ovata*	Xe lamp (100 mW cm^{-2})	Acetate	0.38%	106
	$BiVO_4$/Perovskite/IO-TiO_2	FDH from *Desulfovibrio vulgaris* Hildenborough	Simulated solar light (100 mW cm^{-2})	Formate	0.8%	107
	FeOOH/$BiVO_4$/Perovskite/3D TiN	FDH from *Clostridium ljungdahlii*	Xe lamp (λ > 420 nm, 100 mW cm^{-2})	Formate	0.08%	108
	FeOOH/$BiVO_4$/Cu(In,Ga)Se_2/mesoITO	FDH from *Thiobacillus* sp. KNK65MA	Xe lamp (λ > 400 nm, 100 mW cm^{-2})	Formate	0.03%	61
	$BiVO_4$/Perovskite/IO-TiO_2	H_2ase from *Desulfomicrobium baculatum*	Simulated solar light (100 mW cm^{-2})	Hydrogen	1.1%	109
	P_{Os}−PSII/dpp/IO-TiO_2/IO-ITO	H_2ase from *Desulfomicrobium baculatum*	Xe lamp (λ > 420 nm, 100 mW cm^{-2})	Hydrogen	0.14%	110
	InP nanoparticles	*Saccharomyces cerevisiae*	Violet LED (5.6 mW cm^{-2})	Shikimic acid	1.58%	111

photovoltaic-integrated photoelectrocatalytic tandems (e.g., photoanode|photovoltaic|cathode) (Figure 5).[21]

Single-photoelectrode assembly operates in two different mirror-image modes. In the first configuration, an n-type photoanode harvests sunlight and drives oxidation reactions (e.g., H_2O oxidation to O_2) whereas a dark conducting cathode performs cathodic reactions (e.g., electron transfer to metalloenzyme) and completes the circuit; in the other configuration, a p-type photocathode is illuminated to drive cathodic reactions and a dark anode oxidizes redox substrates in an electrolyte (Figure 5a). Because a solitary semiconductor typically delivers a V_{ph} of <1 V under Air Mass 1.5 G (AM 1.5G) illumination, an electrical bias of several hundred to thousand millivolts is usually required to span the potential gap between the oxidative and reductive half-reactions. The architecture remains electrically and mechanically simple, and the dark counter-electrode can be freely selected for catalytic compatibility. Nevertheless, because solar-to-chemical efficiency is referenced solely to the incident solar irradiance, any portion of the reaction overpotential supplied by an external bias rather than by V_{ph} directly lowers the fraction of product energy attributable to sunlight—thereby diminishing the efficiency value.

Dual-photoelectrode photoelectrocatalytic systems place a light-absorbing n-type photoanode in series with a complementary p-type photocathode so that each half-cell supplies its own V_{ph} (Figure 5b). Under steady light conditions (e.g., AM 1.5G), the photoelectrocatalytic system's V_{ph} equals the sum of two individual contributions. When this combined V_{ph} exceeds the V_{th} plus the overpotentials associated with the reaction (see details in 2.4.1), the photoelectrocatalytic device operates without an external electrical bias—a condition termed bias-free operation. In this regime the photoanode oxidizes the electron donor, and the photocathode transfers electrons for redox biosynthesis. Furthermore, the dual-absorber architecture offers spectral complementarity, because each semiconductor can be chosen to harvest a different portion of the solar spectrum.

Photovoltaic-integrated photoelectrocatalytic tandems connect a photovoltaic module (e.g., crystalline Si, halide perovskites, Cu(In,Ga)Se_2)[59−70] in series with a photoelectrocatalytic system, yielding layouts like photoanode|photovoltaic|cathode and anode|photovoltaic|photocathode (Figure 5c). The photovoltaic element adds an additional V_{ph} of 0.7 to 1.3 V, enabling bias-free operation under full-spectrum sunlight, as the combined V_{ph} from the photoelectrode and photovoltaic device[71−96] is sufficient to drive thermodynamically challenging redox reactions. This modularity broadens the palette of electrocatalytic materials to include earth-abundant metals, conductive carbons, and molecularly modified semiconductors. The trade-off is additional fabrication complexity and the need for optical coupling strategies that minimize parasitic losses within the tandem stack.

Taken together, the single-photoanode platform offers maximal simplicity but pays an energy penalty; the dual-photoelectrode approach is conceptually elegant yet photocathode materials-limited; and photovoltaic-assisted tandems provide the highest design freedom at the cost of additional fabrication steps. Selecting an architecture therefore hinges on the voltage budget of the biotransformation and the spectral overlap of the semiconductors involved.

3. PERFORMANCE INDEXES FOR BIOSOLAR CATALYSIS

The quantitative evaluation of biosolar catalytic performance requires a suite of complementary metrics, each capturing a distinct aspect of device operation, such as energy efficiency, reaction selectivity, and catalyst durability. Selection of an appropriate index should depend on the research objective—

https://doi.org/10.1021/acs.chemrev.5c01010
Chem. Rev. 2026, 126, 4857−4899

whether it is to maximize energy conversion, optimize catalytic turnover, improve selectivity, or ensure long-term stability. Ideally, multiple metrics should be reported in parallel to provide a holistic view of the system performance.

3.1. Solar-to-Chemical Conversion Efficiency

This metric evaluates the overall energy conversion performance of the system, measuring how effectively incident solar energy is stored as chemical energy in the target product (eq 7):[97,98]

$$\text{Solar-to-chemical conversion efficiency (\%)} = \frac{\Delta G \times r}{P \times A} \times 100 \quad (7)$$

where ΔG is the change in Gibbs free energy per mole of target product (J mol^{-1}), r is the production rate of the target product (mol s^{-1}), P is the incident illumination power density (W cm^{-2}), and A is the illuminated area (cm^2). Natural photosynthesis represents a highly evolved biological process for solar-to-chemical energy conversion. Through the coordinated operation of light-harvesting antenna complexes, photosystem II, photosystem I, and the Calvin−Benson cycle, solar photons drive water oxidation and CO_2 reduction to produce O_2 and energy-rich organic compounds (e.g., carbohydrates).[99] However, its solar-to-chemical conversion efficiency is rather low under typical field conditions (e.g., 2.9% for C3 plants, 4.2% for C4 plants, and 0.2−1% for many crop species)[100,101] (Table 1). This limitation suggests a system-level consequence of evolutionary optimization for survival and adaptability rather than maximal photon-to-biomass conversion.[102,103] Compared to these natural solar-to-chemical conversion efficiencies, semiartificial photosynthetic systems[104,105] have demonstrated higher performances than natural ones (Table 1),[61,104−111] which are attributed to (i) reduced energy losses along reaction pathways and (ii) broadband absorption of the solar spectrum, enabling more effective utilization of incident light.[100] Note that the solar-to-chemical efficiency quantifies energy conversion at the macroscopic level but does not reveal the underlying electrochemical processes responsible for product formation. For a deeper mechanistic understanding, current-related metrics are employed as follows.

3.2. Current and Current Density

In photoelectrochemical devices, the production rate of a target species is fundamentally governed by the Faraday's law of electrolysis, which states that the amount of substance produced or consumed at an electrode is proportional to the total charge transferred. Current is defined as the rate of electric charge flow through the electrode over time (eq 8):

$$\text{Current (A)} = \frac{\text{Total charge transferred (C)}}{\text{Elapsed time (s)}} \quad (8)$$

According to the Faraday's law, current is directly related to the rate of electrochemical reaction at the electrode surface.[112,113] Because the current increases with increasing surface area of a catalytic electrode, the current density is commonly used to describe performance, defined as eq 9:

$$\text{Current density (A cm}^{-2}\text{)} = \frac{\text{Current (A)}}{\text{Electrode area (cm}^2\text{)}} \quad (9)$$

In reporting current density, the 'geometrical' surface area of the electrode is considered rather than the 'electrochemically active' surface area; the geometrical surface area refers to the two-dimensional projected area of the electrode as seen from a top-down perspective, without accounting for surface roughness, porosity, or microscopic texture. Current (density) alone does not indicate whether the measured charge is directed toward the desired reaction. To assess the reaction-specific utilization of charge, Faradaic efficiency must be considered.

3.3. Faradaic Efficiency

Faradaic efficiency (FE) assesses the proportion of electric charge used for the intended (photo)electrochemical reaction,[114] which is calculated according to eq 10:

$$\text{FE} = \frac{n \times F \times \text{Amount of product formed (mol)}}{Q} \quad (10)$$

where n is the number of electrons transferred per molecule of product, F is Faraday's constant (96,485 C mol^{-1}), and Q is the total charge passed (C). A higher FE signifies that a greater fraction of the generated electric charge is utilized for the desired biosolar reaction, minimizing losses to side reactions and non-Faradaic processes. Partial current (density), which is a more precise descriptor of reaction-specific performance, can be derived by combining current (density) with the FE.

3.4. Partial Current and Partial Current Density

The overall current includes both the Faradaic contributions and the non-Faradaic components such as capacitive charging.[114,115] The partial current isolates the portion of the current producing the target product (eq 11):

$$\text{Partial current (A)} = \text{Current (A)} \times \text{FE} \quad (11)$$

For performance comparisons, it is common to normalize this partial current to the geometric area of the electrode, yielding a partial current density (eq 12):

$$\text{Partial current density (A cm}^{-2}\text{)} = \frac{\text{Partial current (A)}}{\text{Electrode area (cm}^2\text{)}} \quad (12)$$

Partial current (density) serves as a metric for both the activity and selectivity of a biosolar system. Whereas partial current (density) describes product formation rates in electrochemical terms, the following catalytic turnover metrics quantify reaction rates relative to the catalyst amount, which is critical in biocatalytic contexts.

3.5. Turnover Frequency

Turnover frequency (TOF) quantifies the rate at which reactants are converted into products per mole of catalyst (e.g., redox enzymes) (eq 13):[116]

$$\text{TOF (h}^{-1}\text{)} = \frac{\text{Amount of product formed (mol)}}{\text{Amount of catalyst (mol)} \times \text{Reaction time (h)}} \quad (13)$$

TOF provides a direct measure of the catalyst's activity. Because the TOF decreases over reaction time due to substrate depletion and/or catalyst degradation, the TOF is commonly measured and reported during the early stage of biosolar reactions. It is recommended that the time point at which the TOF measurement is taken. While TOFs are commonly used in chemocatalysis, the biocatalytic equivalent is the specific activity (A_{spec}) (eq 14):

https://doi.org/10.1021/acs.chemrev.5c01010
Chem. Rev. 2026, 126, 4857−4899

$$A_{spec}\ (\mathrm{U\ mg_{enzyme}^{-1}}) = \frac{\text{Amount of product formed } (\mu\text{mol})}{\text{Mass of enzyme (mg)} \times \text{Reaction time (min)}} \quad (14)$$

Both numbers are interchangeable via eqs 15 and 16:

$$\mathrm{TOF\ (h^{-1})} = \frac{A_{spec}\ (\mu\mathrm{mol\ min^{-1}\ g^{-1}}) \times M_{catalyst}\ (\mathrm{g\ mol^{-1}}) \times 60}{10^6} \quad (15)$$

$$A_{spec}\ (\mu\mathrm{mol\ min^{-1}\ g^{-1}}) = \frac{\mathrm{TOF\ (h^{-1})} \times 10^6}{M_{catalyst}\ (\mathrm{g\ mol^{-1}}) \times 60} \quad (16)$$

(assumptions: in case of multimeric enzymes $M_{catalyst}$ = M of one subunit).

TOF and A_{spec} are typically determined from initial rates, i.e., at conversions below 10%, where product formation remains linear and is not yet affected by factors such as product inhibition or catalyst inactivation. While the TOF is normalized to the number of active sites, A_{spec} is normalized to the mass of catalyst used. Typical enzymatic TOFs range from a few to several hundred per second, whereas those of chemical catalysts are often expressed on an hourly scale. However, because enzymes have a much higher molecular weight, the corresponding A_{spec} values of both catalyst types tend to be of comparable magnitude.

3.6. Total Turnover Number

Whereas TOF and A_{spec} provide activities, the total turnover number (TTN) quantifies the amount of product generated per mole of catalyst, providing a unitless measure expressed as mol of product per mol of catalyst (eq 17):[117,118]

$$\mathrm{TTN} = \frac{\text{Amount of product formed (mol)}}{\text{Amount of catalyst (mol)}} \quad (17)$$

TTN is a cumulative metric that reflects the catalyst's durability and long-term performance. It also reflects the economic feasibility and environmental impact of a catalyst.

3.7. Turnover Number

Turnover numbers are defined differently across fields, often leading to confusion. In enzymology, turnover number (s^{-1}), also termed k_{cat}, represents the maximum number of substrate molecules converted per enzyme active site per time.[119] In organometallic catalysis, turnover number (mol) refers to the number of substrates that a catalyst can convert to products.[120] In photobiocatalysis, turnover number is often used interchangeably with TTN. To avoid confusion, we will use TTN rather than turnover number in this context.

3.8. Product Yield and Conversion Yield

The product yield is the amount of product formed divided by the amount of substrate added (eq 18):

$$\text{Product yield (\%)} = \frac{\text{Amount of product formed (mol)}}{\text{Initial amount of substrate (mol)}} \times 100 \quad (18)$$

Product yields can be reported as analytical or isolated yields. Conversion yield represents another popular measure. It quantifies the amount of substrate consumed during the reaction relative to the initial substrate amount, irrespective of the product quantity (eq 19):

$$\text{Conversion yield (\%)} = \left(1 - \frac{\text{Remaining amount of substrate (mol)}}{\text{Initial amount of substrate (mol)}}\right) \times 100 \quad (19)$$

In contrast to the product yield, the conversion yield is less informative, as it does not distinguish how the starting material disappears from the reaction mixture (e.g., through evaporation, absorption, or degradation). Thus, product yield is a more appropriate metric than conversion yield to report when the objective is to highlight the system's ability to synthesize desired products. To further refine efficiency assessments, reaction selectivity should be determined to account for product distribution.

3.9. Reaction Selectivity

Reaction selectivity is a key performance indicator that quantifies the proportion of consumed substrate that is converted specifically into the desired product rather than undesired byproducts. Selectivity is typically defined as eq 20:

$$\text{Reaction selectivity (\%)} = \frac{\text{Amount of desired product formed (mol)}}{\text{Amount of converted substrate (mol)}} \times 100 \quad (20)$$

3.10. Enantiomeric Excess

Enantioselectivity describes the preferential formation of one enantiomer over its mirror-image counterpart. A common quantitative assessment of enantioselectivity is enantiomeric excess (ee), which indicates the extent to which one enantiomer predominates over the other. It is calculated by comparing the concentrations of two enantiomers using the following eq (eq 21):

$$\text{ee (\%)} = \left|\frac{[R] - [S]}{[R] + [S]}\right| \times 100 \quad (21)$$

where $[R]$ and $[S]$ are the concentrations of the two enantiomers.

4. PHOTOCATALYTIC ENZYME ACTIVATION FOR SUSTAINABLE BIOSYNTHESIS

4.1. Mediated Electron Transfer in Abiotic–Biotic Systems

In situ recycling of coenzymes enables sustainable chemical synthesis by coenzyme-dependent enzymes (e.g., alcohol dehydrogenase, glucose-1-dehydrogenase, ene-reductase) and microorganisms (e.g., *Escherichia coli*, *Shewanella oneidensis*). Coenzyme recycling addresses the economic and practical challenges associated with the stoichiometric consumption of expensive coenzymes (cost per mole: $2,600 for NADH, $1,400 for NAD^+, $70,000 for NADPH, $18,000 for $NADP^+$).[121] Photochemical regeneration of coenzymes has been demonstrated across diverse photobiocatalytic platforms employing photoactive molecules (e.g., xanthene dyes, $Ru(bpy)_3^{2+}$, porphyrin, flavin)[122−133] or (in)organic semiconducting particulates (e.g., aggregation-induced emission micelle, CdSe quantum dots, TiO_2, MXene, metal organic framework, graphitic C_3N_4, single atom catalyst, carbon nanodots, covalent−organic framework).[17,134−156] Mechanistically, these

https://doi.org/10.1021/acs.chemrev.5c01010
Chem. Rev. 2026, 126, 4857−4899

Table 2. Comparison of Photocatalytic NADH Regeneration Systems for Enzymatic Synthesis

Abiotic catalyst	Electron mediator	Electron donor	Light source	Maximum NADH production rate	Maximum NADH yield	Target biocatalysis	Substrate	Product	Maximum TOF	Maximum TTN	ref.
QDs/g-C_3N_4 nanosheet (1.0 g L^{-1})	M_{ox} (0.25 mM)	TEOA (0.67 M)	Xe lamp (λ > 420 nm)	0.94 mM h^{-1} (estimated)	95.7% (2 h)	ADH-catalyzed furfural-to-furfuryl alcohol		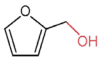	12.0 h^{-1} (estimated)	44.9 (estimated)	134
Co single atom@PCN (0.8 g L^{-1})	M_{ox} (0.3 mM)	H_2O	410 nm LED (2.04 mW cm^{-2})	0.135 mM h^{-1} (estimated)	33.6% (2 h)	FDH-catalyzed CO_2-to-formate	CO_2	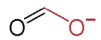	Cannot be estimated	Cannot be estimated	135
Lawn-like TP-COFs/MXene (1.0 g L^{-1})	None	TEOA (1 M)	300 W Xe lamp (λ > 420 nm, 153.3 mW cm^{-2})	1.16 mM h^{-1} (estimated)	46% (30 min)	FDH-catalyzed CO_2-to-formate	CO_2	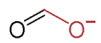	Cannot be estimated	Cannot be estimated	139
Anatase/rutile-TiO_2@MXene (1.33 g L^{-1})	None	EDTA-2Na (0.15 M)	300 W Xe lamp (390.2 mW cm^{-2})	2.1 mM h^{-1} (estimated)	65% (50 min)	FDH-catalyzed CO_2-to-formate	CO_2	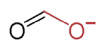	0.668 h^{-1}	4.75 (estimated)	140
Porpyhrin-based 2D COF thin film (1 x 3 cm^2)	M_{ox} (0.2 mM)	Ascorbic acid (33 mM)	Xe lamp (λ > 420 nm, 100 mW cm^{-2})	0.3 mM h^{-1} (estimated)	98.5% (2 h)	FDH-catalyzed CO_2-to-formate	CO_2	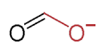	Cannot be estimated	Cannot be estimated	141
Rh-sp^2c-COF (1.0 g L^{-1})	Anchored M_{ox} (60.8 μM)	TEOA (1 M)	300 W Xe lamp (λ > 420 nm)	2.17 mM h^{-1}	82% (1 h)	EREDs-catalyzed asymmetric hydrogenation of C=C bonds			112 h^{-1} (estimated)	401 (estimated)	142
MXene/COF-367 heterostructure (1.0 g L^{-1})	None	TEOA (1 mM)	380-750 nm LED (100 mW cm^{-2})	0.28 mM h^{-1} (estimated)	83.4% (5 h)	FDH-catalyzed CO_2-to-formate	CO_2	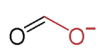	Cannot be estimated	Cannot be estimated	143
Triazine-based 2D COF (1.0 g L^{-1})	M_{ox} (0.5 mM)	TEOA (1 M)	300 W Xe lamp (λ > 420 nm)	7.92 mM h^{-1} (estimated)	90.4% (10 min)	GDH-catalyzed α-ketoglutarate-to-L-glutamate	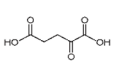	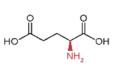	Cannot be estimated	Cannot be estimated	144
MIL-125-Py-Rh (5.0 g L^{-1})	Anchored M_{ox} (0.277 mM)	TEOA (1 M)	450 nm LED	0.81 mM h^{-1} (estimated)	66.4% (1 h)	Immobilized FDH-catalyzed CO_2-to-formate	CO_2	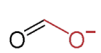	Cannot be estimated	Cannot be estimated	145
Lignin-vaterite/Eosin Y microsphere (16.7 g L^{-1})	M_{ox} (0.25 mM)	TEOA (0.2 M)	White LED (4.55 mW cm^{-2})	0.41 mM h^{-1}	59.6% (1 h)	Immobilized GDH-catalyzed α-ketoglutarate-to-L-glutamate	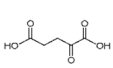	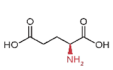	1,060 h^{-1}	39,800	161
g-C_3N_4 nanosheet (1.25 g L^{-1})	None	TEOA (0.2 M)	400-800 nm LED (100 mW cm^{-2})	1.02 mM h^{-1} (estimated)	97.3% (12 h)	ADH-catalyzed acetaldehyde-to-ethanol			Cannot be estimated	Cannot be estimated	162
Rh-NU-1006 (1.8 mM)	Anchored M_{ox} (0.029 mM)	TEOA (0.5 mM)	420 nm LED	28.0 mM h^{-1}	100% (24 h)	Immobilized FDH-catalyzed CO_2-to-formate	CO_2	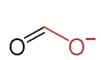	865 h^{-1}	20,800 (estimated)	178
InP quantum dot (1.5 μM)	M_{ox} (0.25 mM)	TEOA (1 M)	460 nm LED (~200 mW cm^{-2})	4.68 mM h^{-1}	> 99% (30 min)	ADH-catalyzed butyraldehyde-to-butanol	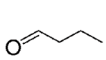	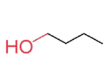	53,300 h^{-1} (estimated)	11,000 (estimated)	179
CdS@Protamine-induced TiO_2 microcapsule (1.5 g L^{-1})	Anchored M_{ox}	TEOA (0.4 M)	420 nm LED	4.86 mM h^{-1} (estimated)	~41% (10 min)	ADH-catalyzed propionaldehyde-to-propanol		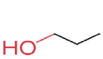	38,000 h^{-1}	19,000 (estimated)	180

abiotic catalysts regenerate reduced or oxidized forms of coenzymes [e.g., 1,4-dihydronicotinamide adenine dinucleotide (1,4-NADH), its phosphorylated form (1,4-NADPH), corresponding oxidized forms ($NAD(P)^+$), flavin mononucleotide hydroquinone ($FMNH_2$), and viologens] that participate in electron transfer to or from enzymatic prosthetic groups (e.g., FMN, Zn^{2+}, pyrroloquinoline quinone). Other biological electron carriers include lipophilic quinones (e.g., ubiquinone,[157] menaquinone[158]) and specialized redox-active proteins (e.g., ferredoxin, flavodoxin[159]). These carriers function as central components of natural biological electron-transfer networks. The photochemical regeneration of such carriers could be leveraged to deliver electrons to redox enzymes in biosolar conversion, although photobiocatalytic synthesis examples using these electron carriers remain limited yet.

4.1.1. Nicotinamide Coenzyme Regeneration. *In situ* regeneration of the reduced nicotinamide coenzyme (NAD(P)H) is the most extensively reported example of indirect electron transfer: photoexcited electrons are transferred from the light-absorbing catalytic materials[134,135,142,160−164] to the oxidized form of coenzyme (i.e., $NAD(P)^+$) (Table 2). Concurrently, sacrificial electron donors such as TEOA and EDTA[165−173] donate electrons to restore the oxidized photocatalyst, thus completing the catalytic redox cycle. NAD(P)H serves as a reductant in the biocatalytic reaction

https://doi.org/10.1021/acs.chemrev.5c01010
Chem. Rev. 2026, 126, 4857−4899

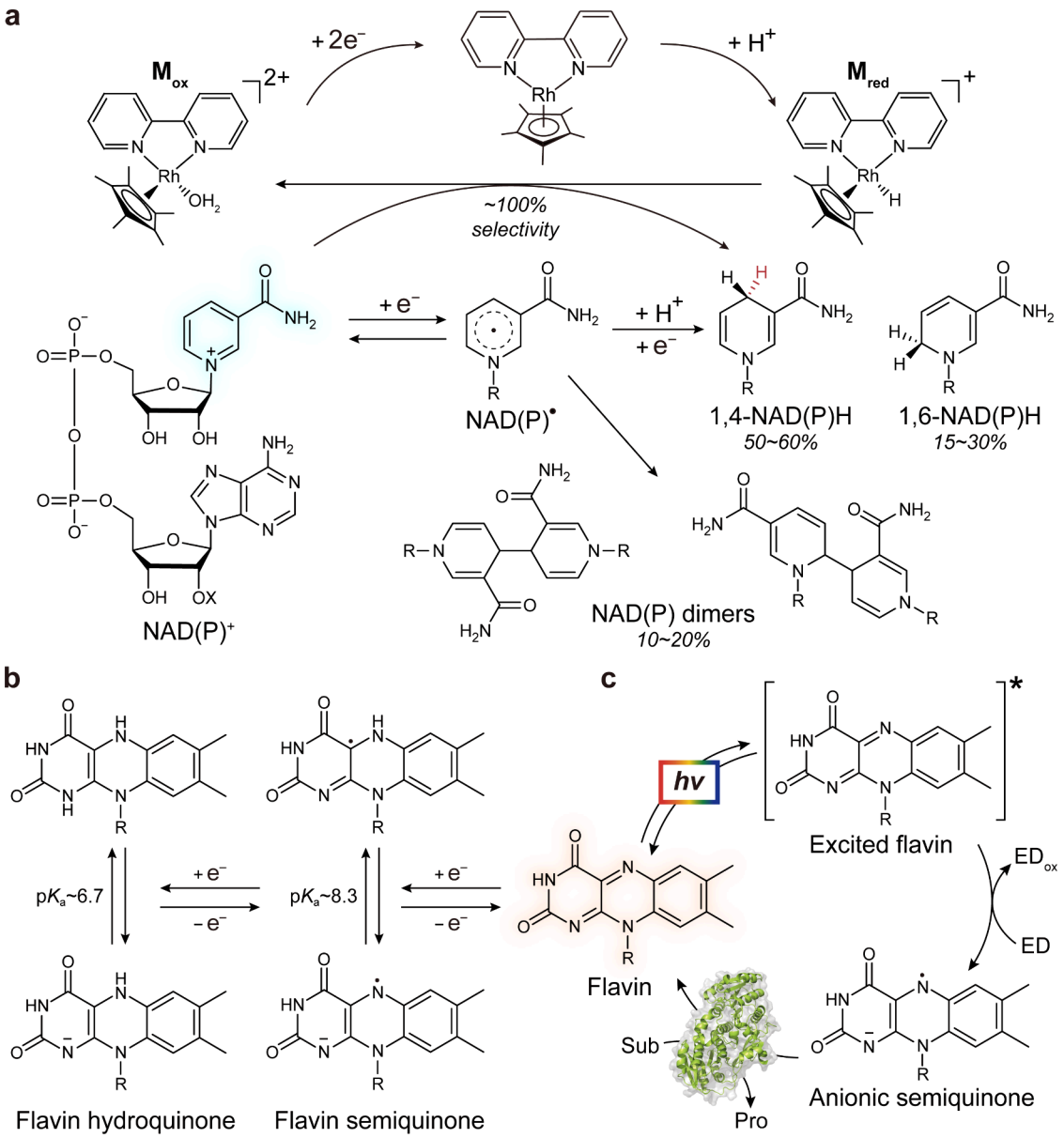

Figure 6. Redox chemistry of nicotinamide and flavin molecules. (**a**) Comparison of direct and mediated reduction of NAD(P)$^+$ coenzymes. Direct one-electron reduction generates the NAD(P)$^\bullet$ radical and affords a mixture of 1,4-NAD(P)H, 1,6-NAD(P)H and NAD(P) dimers. The percentages represent typical product distributions. With the Rh-based **M** complex, two-electron reduction of $\mathbf{M}_{ox}$ followed by hydride transfer to NAD(P)$^+$ furnishes 1,4-NAD(P)H. (**b**) Proton-coupled reduction of oxidized flavin to its semiquinone and hydroquinone states. pK_a values for the relevant acid–base transitions are indicated. (**c**) Redox cycle of flavin-driven catalysis. Abbreviations: Pro, product; Sub, substrate; ED, electron donor; ED_{ox}, oxidized electron donor.

of interest while being reoxidized and thereby closing the enzymatic cycle.

Direct transfer of photoexcited electrons from a photocatalyst to NAD(P)$^+$ is possible, but this route suffers from low selectivity. Mechanistically, the process proceeds via two sequential single-electron transfer steps, resulting in the formation of a NAD(P)$^\bullet$ radical intermediate.[174−176] This radical can be further reduced to enzymatically active NAD(P)H; however, it is also prone to engaging in nonselective side reactions that yield nonfunctional byproducts, such as 1,2-NAD(P)H, 1,6-NAD(P)H, and NAD(P) dimers (Figure 6a). This issue underscores the need for alternative strategies that enhance both the selectivity and thermodynamic efficiency in NAD(P)H regeneration systems.

To address the limitation, redox mediators,[55,177,178] such as $[Cp^*Rh(III)(bpy)(H_2O)]^{2+}$ (Cp^* = C_5Me_5, bpy = 2,2′-bipyridine) ($\mathbf{M}_{ox}$), have been used to achieve nearly 100% selectivity for 1,4-NAD(P)H production under a milder reduction potential of −0.14 V (vs RHE); upon receiving photoexcited electrons from a photocatalyst, $\mathbf{M}_{ox}$ becomes $[Cp^*Rh(III)(bpy)H]^+$ ($\mathbf{M}_{red}$) via Cp*Rh(I)(bpy), and the $\mathbf{M}_{red}$ couples the two single-electron transfer steps into one hydride-transfer to the C4 atom of NAD(P)$^+$ (Figure 6a). This mediated route bypasses the formation of NAD(P)$^\bullet$ radicals and prevents the side reactions that form inactive isomers or dimers, thereby ensuring that the recycled coenzyme remains fully active and available for enzyme catalysis.

Though $\mathbf{M}_{red}$-driven NAD(P)H regeneration is highly selective for the formation of catalytically active 1,4-NAD(P)-

https://doi.org/10.1021/acs.chemrev.5c01010
Chem. Rev. 2026, 126, 4857−4899

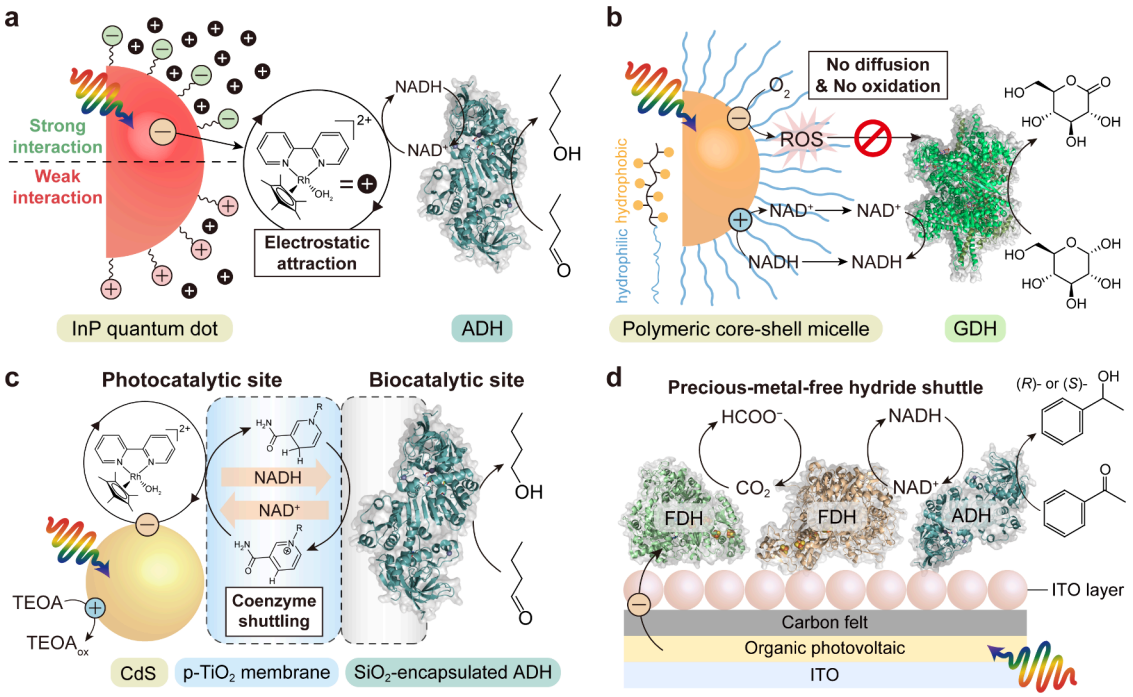

Figure 7. Photo(electro)catalytic regeneration of nicotinamide-based coenzymes. (**a**) Electrostatic modulation of photocatalyst-mediator interactions for enhanced NADH regeneration.[179] Negatively charged surfaces electrostatically attract positively charged redox mediator, increasing its local concentration and accelerating electron transfer to NAD^+. (**b**) Core−shell micellar structures for redox shielding.[136] The hydrophilic shell prevents the escape of reactive oxygen species (ROS) that deactivates redox enzymes. (**c**) Membrane-separated architecture for coenzyme shuttling.[180] Photogenerated NADH diffuses across the membrane to drive the biocatalytic reaction. (**d**) Precious-metal-free NADH regeneration on photocathode.[181] An enzyme-only $CO_2/HCOO^-$ redox loop with formate dehydrogenases (FDHs) enables a Rh-free hydride shuttle on an organic photovoltaic-integrated photocathode. Abbreviations: ADH, alcohol dehydrogenase; GDH, glucose 1-dehydrogenase; CdS@p-TiO_2, CdS quantum dots deposited protamine induced TiO_2; ITO, indium tin oxide.

H, the overall selectivity of photocatalytic NAD(P)H regeneration systems may be impaired by DET from the photocatalyst to $NAD(P)^+$. Engineering the surface charge of the heterogeneous photocatalyst can alleviate this issue as the dominant states of the catalytic complex **M** are positively charged whereas the nicotinamide cofactor, both $NAD(P)^+$ and NAD(P)H, is overall an anion (Figure 6a).

The Pillai group underscored the significance of electrostatic attraction (Figure 7a and Table 2):[179] altering the surface charge of the photocatalyst (indium phosphide) from positive to negative increased the local concentrations of **M** in the proximity to the indium phosphide surfaces while it simultaneously decreased the local concentration of NAD(P). As a result, the yield of enzymatically active NADH was doubled. A similar electrostatic coupling strategy (i.e., facilitating the interaction between $\mathbf{M_{ox}}$ and a positively charged $[Ru(bpy)_3]^{2+}$ photocatalyst by introducing carboxylate groups to the bpy-ligand of **M**) increased the NADH yield by approximately 6.3-fold.[182]

The broad scope of **M** also opens up possibilities of *in situ* regeneration of noncanonical redox coenzymes such as NAD-mimicking N-benzyl nicotinamide (mNAD). For example, nitrogen-doped carbon nanodots have been demonstrated as photocatalytic nanoparticles converting $\mathbf{M_{ox}}$ to $\mathbf{M_{red}}$ to recycle mNADHs under solar-simulated light.[164] This photocatalytic supply of the reduced coenzymes accelerated ene-reductase-driven *trans*-hydrogenation of C=C bonds. Similarly, photocatalytic graphitic C_3N_4 has been reported to regenerate mNADHs and enhance the yield of enzymatic products under blue light (λ: 460 nm).[183] *In situ* regeneration of better-than-nature mNADHs driven by these metal-free photocatalysts (carbon nanodots and graphitic C_3N_4) can be rationalized by quasi-Fermi level alignments that are thermodynamically suitable for $\mathbf{M_{ox}}$ reduction ($E_{qF,electron} < E_{red}$ ($\mathbf{M_{ox}}/\mathbf{M_{red}}$)) and concurrent TEOA oxidation ($E_{qF,hole} > E_{ox}$ ($TEOA_{ox}/TEOA$)).

Apart from the Rh-based electron mediators, ferredoxin:-$NADP^+$-reductase[184−194] has been used as an electroactive biocatalyst for NADPH regeneration. Comparable to $\mathbf{M_{ox}}$, ferredoxin:$NADP^+$-reductase also accepts electrons from photoactive materials and reduces nicotinamide coenzymes. However, the reductase exhibits strict specificity for the recycling of NADPH, not NADH.[195] Harnessing the capability of ferredoxin:$NADP^+$-reductase to catalyze the reduction of $NADP^+$ to NADPH, CdSe quantum dots have been integrated with the reductase through favorable electrostatic interactions between the negatively charged surface ligands of CdSe and the positively charged ferredoxin:$NADP^+$-reductase. Under these preferential binding conditions, photoexcited electrons from CdSe nanoparticles were transferred directly to the flavin adenine dinucleotide prosthetic group of the NADPH-generating reductase upon blue-light irradiation.[196] Subsequently, the enzyme executes hydride transfer to $NADP^+$, enabling NADPH recycling that sustained the alcohol-dehydrogenase-catalyzed reduction of aldehydes to alcohols.

In addition to the reductive recycling of NAD(P)H and nicotinamide analogues, the photocatalytic regeneration of NAD^+ has been achieved for enzymatic oxidation reactions. In this approach, photoactive materials oxidize 1,4-NADH to NAD^+. The regenerated NAD^+ is subsequently used by NAD^+-dependent redox enzymes to drive oxidative transformation.

https://doi.org/10.1021/acs.chemrev.5c01010
Chem. Rev. 2026, 126, 4857−4899

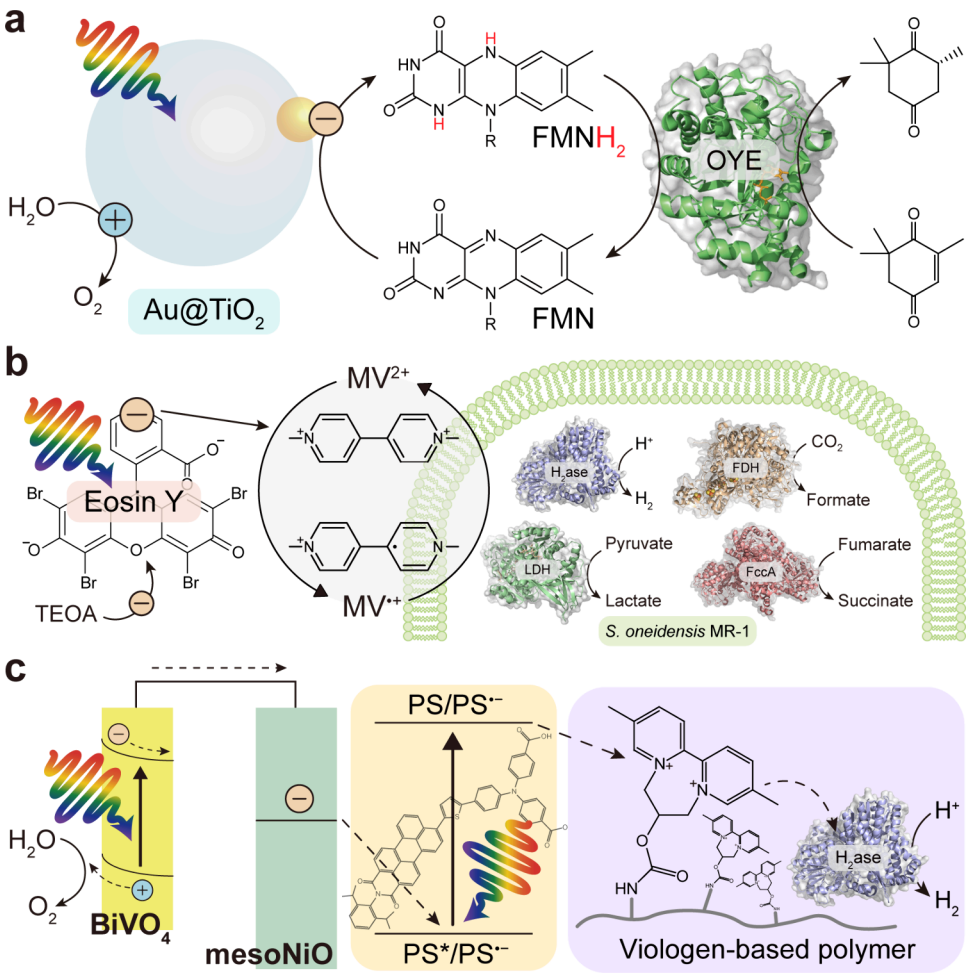

Figure 8. Photo(electro)catalytic recycling of flavin and viologen mediators. (a) Photochemical regeneration of flavin mononucleotide neutral hydroquinone ($FMNH_2$) for flavoprotein-catalyzed asymmetric hydrogenation.[213] TiO_2-based photocatalysts reduce FMN to $FMNH_2$ using H_2O as an electron donor. (b) Photoreduction of methyl viologen (MV^{2+}) for intracellular reactions in microorganism.[214] The reduced form of MV^{2+}, $MV^{\bullet+}$, mediates electron delivery to native metabolic enzymes. (c) Immobilized viologen-based redox polymers for localized electron transfer.[215] A viologen-functionalized photocathode enables surface-confined electron delivery to redox enzymes. Abbreviations: $Au@TiO_2$, gold-loaded TiO_2; mesoNiO, mesoporous NiO; PS, photosensitizer; TEOA, triethanolamine; OYE, old yellow enzyme; FDH, formate dehydrogenase; LDH, lactate dehydrogenase; FccA, fumarate reductase.

Concurrently, the photoactive materials reduce electron acceptors (mostly O_2) to complete the overall redox cycle. In contrast to the reductive regeneration of NAD(P)H, the reverse reaction does not suffer from selectivity issues, as the aromatic, oxidized nicotinamide represents the only thermodynamically stable product. As a result, mediated approaches such as NAD(P)H regeneration are not necessary.

Natural flavins have for a long time been used as catalysts for the aerobic (H_2O_2-forming) reoxidation of NAD(P)H to drive $NAD(P)^+$-dependent oxidation reactions[197] but the hydride transfer from NAD(P)H to the oxidized alloxazine is kinetically impaired. This limitation can be overcome by photoactivation of the flavin catalyst by blue light and be used for example for the biocatalytic oxidative lactonization of diols, yielding enantiomerically pure lactones.[198,199]

Polymeric core−shell micelles have been constructed for biosolar oxidation of glucose under visible light.[136] In this configuration, photoexcited holes oxidized NADH to NAD^+, whereas photoexcited electrons reduced O_2 as electron acceptor (Figure 7b) without the need for artificial electron mediators (e.g., **M** for NADH regeneration). Similarly, amyloid/solvatochromic dye hybrid has been reported for biosolar oxidation of ethanol under visible light, where the solvatochromic dye—with its twisting motion suppressed to enable charge-transfer catalysis—recycled NAD^+ and drove enzymatic process.[200]

During photochemical regeneration of nicotinamide coenzymes, photoactive materials often generate reactive oxygen species (e.g., $^1O_2$, $^{\bullet}OH$, $O_2^{\bullet-}$) that impair enzyme integrity. This challenge has been addressed through the spatial decoupling of photocatalysts and enzymes. Protamine-induced TiO_2 (p-TiO_2) capsule architectures exemplify this approach, wherein NADH-regenerating CdS quantum dots were compartmentalized within porous p-TiO_2 membranes, while silica-encapsulated alcohol dehydrogenase remained outside (Figure 7c and Table 2).[180] The porous p-TiO_2 permitted NAD^+/NADH transport between CdS and dehydrogenase, preventing direct enzyme-radical contact. Similarly, photocatalytic amphiphilic polymers established a steric shielding layer by confining photocatalysts within a hydrophobic core and surrounding them with a poly(ethylene glycol) shell.[136] The thickness of the shell (8.6−12.5 nm) exceeded the diffusion length of short-lived $^1O_2$ (~10 nm), thereby protecting glucose-1-dehydrogenase from photocatalyst-in-

https://doi.org/10.1021/acs.chemrev.5c01010
Chem. Rev. 2026, 126, 4857−4899

duced oxidative damage. Concurrently, NADH was oxidized to NAD^+ under visible light for the sustained enzymatic oxidation of glucose.

4.1.2. Flavin Coenzyme Recycling. Like NAD(P)H and its analogues, flavin molecules—including riboflavin (RF), flavin mononucleotide (FMN), and flavin adenine dinucleotide (FAD)—serve as a redox mediator that shuttles electrons to and from redox enzymes (especially flavoenzymes). Upon accepting electrons from a photocatalyst, the isoalloxazine core of flavin first takes up an electron into its π^* orbital at the N5/C4a region to form the intermediate semiquinone (neutral or anionic depending on the pH), and then accepts a second electron to yield the fully reduced hydroquinone (neutral or anionic) species (Figure 6b).[201,202] The redox potential of free $FMN/FMNH_2$, $FAD/FADH_2$, and RF/RFH_2 are approximately 0.205, 0.206, and 0.191 V (vs RHE), respectively.[203,204] Oxidized flavins are blue-light responsive photocatalysts themselves, enabling their self-photoreduction in the presence of a sacrificial electron donor.[205,206] This reactivity has been exploited for the nicotinamide-independent regeneration of monooxygenases,[207−209] ene-reductases,[210,211] peroxygenases[212] or for driving ADH-catalyzed oxidations[198] (Figure 6c).

The electron donor scope of photoexcited flavins, however, is rather limited to low-redox-potential electron donors such as reduced nicotinamides, EDTA, or TEOA. More attractive electron donors or even water are inaccessible. To achieve this, photochemical regeneration of $FMNH_2$ was coupled to metal-loaded TiO_2 particulates (e.g., gold-loaded TiO_2, vanadium-loaded TiO_2) as cocatalysts to drive enzymatic asymmetric hydrogenation (Figure 8a).[213] Upon photoexcitation, TiO_2 extracted electrons from H_2O and transferred the photoexcited electrons to FMN, producing the two-electron-reduced form, $FMNH_2$. This reduced flavin served as an electron donor to the flavin prosthetic group of an old yellow enzyme homologue from *Thermus scotoductus* SA-01 (*Ts*OYE), enabling stereoselective hydrogenation of ketoisophorone to (*R*)-levodione. These studies establish *in situ* light-driven FMN regeneration as a robust strategy for flavoenzyme-catalyzed reactions.

When photocatalysts undergo the rapid recombination of photoexcited charge carriers, electron transfer to FMN becomes kinetically inaccessible. An outer-sphere redox mediator provides an alternative electron-transfer pathway that bypasses the recombination issue. For example, CdSe quantum dots did not generate the reduced form of FMN because charge recombination outpaced electron transfer to FMN.[137] An outer-sphere electron-relaying method using methyl viologen (MV^{2+}) circumvented this kinetic bottleneck by capturing photoexcited electrons from CdSe (time scale ~10 ps) and stabilizing the electrons as a longer-lived $MV^{+\bullet}$ radical. This relay intermediate subsequently reduced FMN via a secondary electron-transfer step, achieving *in situ* flavin recycling and driving flavoenzyme-catalyzed reduction of α,β-unsaturated alkenes.

4.1.3. Redox Cycling of Viologen Mediators. Artificial viologen derivatives (e.g., MV^{2+}, ethyl viologen)[7,216,217] act as diffusible, external electron transfer mediators between photocatalysts and enzymatic cofactors (e.g., flavin of ene-reductase, tungsten of FDH, $[Fe_4S_4]$ cluster of nitrogenase).[8,218−222] Their 4,4'-bipyridinium core undergoes a reversible one-electron reduction via electron acceptance into their delocalized π^* (LUMO) orbital. This electron transfer yields a radical cation species (e.g., $MV^{\bullet+}$) with a characteristic deep-blue color, but their susceptibility to reoxidation by O_2 requires strictly anaerobic conditions to maintain their stability. In addition, $MV^{\bullet+}$ is cytotoxic under aerobic conditions because it reacts with O_2 to generate superoxide radicals ($MV^{\bullet+} + O_2 \rightarrow MV^{2+} + O_2^{\bullet-}$), which imposes oxidative stress on cellular components.[223]

Like flavin coenzymes, viologens accept electrons directly from photoactivated catalysts. The redox potential of viologen redox couples (−0.198 V vs RHE for MV^{2+} and ethyl viologen)[224] is more negative than that of flavin (0.191 to 0.206 V vs RHE) and nicotinamide (0.093 V vs RHE) couples, rendering $MV^{\bullet+}$ a stronger reductant. The capability of $MV^{\bullet+}$ is exemplified in the light-driven activation of ene-reductases; photoactivated Ru(II) and Ir(III) complexes were reported to transfer electrons to MV^{2+} at the expense of TEOA under UV−visible light (λ > 360 nm).[225] The resultant $MV^{\bullet+}$ subsequently reduced the flavin prosthetic group of ene-reductases from *Thermoanaerobacter pseudethanolicus*, achieving hydrogenation of cyclohexen-2-one to cyclohexanone.

Beyond the photochemical activation of cell-free enzymes, viologen regeneration has been extended to whole-cell biocatalysis. Honda and co-workers developed solar-driven H_2 evolution using recombinant *Escherichia coli* cells engineered to express [FeFe]-H_2ase and maturase genes.[138] Their photobiocatalytic strategy used anatase TiO_2 as a photocatalyst, MV^{2+} as an electron mediator, and ascorbic acid as an electron donor. Under simulated solar irradiation (λ > 250 nm), anatase TiO_2 regenerated $MV^{\bullet+}$ from MV^{2+} extracellularly, and H_2 was produced intracellularly at approximately 0.721 μmol min^{-1} (mg of wet cells)$^{-1}$. In addition, this whole-cell approach demonstrated improved operational stability, maintaining activity for an extended reaction period of up to 15 h compared to systems using purified H_2ase. However, the pathway by which $MV^{\bullet+}$ engages the cytosolic hydrogenase remains unresolved. Because MV^{2+} is known to be impermeable cation across *Escherichia coli* membranes,[226] the observed H_2 production suggests the involvement of indirect intracellular electron-transfer, the exact mechanism of which requires further investigation.

Expanding the versatility of this methodology, photocatalytic $MV^{\bullet+}$ recycling was paired with the nonphotosynthetic bacterium *Shewanella oneidensis* under visible light (λ > 400 nm) (Figure 8b).[214] Photoreduced $MV^{\bullet+}$ acted as an electron mediator, driving intracellular enzymatic reactions, including H_2 evolution, fumarate hydrogenation, and reduction of CO_2 and pyruvate. These biosolar syntheses were realized when eosin Y and $Ru(bpy)_3^{2+}$ served as molecular photocatalysts by using TEOA as an electron donor. This cell-based platform bypassed the need for enzyme purification and leveraged the catalytic repertoire of *Shewanella oneidensis*. Nevertheless, this work also left the mechanistic question unanswered. Direct evidence of $MV^{\bullet+}$ entry into the periplasm or cytoplasm was not conclusively verified, and the precise path of electron transfer from the cell surface to the target enzymes remains speculative. Future investigations into the role of cellular electron transport components could further elucidate the intricate mechanisms underlying this promising photocatalytic platform.

4.2. Direct Electron Transfer Across Abiotic−Biotic Interfaces

DET involves direct delivery of electrons between an enzyme's buried redox center (or electron relay chain) and photo-

https://doi.org/10.1021/acs.chemrev.5c01010
Chem. Rev. 2026, 126, 4857−4899

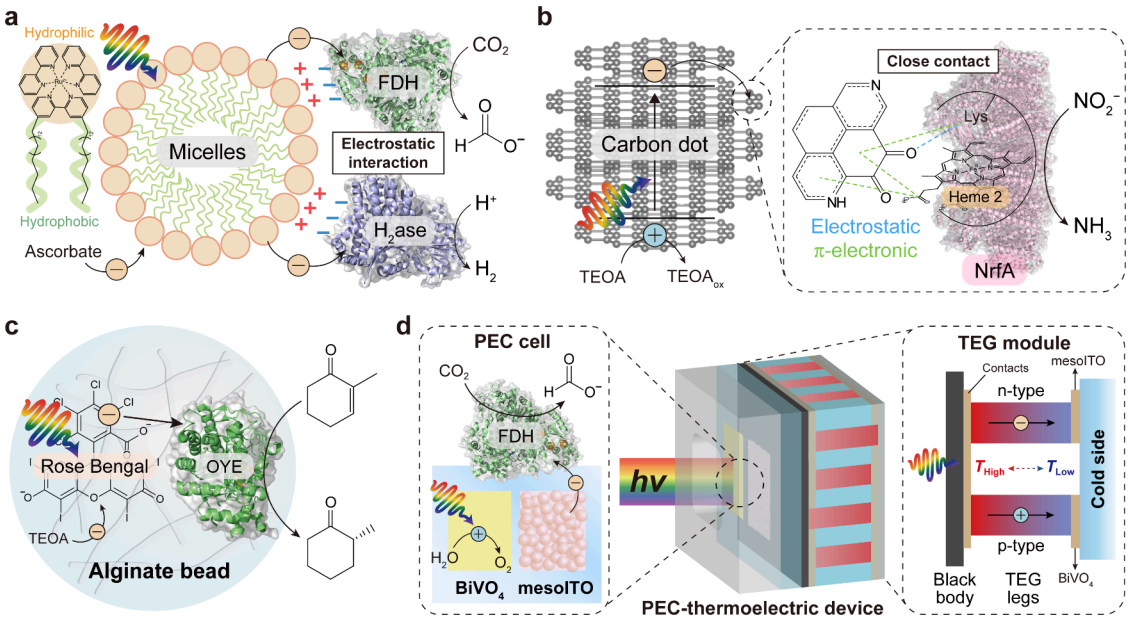

Figure 9. DET-based strategies for light-driven redox biocatalysis. (**a**) Electrostatic interface engineering between cationic micelles and metalloenzymes.[227] Ru-based micellar photocatalysts align with the negatively charged surface of oxidoreductases to facilitate direct electron injection into distal cofactors. (**b**) Direct electronic interfacing of π-conjugated carbon dots with hemeproteins.[286] Aromatic ketone-functionalized carbon dots bind near heme 2 via π-electronic and electrostatic interactions, enabling DET toward the enzyme's active site. (**c**) Molecular proximity-driven DET to flavoenzymes within encapsulated architectures.[287] Colocalization of organic dye and redox enzyme in a hydrogel matrix enables DET to the flavin cofactor. (**d**) Thermoelectric-assisted photoelectrocatalytic device for bias-free DET.[20] A thermoelectric generator (TEG) harvests sub-band gap thermal energy to supply auxiliary photovoltage to the photoelectrode via the Seebeck effect, enabling full-spectrum light utilization. Abbreviations: mesoITO, mesoporous indium tin oxide; TEOA, triethanolamine; FDH, formate dehydrogenase; NrfA, cytochrome *c* nitrite reductase; OYE, old yellow enzyme.

catalytic materials (e.g., $Ru(bpy)_3^{2+}$ micelles, cyanamide-g-C_3N_4 sheets, organosilica nanodots)[227−229] without the aid of coenzymes or artificial mediators.[230−233] Because most enzymes' active sites are deeply buried within a nonconductive polypeptide environment, efficient DET critically depends on precise redox-level alignment and subnanometer, electrostatically complementary contacts that promote quantum tunneling at the protein-material interface. In contrast to mediated electron transfer, where oxidoreductases rely on diffusing coenzymes or mediators, DET bypasses these additional redox steps. As a result, DET simplifies the overall reaction scheme and enhances charge transfer efficiency, ultimately enabling coenzyme-free, biosolar synthesis of fuels and chemicals (e.g., H_2, formate, methanol, acetate, poly-β-hydroxybutyrate).[227−229,234−238]

4.2.1. Material Coupling with Metalloenzymes. Metal clusters are key inorganic prosthetic groups in many redox enzymes,[21,100,109,239−272] which exhibit remarkable structural and electronic flexibility enabling ligand binding and catalytic activity under ambient conditions. Recent studies showed that interfacial engineering accelerated DET to relay chains (e.g., FeS) and active sites (e.g., [W], [NiFeSe] or [FeFe]), thereby enabling solar fuel and chemical synthesis with high turnover.[22,227,228,230,273−284] For example, interfacing $[Ru(bpy)_3]^{2+}$-based micelles with FDH has been documented for biosolar synthesis of formate (Figure 9a).[227] This approach was tested with FDH from *Desulfovibrio vulgaris* Hildenborough, a tungsten-containing metalloenzyme featuring a [W] active site and multiple FeS clusters surrounded by negatively charged residues (e.g., Asp, Glu). Strong electrostatic interactions between the cationic Ru-based micelles and the anionic FDH surface enabled close contact and efficient interfacial electron delivery. Under simulated solar light (AM 1.5G), the photocatalytic micelles were reductively quenched by ascorbate, an electron donor, generating reduced Ru species capable of injecting electrons into the distal FeS clusters of FDH. These electrons were subsequently funneled through the relay chain to the [W] prosthetic group, yielding a TTN of 8,000 for FDH.

The significance of electrostatic complementarity in DET was further demonstrated by the Reisner group using cyanamide-functionalized graphitic carbon nitride that has a negatively charged surface (zeta potential: −36.2 mV).[228] The carbon nitride was interfaced with [FeFe]-H_2ase from *Clostridium pasteurianum*, the distal [4Fe-4S] cluster of which was surrounded by a positively charged protein domain. This electrostatic complementarity promoted stepwise electron transfer to the deeply embedded catalytic [FeFe] metallocofactor via [4Fe-4S] clusters, thereby ensuring efficient intraprotein charge transfer. The carbon nitride/H_2ase hybrid enabled efficient H_2 evolution, achieving a TTN of 198,000 under simulated solar light (AM 1.5G). This electrostatic preference was further corroborated by replacing the positively charged [FeFe]-H_2ase with [NiFeSe]-H_2ase, which presents a negatively charged patch near its distal [4Fe-4S] cluster. This inversion of local surface charge created an electrostatic mismatch that suppressed DET and reduced TTN by roughly 3 orders of magnitude.

Beyond material tuning, protein engineering is crucial to enhance the abiotic−biotic interfacial electron transfer by redesigning the enzyme architecture to create more efficient electron-entry sites. For example, introduction (or repositioning) of a surface-exposed cysteine residue proximal to the distal Fe−S relay can enable site-selective anchoring of photoactive

https://doi.org/10.1021/acs.chemrev.5c01010
Chem. Rev. 2026, 126, 4857−4899

redox moieties.[17,237,285] Through the modification, injected electrons are directed into the native intraprotein relay rather than into nonproductive interfacial pathways. In case of [NiFe]-H_2ase, such site-directed mutation enabled site-selective installation of Ag nanoclusters as an auxiliary electron-entry point, affording visible-light-driven H_2 evolution under aerobic conditions without altering the active-site composition.[17,237]

In addition to the cluster-mediated DET of redox enzymes (e.g., [W]-FDH, [FeFe]-H_2ase, [NiFeSe]-H_2ase), cluster-independent DET is possible when the active site is located near the enzyme surface. For example, organosilica nanodots activate soluble methane monooxygenase hydroxylase (MMOH) from *Methylosinus trichosporium* OB3b for biosolar conversion of CH_4 to methanol.[229] Under visible light ($\lambda > 400$ nm), the nanodots directly delivered photoexcited electrons to the surface-accessible,[229,288] glutamate-bridged diiron active site[133,289] of MMOH for CH_4 liquefaction to methanol (84.8 $mmol_{methanol}\ g_{cat}^{-1}$ over 24 h) under ambient conditions. This charge-transfer pathway departed from the natural one, where MMOH catalyzes CH_4 oxidation after receiving electrons from NADH via methane monooxygenase reductase.

Besides the MMOH having a diiron active site, heme proteins (e.g., CYP) have been photoactivated to produce oxygenated compounds via DET from photoactive materials (e.g., Ru-based complex, deazaflavin, eosin Y)[290−295] at their heme-iron centers. This electron transfer pathway circumvents the need for NAD(P)H coenzymes. Le et al. presented visible light-driven hydroxylation of C−H bonds through collaborative catalysis between CYP enzyme and natural flavin photocatalysts (e.g., RF, FMN, FAD).[296] Under white light illumination, flavin photoactivation converted the heme domain from the ferric (Fe^{3+}) to the ferrous (Fe^{2+}) state. This redox transition enabled hydroxylation of aromatic (4-nitrophenol, TTN: up to 139) and aliphatic (lauric acid, TTN: up to 34) substrates. Building on this foundational work, a subsequent study advanced flavin-mediated DET to whole-cell platforms by using *Escherichia coli* expressing human CYP enzymes.[42] In this *in vivo* context, the intracellular uptake of flavins obviated the need for CYP purification and enabled direct photoactivation of CYP within living cells. Consequently, this biohybrid system facilitated oxidative biotransformations of pharmaceuticals and steroids.

In analogy to CYP, which enables oxidative photobiocatalysis through photocatalytic reduction mechanism, cytochrome *c* nitrite reductase (NrfA)—a multiheme enzyme catalyzing the six-electron reduction of nitrite to ammonia—catalyzes biosolar valorization of nitrogen via photoreductive activation by photoactive materials. For example, photocatalytic carbon dots have demonstrated DET activation of NrfA under visible light (λ: 400 to 750 nm) (Figure 9b).[286] The nanoscale photocatalysts (~2 nm diameter) exhibited proximity (~10 Å) to the surface-exposed heme of NrfA through preferential binding mediated by π-electronic and electrostatic interactions with nearby lysine residues. This intimate association facilitated multistep electron transfer to the active site, yielding ammonia production at rates of up to $12.5 \pm 1.1\ \mu mol\ mg^{-1}\ h^{-1}$. Similarly, ammonium-terminated carbon nanodots drove biosolar hydrogenation of fumarate to succinate through DET to the surface-proximal heme cofactor of fumarate reductase under simulated solar irradiation (AM 1.5G).[277]

Extending DET-based ammonia synthesis, nitrogenases enable the synthesis of ammonia from inert N_2 through its interface with semiconducting photocatalysts. For example, a CdS-nitrogenase biohybrid system was developed wherein the morphology and surface electrostatics of CdS nanocrystals promoted the self-assembly with the nitrogenase's MoFe protein.[240,297] Efficient light harvesting and strong interfacial electronic coupling enabled the accumulation of successive electrons, granting access to the reduced [FeMo] cofactor E states required for N_2 activation and catalytic turnover. This electron-accumulation regime supported light-driven NH_3 formation while competing H_2 evolution remains an intrinsic side pathway.

4.2.2. Photoactivation of Flavin Prosthetic Groups. Flavoenzymes having a tightly bound flavin prosthetic group (e.g., FAD, FMN)[137,164,213,298] can accept photoexcited electrons directly from photocatalytic materials. This DET pathway is distinct from the mediated electron transfer where the flavin prosthetic group receives electrons from nicotinamide- or flavin-based coenzymes [e.g., NAD(P)H, NADH analogues, $FMNH_2$]. This concept has been exemplified through biosolar conversion mediated by Baeyer−Villiger monooxygenase. Hollmann and colleagues demonstrated that diffusing flavins (RF, FMN, FAD) function as molecular photocatalysts to photoactivate phenylacetone monooxygenase under aerobic conditions.[207] Under white light, these flavins deliver photoexcited electrons to the FAD prosthetic group at the expense of EDTA. The low enzymatic TOF and TTN were suggested to result from the slow kinetics of electron transfer to the phenylacetone monooxygenase. We conjecture that, given the well-documented ability of flavin photocatalysts to photochemically reduce O_2 to H_2O_2,[299−301] this side reaction may compete with the photoreduction of the monooxygenase's FAD moiety, thereby limiting the efficiency of the overall photobiocatalytic process.

In addition to the FAD-dependent Baeyer−Villiger monooxygenase, FMN-containing ene-reductases have fulfilled biosolar hydrogenation reactions. Xanthene derivatives (e.g., rose bengal shown in Figure 9c)[287,302] directly inject their photoexcited electrons into the FMN prosthetic group of *Ts*OYE. This DET led to asymmetric hydrogenation reactions with excellent enantioselectivity (ee >99%), a maximum conversion of 70.4%, and a TTN of 300. Notably, rose bengal exhibited (i) spontaneous association with the FMN prosthetic group and (ii) favorable electrostatic interactions with *Ts*OYE's surface, thereby facilitating efficient charge transfer to the flavin moiety. Using the same electron transfer scheme, NAD^+ (as a photocatalyst, not coenzyme) triggers *Ts*OYE-mediated biosolar *trans*-hydrogenation under solar light (λ: 260 to 900 nm), achieving a TOF of 1,260 h^{-1} and a TTN of 1,690.[303] This photoactivation approach fundamentally differs from conventional photocatalytic schemes that rely on NADH recycling for *Ts*OYE activation.

4.2.3. Electronic Coupling at Material−Bacteria Interfaces. Collaborative catalysis between nonphotoactive bacteria and photocatalysts enables biosolar chemical transformations, which are mediated by electron transfer from light-harvesting materials to bacterial cells, thereby stimulating microbial metabolism. CO_2-fixing biohybrid systems have been constructed by interfacing nanostructured photocatalysts (e.g., Au nanoclusters,[304] CdS,[16,305] $Cd_{0.8}Zn_{0.2}S$,[306] poly(3-hexylthiophene)-based semiconductor[307]) with electroactive acetogens (e.g., *Sporomusa ovata*[234,307,308] and *Moorella thermoace-*

https://doi.org/10.1021/acs.chemrev.5c01010
Chem. Rev. 2026, 126, 4857−4899

Table 3. H_2O_2-Dependent Biocatalysis Driven by Diverse Classes of Photocatalysts

Photocatalyst	Electron donor	Light source	Initial H_2O_2 production rate	Biocatalyst	Substrate	Product	Maximum TOF	Maximum TTN	Reaction time length	ref.
Kraft lignin (8 g L^{-1})	H_2O	Xe lamp (λ > 400 nm)	0.16 mM h^{-1}	UPO	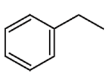	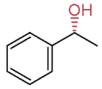	6,500 h^{-1}	72,600	130 h	314
					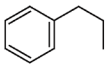	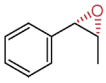	Cannot be estimated	27,100		
N-doped carbon nanodots (5.0 g L^{-1})	H_2O	391 nm LED	0.0006 mM h^{-1} (estimated)	UPO			65 h^{-1} (estimated)	7,800	120 h	316
Pd-loaded 3DOM TiO_2 (5.0 g L^{-1})	Methanol (32 mM)	300 W Xe lamp	1.56 mM h^{-1}	UPO	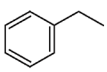	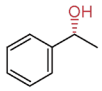	Cannot be estimated	Cannot be estimated	12 h	317
Pt-loaded g-C_3N_4 (1.0 g L^{-1})	Methanol (150 mM)	150 W halogen lamp (λ > 400 nm, 10.4 mW cm^{-2})	Not reported	UPO	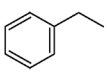	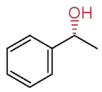	19,000 h^{-1}	133,000	5 h	319
Au-loaded anatase (5.0 g L^{-1})	H_2O	150 W halogen lamp (λ > 400 nm)	Not reported	UPO	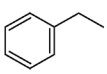	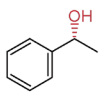	1,430 h^{-1} (estimated)	2,000	6 h	323
Au-loaded rutile (5.0 g L^{-1})				Immobilized UPO			4,200 h^{-1} (estimated)	21,000	120 h	
g-C_3N_4 (2.0 g L^{-1})	Methanol (2.5 M)	365 nm LED	0.99 mM h^{-1}	Immobilized UPO	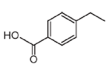	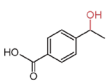	13,000 h^{-1}	130,000	4 h	325
	$NaHCO_2$ (250 mM)	200W halogen lamp	0.12 mM h^{-1}		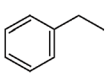	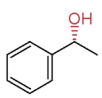	283 h^{-1} (estimated)	60,000	96 h	328
Flavin adenine mononucleotide (50 μM)	EDTA (1 mM)	200 W halogen lamp	Not reported	UPO	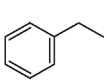	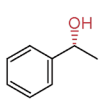	23,900 h^{-1}	11,500	5 h	212
					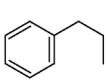	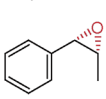	17,300 h^{-1}	4,730		
Au-loaded TiO_2 (5.0 g L^{-1})	Methanol (250 mM)	250 W halogen lamp	0.52 mM h^{-1}	UPO	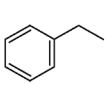	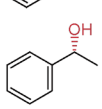	6,640 h^{-1}	71,000	72 h	327
MCC-functionalized InP/ZnSe/ZnS quantum dots (1.0 g L^{-1})	H_2O	Xe lamp (100 mW cm^{-2})	0.28 mM h^{-1}	UPO	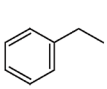	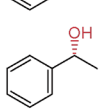	130,000 h^{-1}	173,000	12 h	330
					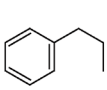	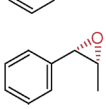	33,400 h^{-1}	54,000		
Artificial wood (10 g L^{-1})	H_2O	Xe lamp (100 mW cm^{-2})	0.59 mM h^{-1}	UPO	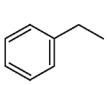	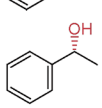	1,900 h^{-1}	45,300	32 h	334
					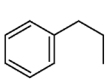	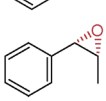	700 h^{-1}	16,500		
Stacked tubular polymeric carbon nitride (1.0 g L^{-1})	H_2O	Xe lamp (350 mW cm^{-2})	0.15 mM h^{-1}	CPO	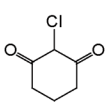	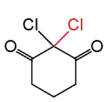	Cannot be estimated	Cannot be estimated	4 h	340

tica[304,305,309]). Upon illumination, these abiotic catalysts generated photoexcited electrons, which were transferred to membrane-bound redox proteins (e.g., cytochrome, ferredoxin, flavoprotein, [NiFe]-H_2ase)[305,310] of the acetogens. The electrons were then funneled into the intracellular redox enzymes (e.g., FDH, H_2ase, methylene-tetrahydrofolate reductase) within the Wood-Ljungdahl pathway, thereby achieving CO_2 valorization to acetate ($2CO_2 + 7H^+ + 8e^- \rightarrow CH_3COO^- + 2H_2O$).

https://doi.org/10.1021/acs.chemrev.5c01010
Chem. Rev. 2026, 126, 4857−4899

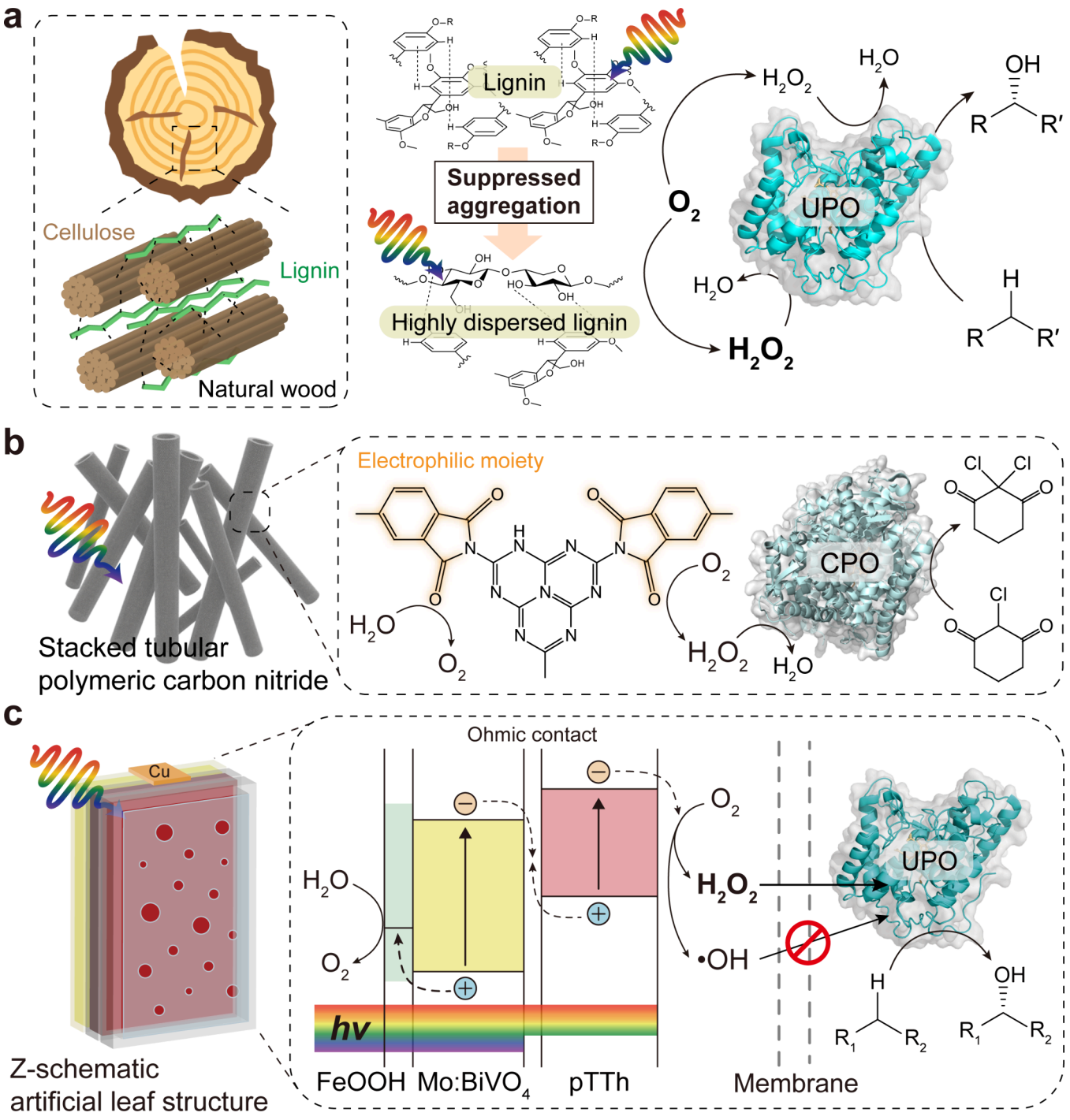

Figure 10. Photo(electro)catalytic materials and structures for efficient H_2O_2-dependent biocatalysis. (**a**) Lignin-cellulose composite photocatalyst for robust oxyfunctionalization.[334] Embedding kraft lignin into cellulose matrices suppresses lignin aggregation, improving redox-site accessibility for O_2-to-H_2O_2 conversion. (**b**) Structured carbon nitride for enhanced enzymatic halogenation.[340] Stacked tubular architecture and electrophilic moieties promote directional electron transfer and localized H_2O_2 delivery to H_2O_2-dependent peroxidase. (**c**) Z-schematic tandem device for sustainable biocatalysis.[350] A cellulose-membrane-separated artificial leaf allows H_2O_2 diffusion and blocks short-lived hydroxyl radicals (·OH). Abbreviations: FeOOH, ferric oxyhydroxide; Mo:BiVO$_4$, molybdenum-doped bismuth vanadate; pTTh, polyterthiophene; UPO, unspecific peroxygenase; CPO, chloroperoxidase.

Progress from sacrificial-donor-dependent schemes to water-oxidation-driven electron-supply approaches has propelled sustainable solar-to-chemical conversion in microbial biohybrids forward. In many biohybrid devices,[16,304−307] cysteine has been used because of its dual functionality: (i) electron donor for photocatalytic reactions (2Cysteine +2h$^+$ → Cysteine +2H$^+$),[311] given an oxidation potential of 0.08 V vs RHE and (ii) reducing agent to scavenge O_2 (4Cysteine + O_2 → 2Cystine +2H_2O),[312] thus maintaining anaerobic environments required for acetogenic metabolism. Beyond the consumptive process of cysteine, Sakimoto et al. recycled cystine back to cysteine using photoactive TiO_2 nanoparticles loaded with manganese phthalocyanine cocatalyst.[313] This recycling enhanced the continuity of electron transfer to

https://doi.org/10.1021/acs.chemrev.5c01010
Chem. Rev. 2026, 126, 4857−4899

Table 4. Comparative Assessment of NADH Regeneration and NADH-Dependent Biosynthesis in Photoelectrocatalytic Systems

Abiotic photoelectrocatalyst	Electron mediator	Electron donor	Light source	Electrical bias	Maximum NADH production rate	Maximum NADH yield	Target biocatalysis	Substrate	Product	Maximum TOF	Maximum TTN	ref.
Photoanode: $BiVO_4$ PV: $CH_3NH_3PbI_3$ perovskite Cathode: Carbon cloth (2 cm^2)	M_{ox} (0.5 mM)	Lignin (5 mg mL^{-1})	450 W Xe lamp (λ > 420 nm, 100 mW cm^{-2})	0 V	0.32 mM h^{-1}	71% (1 h)	FDH-catalyzed CO_2-to-formate	CO_2		17.9 h^{-1} (estimated)	Cannot be estimated	60
Photoanode: FeOOH/$BiVO_4$ PV: Cu(In, Ga)Se_2 Cathode: mesoITO (1 cm^2)	M_{ox} (0.5 mM)	H_2O	Xe lamp (λ > 400 nm, 100 mW cm^{-2})	0 V	1.21 mM h^{-1}	72% (3 h)	FDH-catalyzed CO_2-to-formate	CO_2		5.8 h^{-1} (estimated)	271 (estimated)	61
Photoanode: Ta_3N_5 nanotubes Cathode: g-C_3N_4 thin film (4.0 cm^2)	None	H_2O	100W Xe lamp (100 mW cm^{-2})	1.0 V vs RHE	Cannot be estimated	Cannot be estimated	FDH-catalyzed CO_2-to-formate	CO_2		36.3 h^{-1} (estimated)	199 (estimated)	354
Photoanode: CoPi/$BiVO_4$ Cathode: Rh-viologen /polyterthiophene (1 cm^2)	Anchored M_{ox} (15.8 μM)	H_2O	150 W Xe lamp (λ > 420 nm, 100 mW cm^{-2})	0 V	0.0425 mM h^{-1}	25.5% (3 h)	GDH-catalyzed α-ketoglutarate-to-L-glutamate		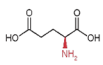	123 h^{-1} (estimated)	246 (estimated)	341
Photoanode: FeOOH/$BiVO_4$ PV: Triple cation perovskite Cathode: Carbon nanotube film (1 cm^2)	M_{ox} (0.5 mM)	H_2O	450W Xe lamp (λ > 420 nm, 100 mW cm^{-2})	0 V	2.4 mM h^{-1}	58% (1 h)	GDH-catalyzed α-ketoglutarate-to-L-glutamate		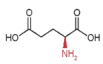	6,200 h^{-1}	108,000	342
Photoanode: CdS PV: Triple cation perovskite Cathode: Carbon paper (2.25 cm^2)	M_{ox} (1 mM)	$K_4[Fe(CN)_6]$	300W Xe lamp (λ > 400nm)	0 V	0.6 mM h^{-1}	49% (90 min)	LDH-catalyzed pyruvate-to-lactate	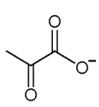	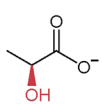	18,200 h^{-1} (estimated)	62,200 (estimated)	355
Anode: Pt Photocathode: Polyterthiophene (0.6 cm^2)	M_{ox} (0.25 mM)	H_2O	Xe lamp (100 mW cm^{-2})	0.1 V vs RHE	0.94 mM h^{-1}	93.3% (3 h)	GDH-catalyzed α-ketoglutarate-to-L-glutamate		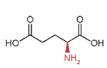	Cannot be estimated	Cannot be estimated	348
Photoanode: α-Fe_2O_3 PV: Silicon Cathode: mesoITO (1 cm^2)	M_{ox} (1 mM)	Lignin (1 mg mL^{-1})	450 W Xe lamp (λ > 400 nm, 100 mW cm^{-2})	0 V	0.49 mM h^{-1}	Cannot be estimated	OYE-catalyzed asymmetric hydrogenation of C=C bonds	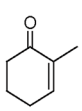	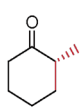	650 h^{-1}	1,250	343
Photoanode: Zr: α-Fe_2O_3 Cathode: Carbon fiber paper (1 cm^2)	M_{ox} (0.25 mM)	PET microplastics (50 mg mL^{-1})	Xe lamp (100 mW cm^{-2})	1.0 V vs RHE	Cannot be estimated	Cannot be estimated	GDH-catalyzed α-ketoglutarate-to-L-glutamate		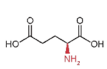	6,700 h^{-1}	144,000	349
							OYE-catalyzed asymmetric hydrogenation of C=C bonds	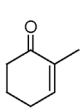	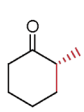	420 h^{-1}	1,300	349
Anode: Carbon felt Photocathode: Organic photovoltaic/Indium tin oxide-Carbon Felt (0.25 cm^2)	CO_2	H_2O	Xe lamp (100 mW cm^{-2})	0.8 V vs RHE	Cannot be estimated	Cannot be estimated	ADH-catalyzed acetophenone-to-chiral 1-phenylethanol		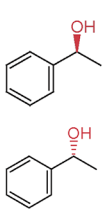	1,200 h^{-1}	12,000	181

sustain biosolar acetate production. Furthermore, water-oxidizing Z-scheme sheet (a pair of $SrTiO_3$ and $BiVO_4$-based particles) has been substantiated to drive microbial CO_2-to-acetate under solar light (AM 1.5G).[234] This reaction scheme eliminated the reliance on sacrificial electron donors, thereby advancing the development of fully integrated biohybrid photosynthetic platforms.

4.3. Peroxide-Driven Biocatalysis through Photocatalytic H_2O_2 Provision

Unspecific peroxygenases (UPOs) catalyze enantioselective oxyfunctionalization of C−H and C═C bonds via the peroxide-shunt pathway.[2,314−321] They directly consume H_2O_2 at a heme-thiolate active site to generate the high-valent oxoferryl-porphyrin π-cation radical (i.e., Compound I), which triggers hydrogen-atom abstraction and oxygen-rebound oxygenation of substrates. By contrast, electron-dependent redox

https://doi.org/10.1021/acs.chemrev.5c01010
Chem. Rev. 2026, 126, 4857−4899

enzymes such as FDH, H_2ase, ene-reductase, NrfA, and MMOH rely on external reducing equivalents (e.g., NAD(P)H, NADH analogues, $FMNH_2$) or DET partners (e.g., photocatalysts) to supply electrons to their active centers and thereby drive redox chemistry through conventional electron-transfer chains. Consequently, UPOs operate through a mechanistically distinct pathway as H_2O_2-mediated, stand-alone oxygen transfer catalysts. However, UPOs are susceptible to irreversible transformation of their heme groups to catalytically inactive species (e.g., α-meso-hydroxyheme, verdoheme, biliverdin) at elevated H_2O_2 concentrations.[314,322−326] To overcome this limitation, *in situ* provision of H_2O_2 at low but sufficient concentrations for sustained UPO catalysis appears to be the most promising solution. Various semiconducting and molecular photocatalysts (e.g., gold-loaded rutile TiO_2, graphitic C_3N_4, methylene blue, FMN, phenosafranine)[212,327−330] have been reported to achieve O_2 reduction to H_2O_2 (eq 22):

$$O_2 + 2e^- + 2H^+ \rightarrow H_2O_2, \quad E_{red} = 0.68\ V\ vs\ RHE \tag{22}$$

Those photocatalysts enabled the hydroxylation of multiple organic substrates [e.g., (cyclo)alkanes and alkyl arenes] mediated by the UPO from *Agrocybe aegerita*, which was expressed recombinantly in *Pichia pastoris* (r*Aae*UPO) (Table 3). These photocatalyst/UPO hybrids achieved TTNs from ∼10,000 to ∼70,000 at the cost of artificial electron donors (e.g., methanol, formate, NADH).[327−329]

Using H_2O as both the solvent and the electron donor in solar-driven synthesis offers an attractive route toward sustainable H_2O_2 generation and UPO catalysis. This approach enhances atom economy[323,331] and prevents the accumulation of oxidized artificial electron donors, which otherwise can lead to undesirable side reactions (e.g., competitive parasitic redox pathways,[332] accelerated charge recombination of photocatalyst, and back electron transfer from photocatalyst to oxidized electron donor[333]). Gold-loaded TiO_2 (anatase phase), for example, reduced O_2 to H_2O_2 at the expense of H_2O under visible light ($\lambda > 400$ nm) (Table 3).[323] However, TiO_2-driven oxidation of H_2O inevitably generated hydroxyl radicals ($^{\bullet}OH$) that caused heme destruction[322] and consequent irreversible inactivation of UPO. To mitigate $^{\bullet}OH$-mediated deactivation of UPO, Kim et al. presented antioxidant lignin photocatalysts (e.g., kraft lignin, lignosulfonate) for biosolar oxygenation.[314] During lignin-sensitized oxidation of

H_2O to O_2 and H_2O_2, the phenolic moieties of lignin served as $^{\bullet}OH$ scavengers, thereby mitigating heme oxidation and preserving the catalytic activity of r*Aae*UPO. The study has advanced to the creation of artificial wood (lignin-cellulose complexes) that suppressed lignin aggregation problem through hydrogen bonding with cellulose.[334] This structural dispersion increased the exposure of redox-active motifs, which, in turn, boosted photocatalytic H_2O_2 generation and r*Aae*UPO turnover (Figure 10a and Table 3).

In a similar way to UPOs, chloroperoxidase (CPO) has been integrated with photocatalysts for biosolar halogenation reactions. CPO uses H_2O_2 as an oxygen source to catalyze halogenation through H_2O_2-shunt pathway.[335−338] Water-soluble anthraquinone sulfonate has been identified as a homogeneous photocatalyst that (i) generated H_2O_2 from O_2 in the presence of methanol as an electron donor and (ii) activated CPO with a TTN of 318,000 over 30 h.[339] The photocatalytic mechanism of anthraquinone avoided the formation of long-lived radical species that are known to damage CPO, leading to high productivity and long operational stability. Similarly, CPO was noncovalently immobilized onto carbon nitride polymeric photocatalysts for chlorination reactions under simulated solar light (AM 1.5G, 350 mW cm^{-2}) (Figure 10b and Table 3).[340] The intimate CPO-material interface shortened the diffusion path for photogenerated H_2O_2, resulting in a 3.5-fold enhancement in the conversion yield.

5. PHOTOELECTROCATALYTIC SYSTEM FOR REDOX BIOTRANSFORMATION

5.1. Mediated Charge Coupling of Abiotic Materials with Biocatalysts

Photoelectrocatalytic devices use band-selective photoanodes (e.g., $BiVO_4$, α-Fe_2O_3, TiO_2) in combination with complementary (photo)cathodes (e.g., mesoporous ITO, carbon nanotube, NiO, polythiophene, $BiFeO_3$).[61,215,341−348] These configurations funnel photoexcited electrons through mediated electron transfer to regenerate NAD(P)H (Table 4), $FMNH_2$, or $MV^{\bullet+}$. A key advantage of photoelectrochemical cells is the spatial separation of anodic and biocathodic sites, which provides the stability of flavin- and viologen-based mediators against reoxidation by photoanodically generated O_2. Furthermore, biosolar photoelectrochemical devices have demonstrated dual productivity by enabling chemical synthesis at both electrodes. For example, cathodic regeneration of coenzymes was coupled with value-adding anodic oxidations [e.g., conversion of post-consumer poly(ethylene terephthalate) into formate and acetate].[349]

5.1.1. Photoelectrocatalytic Regeneration of Nicotinamide Coenzymes. Photoelectrocatalytic methods offer delicate control over E_{qF} by applying an electrical bias. This tunability enables precise modulation of the redox environment at the electrode surface. Such control promotes selective hydride transfer via metal-based oxidants and enables highly selective regeneration of enzymatically active 1,4-NAD(P)H.[351] The anodic half-reaction proceeds independently at the (photo)anode, eliminating the need for costly sacrificial electron donors (e.g., TEOA, EDTA, ascorbic acid) that are commonly required in photocatalytic systems. This feature improves the atom economy and reduces waste generation. Furthermore, the external bias can expand the reaction scope of photoelectrocatalytic devices. By shifting the E_F of a (photo)anode to more positive potentials and enhancing charge separation via modulation of band bending, photoelectrocatalytic systems can drive thermodynamically and kinetically challenging oxidation reactions, such as H_2O oxidation (eq 23):

$$2H_2O \rightarrow O_2 + 4H^+ + 4e^-, \quad E_{ox} = 1.23\ V\ vs\ RHE \tag{23}$$

Notably, the use of conductive electrodes decouples light absorption from redox potential control, allowing oxidation reactions beyond the intrinsic photophysical limitations of photocatalysts.

Many photoelectrocatalytic systems use H_2O as an electron donor to regenerate NAD(P)H because of its high abundance (55.55 M).[303] Several photoelectrocatalytic devices have demonstrated H_2O oxidation using oxide or nitride-based photoanodes for solar NAD(P)H regeneration.[352−354] Under

https://doi.org/10.1021/acs.chemrev.5c01010
Chem. Rev. 2026, 126, 4857−4899

simulated solar light and applied electrical bias (1.0 to 1.2 V), the photoanodes (e.g., $BiVO_4$, α-Fe_2O_3, Ta_3N_5, CdS)[61,341,342,352,354−357] extracted electrons from H_2O and transferred them to (photo)cathodes (e.g., polyterthiophene, mesoporous indium tin oxide)[61,341] to reduce $NAD(P)^+$ to NAD(P)H, subsequently achieving NAD(P)H-dependent enzymatic transformation (e.g., CO_2 reduction,[61,352,354] reductive amination[353]). Among various photoanode materials, $BiVO_4$ has been widely adopted because of small effective masses of charges, suitable band-edge positions, and high photostability in neutral conditions.[49,358]

Photoelectrocatalytic systems often require an electrical bias because the sum of V_{th} of the redox couple [i.e., H_2O oxidation and **M**-mediated NAD(P)H regeneration (1.34 V)] and overpotential is larger than the V_{ph} of photoanodes. To avoid the external electrical bias, Park and colleagues used a photovoltaic cell to provide a supplementary V_{ph} (Table 4).[61,342] In this tandem architecture, photogenerated electrons from H_2O oxidation at a FeOOH|$BiVO_4$ photoanode migrated through the circuit to mesoporous cathodes [e.g., indium tin oxide (ITO),[61] carbon nanotube film[342]], where they reduced $\mathbf{M}_{ox}$ at the electrode−electrolyte interface; the mesoporous morphology enlarged the electrochemically active surface, thereby accelerating interfacial charge transfer. The regenerated NADH subsequently powered glutamate dehydrogenase (GDH) and FDH for bias-free amination and CO_2 reduction, respectively.

Despite the proof-of-concept success, such a platform still relies on freely diffusing noble-metal mediators (i.e., **M**), which account for a disproportionate share of the projected cost and complicate downstream separation. Inspired by the immobilized organization of redox cofactors within the thylakoid membrane, Zhao et al. attached **M** to the surface of polythiophene-based photocathode via hydrophobic self-assembly, forming lipid-bilayer-like arrangements (Table 4).[341] Anchoring the catalyst in a nanoscale, ordered domain enforced directional electron flow from the semiconductor to $\mathbf{M}_{ox}$, decreased the amount of **M** loading, and minimized the leaching of its Rh center. The surface-tethered redox mediator exhibited an apparent TOF of 179 h^{-1} for NADH regeneration, enabling the sustainable GDH-catalyzed amination of C═O bonds. This study underscores that the construction of leak-free redox layers via catalyst-interface engineering can reduce system cost without compromising catalytic performance in biosolar manufacturing.

In addition to these advances in the reductive half-reaction, substantial progress has been made on the oxidative side through the implementation of alternative anodic reactions. Replacing water with energy-rich wastes circumvents the kinetic barrier of four-electron O_2 evolution, in parallel upgrading low-value feedstocks into commercially relevant coproducts. For example, a bias-free tandem device—consisting of an α-Fe_2O_3 photoanode with a Si/mesoporous ITO photocathode—extracted electrons from kraft lignin under 1-sun illumination (Figure 4c and Table 4).[343] The dual-absorbing system generated sufficient V_{ph} to (i) drive lignin oxidation into aromatic compounds, (ii) extract electrons more rapidly than from water oxidation, and (iii) accelerate ene-reductase-catalyzed asymmetric hydrogenation. This approach was further broadened to harness solid plastic waste as an electron source.[349] A Zr-doped hematite photoanode enabled rapid electron extraction from hydrolyzed poly(ethylene terephthalate) microplastics derived from real-world samples (Figure 4c and Table 4). This, in turn, boosted NADH-dependent enzymatic modules—GDH and ene-reductase—achieving TTNs of 144,000 and 1,300, respectively. These values exceeded those of water-fueled controls by 1−2 orders of magnitude. Collectively, these works highlight the dual benefits of environmental remediation and value-added synthesis.

Rh-based **M** complexes suffer from some undesired side reactivities such as the parasitic proton reduction that diverts electrons to H_2[359] and the mutual inactivation with biocatalysts[360] due to strong interactions between $\mathbf{M}_{ox}$ and nucleophilic amino acid residues within the enzymes.[361] These drawbacks have motivated the search for alternatives to **M**. A compelling solution is the use of enzyme-only $CO_2/HCOO^-$ redox loop recently devised by Reisner and colleagues (Figure 7d and Table 4).[181] In this design, a [W]-FDH from *Nitratidesulfovibrio vulgaris* Hildenborough (*Nv*HFDH) reduces CO_2 to formate (eq 24), and simultaneously a NAD^+-dependent FDH from *Candida boidinii* (*Cb*FDH) oxidize formate to regenerate NADH from NAD^+ (eq 25), thus replacing the Rh hydride as a transferable hydride reservoir:

$$NvHFDH + CO_2 + H^+ + e^- \rightarrow NvHFDH + HCOO^- \quad (24)$$

$$CbFDH + HCOO^- + NAD^+ \rightarrow CbFDH + CO_2 + NADH \quad (25)$$

Co-immobilizing dual FDH enzymes on a mesoporous ITO layer deposited on carbon felt—electrically wired to an organic-photovoltaic photocathode—elevated NADH turnover number to 8,400 h^{-1}, which is a 230-fold enhancement over Rh-based benchmark (36 h^{-1}). The regenerated cofactor seamlessly drove alcohol dehydrogenases to furnish enantioenriched 1-phenylethanol under 1-sun irradiation, thereby establishing the $CO_2/HCOO^-$ couple as a sustainable, precious-metal-free hydride shuttle for photoelectrochemical biocatalysis.

5.1.2. Photoelectrocatalytic Recycling of Flavin Coenzymes. Photoelectrocatalytic devices offer a promising route for the regeneration of flavin-based coenzymes. By applying electrical energy, the redox environment at the (photo)cathodic compartment can be precisely tuned to generate reduced flavin species (e.g., flavin semiquinone or flavin hydroquinone) in a selective manner. Moreover, spatial separation of oxidation and reduction sites enables the use of H_2O as a sustainable electron donor, and suppresses the detrimental diffusion of O_2 to flavin molecules. This approach is advantageous given the inherent complexities of flavin redox chemistry—including multiple proton-coupled electron transfer steps, transient semiquinone formation, high sensitivity to O_2, and susceptibility to direct photoreduction by sacrificial electron donors (e.g., EDTA, TEOA)—which have posed challenges for efficient photocatalytic regeneration in a single reaction compartment platform.

Several photoelectrocatalytic platforms have been reported to enable FMN reduction with H_2O as an electron feedstock, thereby driving flavoenzyme-catalyzed hydrogenation of C═C bonds.[345,346] Under light illumination and external electrical bias, O_2-evolving $BiVO_4$-based photoanodes oxidized H_2O to extract electrons in an anodic compartment, and transferred solar-powered electrons to FMN via conductive carbon nanotube hybrid film. The reduced form of FMN directly

https://doi.org/10.1021/acs.chemrev.5c01010
Chem. Rev. 2026, 126, 4857−4899

provided the electrons to the flavin prosthetic group of *Ts*OYE, subsequently achieving asymmetric *trans*-hydrogenation of ketoisophorone to (*R*)-levodione with high FE (~81%) and ee (>80%). Importantly, the physical separation of the H_2O-oxidizing anode compartment and the $FMNH_2$-generating cathode compartment minimized the extent of O_2 crossover, thereby ensuring stable and high current efficiency. Furthermore, this compartmentalized configuration was extended to dual enzymatic transformations at cathodic and anodic interfaces.[346] Under the setup, anodic water oxidation proceeded predominantly through the two-electron pathway to generate H_2O_2 rather than the four-electron O_2-evolution pathway. The *in situ* photogenerated H_2O_2 subsequently activated r*Aae*UPO for the enantioselective oxyfunctionalization of ethylbenzene to (*R*)-1-phenylethanol. Together, these works demonstrate the feasibility of a nature-inspired configuration that separates the H_2O-oxidizing light reaction and FMN-regenerating dark reaction to achieve stable coenzyme recycling in flavin-dependent enzymatic reactions.

5.1.3. Photoelectrocatalytic Rejuvenation of Viologen Mediators. Photoelectrocatalytic architectures provide a distinct advantage over particulate photocatalytic systems for the regeneration of viologen derivatives by spatially decoupling MV^{2+} reduction from H_2O-to-O_2 conversion, thereby enabling continuous $MV^{\bullet+}$ production with H_2O as the electron donor. By circumventing the intrinsic instability of reduced viologens—which are otherwise readily oxidized by O_2 under aerobic conditions[362] this strategy establishes a level of robustness not attainable under purely photocatalytic conditions. For instance, a water-oxidizing TiO_2 photoanode has been integrated with a carbon felt cathode for MV^{2+} reduction and FDH activation in a two-compartment setup.[347] Under UV−visible light (λ > 300 nm) and without external electrical bias, photoexcited electrons migrated through the external circuit to the cathode, reducing MV^{2+} to $MV^{\bullet+}$. The radical cation bound tightly to *Cb*FDH, which in turn catalyzed the two-electron reduction of CO_2 to formate. However, the production rate was only 31.9 nmol h^{-1} under bias-free conditions because of the sluggish electron transfer from the cathode to the MV^{2+}.

The kinetic bottleneck has been alleviated by immobilizing MV^{2+} on the cathode because the tethering strategy transforms electron transfer from a diffusion-limited to a surface-confined process, thereby improving the heterogeneous rate constant, and increases the local concentration of viologens at the electrode−electrolyte interface. Cheng et al. coated viologen-containing redox polymer onto a dye-sensitized mesoporous NiO photocathode, which facilitated rapid extraction of photoexcited electrons, suppressed charge recombination, and prevented H_2ase leaching (Figure 8c).[215] Consequently, the biocatalytic photoelectrochemical device exhibited a high solar-to-hydrogen efficiency of 0.124% and stable operation for 10 h. Similarly, Schuhmann and co-workers deposited a viologen-functionalized poly(ethylene-imidazole) film on a photocathode consisting of a gold electrode coated with an osmium-based redox polymer and photosystem I.[363] By entrapping [NiFeSe]-H_2ase within a surface-confined viologen conduit, these assembled biophotocathodes produced bias-free photocurrents (up to 60 μA cm^{-2}) and sustained H_2 evolution without enzyme leaching.

5.2. Photoelectrocatalytic Devices for Direct Activation of Biocatalysts

5.2.1. Photoactivation of Metalloenzymes. As discussed in Section 4.2, achieving DET without using costly coenzymes and mediators remains a major challenge in solar-driven biotransformation. A persistent issue is the intrinsic limitations of many photocatalysts, such as rapid charge recombination and sluggish kinetics in oxidative half-reactions, which hinder efficient interfacial electron transfer to redox-active prosthetic groups (e.g., flavins, hemes, metal clusters). Photoelectrocatalytic systems offer an advantage of using an external electrical bias that accelerates the separation and transfer of photoexcited charges, thereby promoting directional charge injection into prosthetic groups. Leveraging this principle, a diverse range of photoelectrocatalysis-based strategies and device architectures have been developed to overcome the inherent barriers of DET in biocatalytic systems and enhance the efficiency of solar-to-chemical energy conversion.

The Reisner group has made pioneering contributions to the development of photoelectrocatalytic devices capable of directly activating oxidoreductases (e.g., FDH and H_2ase) for fuel synthesis. In their early work, the group demonstrated photoelectrocatalysis-driven H_2 evolution via DET to [NiFeSe]-H_2ase from *Desulfomicrobium baculatum*,[54,364] a redox enzyme distinguished by its high proton reduction activity, O_2 tolerance, and negligible inhibition by H_2.[250] Specifically, the group designed a photobiocathode comprising a p-type silicon photocathode coated with an amorphous TiO_2, which enabled DET to H_2ase.[54] The TiO_2 layer protected the silicon from oxidative degradation and served as a biocompatible interface for H_2ase immobilization, as well, facilitating DET to the distal metallocofactor (i.e., Fe−S cluster). This photobiocathode achieved H_2 evolution with a FE of 96% under white light. However, external electrical bias (0 V vs RHE) was needed because the generated V_{ph} was insufficient to fully drive the reductive biocatalysis.

To overcome the limited V_{ph} of single-absorbing design, the same group devised a dye-sensitized, semiartificial photoelectrocatalytic architecture for solar fuel synthesis (e.g., H_2, formate) via DET.[110] Electronic wiring of green-light-absorbing diketopyrrolopyrrole dye to photosystem II-modified photoanode with an osmium-complex redox polymer facilitated harvesting of broad-spectrum solar light to oxidize H_2O. This complementary dual-absorber transferred photoexcited electrons through the redox polymer to the distal Fe−S cluster of [NiFeSe]-H_2ase on an inverse-opal ITO biocathode, driving H_2 generation with a solar-to-fuel efficiency of 0.14% under visible light (λ > 420 nm). A similar photoanodel photocathode device—featuring a dye-sensitized, photosystem II-based photoanode—was further used to reduce the overpotential for direct transfer of water-derived electrons to [Fe_4S_4] metallocofactor in W-containing FDH from *Desulfovibrio vulgaris*.[276] Operated under visible light (λ > 420 nm) with a modest external bias of 0.3 V, this semiartificial Z-scheme selectively converted CO_2 to formate with a FE of 70%, although prolonged illumination (>1 h) caused an irreversible decline in photocurrent due to photodegradation of both photosystem II[365] and the photosensitized dye.

In addition to the organic-based photoelectrocatalytic devices, Kuk et al. designed an inorganic oxide-based, dual light-absorber tandem structure by wiring $CuFeO_2$|CuO photocathode and FeOOH-coated $BiVO_4$ photoanode.[53]

https://doi.org/10.1021/acs.chemrev.5c01010
Chem. Rev. 2026, 126, 4857−4899

Illumination with visible light (λ > 420 nm) solely endowed the photoanode|photocathode tandem with a V_{ph} of ~1.9 V, sufficient to drive abiotic CO_2-to-formate conversion concomitant with water oxidation (eq 26).

$$4CO_2 + 2H_2O \rightarrow 4HCOO^- + O_2, \quad V_{th} = 1.272\ V \tag{26}$$

The abiotic photocathode was further transformed into a photobiocathode by introducing an electron-transporting TiO_2 overlayer and FDH from *Clostridium ljungdahlii* (*Cl*FDH). This Z-scheme-inspired tandem cell exhibited a stable photocurrent for >12 h and DET-type formate production (0.098 μmol h^{-1} over 24 h). Collectively, these advances established a durable dual-absorber platform for fully solar-powered enzymatic CO_2 reduction.

Apart from the dual photoelectrode configurations (i.e., photoanode|photocathode), the photovoltaic-photoelectrocatalytic structure facilitates fuel synthesis using light and H_2O as the sole energy and electron source, respectively. Triple-cation mixed-halide perovskites have emerged as promising PV materials due to their high V_{ph} (>0.9 V), power conversion efficiencies (up to 25.2%), and low production costs.[366,367] The Park group coupled the triple-cation perovskite photovoltaic cell with a tandem structure consisting of $BiVO_4$-based photoanode and a 3D-structured TiN cathode that provided high porosity and electrical conductivity for effective *Cl*FDH loading and DET to *Cl*FDH.[108] The unbiased photoelectrochemical device enabled DET-based, FDH-catalyzed CO_2 reduction under visible light (λ > 420 nm), achieving 1.06 μmol h^{-1} of formate production rate and solar-to-formate conversion efficiency of 0.08% for 8 h. However, the production rate dropped to 0.5 μmol h^{-1} within 24 h because of the instability of organometallic perovskite materials under humid conditions. A separate study alleviated the instability issue of perovskite by encapsulating the photoabsorber within a graphite-epoxy matrix.[107] When $BiVO_4$|perovskite|TiO_2-based tandem device was immersed in water, the encapsulated perovskite retained sufficient V_{ph} to activate H_2ase and FDH from *Desulfovibrio vulgaris* Hildenborough via DET. As a result, the bias-free device achieved solar-to-fuel conversion efficiencies from 0.8 to 1.1% with sustained activity over 10 h. Collectively, the photovoltaic-integrated tandem photoelectrochemical devices enabled bias-free solar fuel production via DET to redox enzymes, offering higher efficiencies than photoanode|photocathode systems.

The integration of a thermoelectric generator in series with photoelectrocatalytic device extended solar harvesting beyond the UV−visible range, reaching into the infrared to provide broader spectral input for biocatalysis (Figure 9d).[20] Because most semiartificial photosynthetic approaches rely on UV−visible light absorbers, the remaining solar energy is lost as unabsorbed infrared radiation and thermalization heat. The thermoelectric generator converted the infrared-induced heat into additional voltage via the Seebeck effect, realizing unbiased CO_2-to-formate conversion with a solar-to-formate conversion efficiency of 0.032% under 3-sun illumination (AM 1.5G). This work showcases thermo-electrochemical coupling as a viable route to extend solar utilization beyond the limits of conventional biocatalytic photoelectrochemical devices.

Although H_2O serves as an electron donor in most biocatalytic photoelectrochemical systems, organic molecules (e.g., alcohols, microplastics)[368−370] can work as electron feedstocks for enzyme-mediated solar-to-fuel conversion. Compared to H_2O oxidation, oxidizing organic molecules offers a thermodynamically and kinetically more favorable pathway that simultaneously (i) accelerates DET to reductive biocatalysts and (ii) produces value-added oxidation products rather than O_2. For example, alcohols [e.g., 4-methylbenzylalcohol,[368] 5-(hydroxymethyl)furfural),[368] plastic-derived ethylene glycol[369]] have been employed as electron donors. These organics were used in single light-absorber photoelectrocatalytic devices for FDH-mediated CO_2 reduction (Figure 4c). Within these biosolar devices, organocatalysts (e.g., silatrane-modified nitroxyl radical[368]) or metal alloys (e.g., $Cu_{27}Pd_{73}$[369]) selectively oxidized alcohols or ethylene glycol to aldehydes or glycolate (FEs > 96%), respectively. Concurrently, the electrons generated from these oxidation reactions were consumed during CO_2-to-formate conversion with FEs of 74 to 95%. Another example is a tandem photoelectrocatalytic device developed to produce formate (11 μmol h^{-1}) at both anodic and cathodic sites through concurrent reformation of poly(ethylene terephthalate) and enzymatic CO_2.[371]

Expanding the biosolar conversion system toward real-world applications, the Reisner group developed a modular and scalable biohybrid photoelectrocatalytic device by assembling ITO nanoparticles onto a cyanamide-functionalized carbon nitride support.[22] Unlike typical laboratory-scale systems, this 50 cm^2 carbon nitride photoelectrocatalytic sheet device enabled bias-free CO_2-to-formate conversion via DET to FDH under natural sunlight, producing 0.2 mmol of formate over 3 days of outdoor operation. This work is a door-opener for the real-world deployment of scalable enzyme-integrated photoelectrocatalytic systems.

5.2.2. Photoelectrochemical Transfer of Electrons to Bacteria. Analogous to enzyme photoactivation, photoelectrochemical devices have driven microbial chemical synthesis by transferring photogenerated electrons directly to electrotrophic microorganisms. For instance, electrotroph *Sporomusa ovata* has been interfaced with transition-metal catalysts (e.g., Ni, Pt) on TiO_2-coated silicon nanowire catalysts.[105,106,372−375] The nanowire morphology facilitated the formation of extensive electronic junctions between cell-surface redox moieties and semiconducting electrodes, thereby promoting efficient electron transfer to the acetogen, enhancing cell density on the abiotic materials, and ultimately boosting microbial CO_2 valorization.[376] As a demonstrative example, a TiO_2 nanowire photoanode was integrated with an n^+p-silicon junction/TiO_2/Ni/*Sporomusa ovata* hybrid photocathode, which established the Z-scheme architecture analogous to natural photosynthesis.[106] In this configuration, the overall V_{ph} of the two light absorbers (i.e., Si and TiO_2) was sufficient to furnish the thermodynamic driving force required for bias-free coupling of H_2O oxidation and CO_2 conversion to acetic acid ($2CO_2 + 2H_2O \rightarrow CH_3COOH + 2O_2$, V_{th} = 1.09 V). This biosolar device achieved an acetate partial current of −0.26 mA cm^{-2} and a solar-to-acetate efficiency of 0.38% under a solar light (AM 1.5 G).

The biosolar CO_2-to-C_2 conversion was further coupled with a kinetically facile, low-overpotential organic oxidation, thereby enhancing the acetate partial current. The Yang group designed a photobiochemical diode comprising an n^+p-silicon junction/TiO_2/Pt/*Sporomusa ovata* photobiocathode and a p^+n-silicon junction/TiO_2/Pt−Au photoanode.[56] Under red light (λ: 740 nm), the photoanode oxidized glycerol with a low onset potential of −0.05 V vs RHE, and simultaneously transferred electrons to the photobiocathode. These electrons

https://doi.org/10.1021/acs.chemrev.5c01010
Chem. Rev. 2026, 126, 4857−4899

Table 5. Peroxide-Mediated Activation of Biocatalysts in Photoelectrocatalytic Platforms

Photoelectro catalyst	Electron donor	Light source	Electrical bias	H_2O_2-synthetic reaction	Initial H_2O_2 production rate	Biocatalyst	Substrate	Product	Maximum TOF	Maximum TTN	Reaction time length	ref.
Photoanode: Mo:$BiVO_4$ PV: Silicon Cathode: α-Fe_2O_3 (1 cm^2)	H_2O	450 W Xe lamp (100 mW cm^{-2})	0 V	H_2O oxidation	0.84 mM h^{-1}	UPO	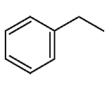	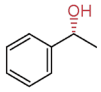	8,340 h^{-1}	41,700	6 h	59
Photoanode: Zr:α-Fe_2O_3 Cathode: Anthraquinone-2-carboxylic acid-anchored carbon fiber paper (1 cm^2)	PET microplastics (50 mg mL^{-1})	Xe lamp (100 mW cm^{-2})	0.9 V vs RHE	O_2 reduction	1.85 mM h^{-1}	UPO	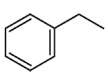	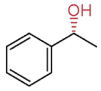	45,000 h^{-1}	271,000	7 h	349
							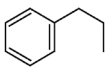	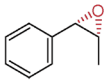	64,000 h^{-1}	362,000		
Photoanode: Mo:$BiVO_4$ Cathode: Inverse opal indium tin oxide (1.5 cm^2)	H_2O	Xe lamp (λ > 400 nm, 100 mW cm^{-2})	0.8 V vs RHE	H_2O oxidation	3.42 mM h^{-1}	UPO	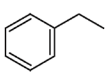	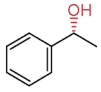	5,000 h^{-1} (estimated)	10,000 (estimated)	2 h	346
Photoanode: $BiVO_4$ PV: Cu(In, Ga)Se_2 Cathode: Carbon nitride/reduced graphene oxide (1 cm^2)	H_2O	Xe lamp (λ > 420 nm, 100 mW cm^{-2})	0 V	O_2 reduction	5.6 mM h^{-1}	UPO	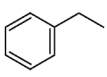	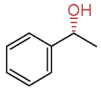	46,400 h^{-1}	43,300	4 h	379
Photoanode: FeOOH/Mo:$BiVO_4$ Photocathode: Polyterthiophene (1 cm^2)	H_2O	Xe lamp (100 mW cm^{-2})	0 V	O_2 reduction	0.363 mM h^{-1}	UPO	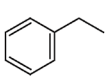	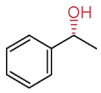	28,100 h^{-1}	128,000	8 h	350
							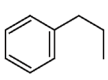	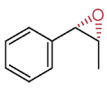	47,200 h^{-1}	193,000		
Anode: Pt Photocathode: Flavin-SWNT (1 cm^2)	H_2O	450 W Xe lamp (λ > 420 nm, 100 mW cm^{-2})	0.22 V vs RHE	O_2 reduction	0.37 mM h^{-1}	UPO	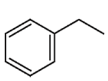	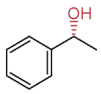	3,100 h^{-1} (estimated)	124,000	40 h	301
						CPO	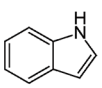	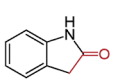	122 h^{-1} (estimated)	4,900		
Photoanode: H:TiO_2 Cathode: Co-N/carbon nanotube (2 cm^2)	H_2O	150 W Xe lamp (100 mW cm^{-2})	0 V	O_2 reduction	1.00 mM h^{-1} (estimated)	Lignin peroxidase	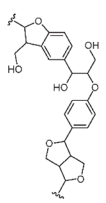	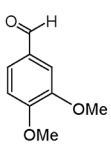	130 h^{-1} (estimated)	590 (estimated)	6 h	380

were subsequently utilized by *Sporomusa ovata* to drive the microbial valorization of CO_2 to acetate, yielding an acetate partial current of −1.04 mA cm^{-2}. The integrated device leverages natural metabolic pathways to enable sustainable solar-to-fuel conversion.

5.3. H_2O_2-Mediated Biocatalysis Enabled by Biosolar Devices

Along with the use of photocatalysis for the activation of cofactor-independent redox enzymes (discussed in Section 4.3), photoelectrocatalytic devices can drive H_2O_2-dependent biotransformations catalyzed by UPOs, CPOs, and peroxidases with TTNs exceeding 10^5 (Table 5). In contrast to *in situ* photocatalytic H_2O_2 generation, the modulation of photoelectrodes' E_F by applying external bias can selectively reduce O_2 to H_2O_2 via a two-electron pathway rather than to H_2O via a four-electron pathway. This approach supplies the enzymes with adequate concentrations of H_2O_2 while avoiding oxidative inactivation of their heme active sites.[377−379] Accordingly, the application of optimal electrical bias on photoelectrodes minimized the accumulation of $^{\bullet}OH$ from H_2O_2 reduction (eq 27) that readily occurs at higher potentials.[44]

$$H_2O_2 + e^- \rightarrow {}^{\bullet}OH + OH^-, \quad E_{red} = 0.79\ V\ vs\ RHE \tag{27}$$

Photoelectrochemical production of H_2O_2 from O_2 has been attained through (i) carbon-based (photo)cathode (e.g., graphitic CN, polyterthiophene)[350,379] and (ii) electrodes functionalized with redox-active molecular mediators (e.g., anthraquinones, flavins).[301,349] The coupling of such (photo)-electrocatalytic materials with r*Aae*UPO enabled hydroxylation of aliphatic and benzylic C(sp^3)-H bonds—with higher TTNs

https://doi.org/10.1021/acs.chemrev.5c01010
Chem. Rev. 2026, 126, 4857−4899

(>100,000) than photocatalytic systems—using solar and electrical energy.[301,349]

The dual light absorber tandem structure eliminates the need for external voltage to drive bias-free H_2O_2 generation and UPO catalysis. This economical approach can use abundant solar energy and H_2O as a sole driving force and electron donor, respectively, when it generates V_{ph} larger than the V_{th} for the H_2O oxidation-coupled O_2 reduction reaction (eq 28) and the required overpotentials.

$$2O_2 + 2H_2O \rightarrow 2H_2O_2 + O_2, \quad V_{th} = 0.55\ V \tag{28}$$

Choi et al. developed unassisted photobiocatalytic oxyfunctionalization by designing a photovoltaic-photoelectrocatalytic tandem architecture that consisted of a FeOOH-coated $BiVO_4$ photoanode, a $Cu(In,Ga)Se_2$ photovoltaic, and a graphitic CN/reduced graphene oxide hybrid cathode.[379] This device provided sufficient V_{ph} (~1.7 V) to oxidize H_2O and reduce O_2 under visible light (λ > 420 nm) without any electrical energy. However, the hybrid cathode further reduced H_2O_2 to $^{\bullet}OH$, which inactivated UPO within a few hours and consequently limited TTNs to ~43,000.

To further address the challenge of $^{\bullet}OH$-mediated UPO inactivation, the same group devised a Z-schematic tandem device that physically separated photoelectrocatalytic and biocatalytic sites (Figure 10c and Table 5).[350] This configuration was inspired by natural photosynthesis, where light and dark reactions occur in thylakoid membranes and stroma, respectively. In the artificial leaf system, a cellulose membrane was used to block the diffusion of short-lived $^{\bullet}OH$ and concurrently mediate H_2O_2 transport from polyterthiophene photoelectrocatalyst to r*Aae*UPO. This protection strategy extended the operational time of UPO biocatalysis by over 2-fold, increasing TTNs to ~128,000. These findings accentuate how spatial partitioning suppresses $^{\bullet}OH$-induced enzyme deactivation and allows effective mediator transfer for biosolar conversion.

The physical separation strategy also has been used with H_2O_2-generating photoelectrocatalytic systems for activating lignin peroxidase isozyme H8, which depolymerizes lignin to value-added aromatic compounds. Ko et al. developed a three-compartment enzymatic photoelectrocatalytic system to integrate unassisted solar-driven H_2O_2 generation with peroxidase-catalyzed lignin valorization (Table 5).[380] Nafion and cellulose membranes were used to isolate each reaction step—photoactivated TiO_2-driven H_2O oxidation, electrocatalytic O_2 reduction to H_2O_2, and H_2O_2-dependent biocatalytic lignin depolymerization—thereby preventing the deactivation of lignin peroxidase by reactive oxygen species (e.g., $^{\bullet}OH$, $O_2^{\bullet-}$) and O_2 bubbles. In addition, the spatial organization confined light exposure to the photoelectrocatalytic compartment, minimizing lignin's optical interference and light-induced enzyme deactivation. This compartmentalized system achieved lignin dimer depolymerization yield and selectivity of 93.7 and 98.7%, respectively, which were 2.6- and 2.9-fold improvements over noncompartmented system. These findings highlight that membrane-based compartmentalization prevents enzyme deactivation and substrate-induced light attenuation for the efficient depolymerization of complex biopolymers beyond simple organic molecules.

Besides the O_2 reduction-based photoelectrocatalytic systems, two-electron H_2O oxidation (eq 29) represents an alternative route for *in situ* H_2O_2 generation for H_2O_2-dependent biocatalysis.[59,381]

$$2H_2O \rightarrow H_2O_2 + 2H^+ + 2e^-, \quad E_{ox} = 1.76\ V\ vs\ RHE \tag{29}$$

This O_2-independent approach requires careful modulation of the photoanode's energetics to suppress the overoxidation of H_2O_2 to O_2. Photoanodic H_2O_2 production was achieved by positively shifting the E_F of a $BiVO_4$-based photoelectrocatalyst, thereby thermodynamically favoring two-electron H_2O oxidation (Table 5).[59] The anodically generated H_2O_2 drove UPO-mediated oxyfunctionalization, achieving TTNs of over 40,000. Unlike O_2-dependent systems, this anodic UPO biocatalysis was decoupled from the reduction of O_2 and instead paired with the reduction of N_2 to NH_3, enabling simultaneous fuel and chemical synthesis at both electrodes. This work illustrates the role of H_2O as a precursor for H_2O_2 supply in peroxygenase biocatalysis, eliminating the need for an O_2-reductive reaction.

6. CONCLUSIONS AND OUTLOOK

Recent cutting-edge advances in photocatalytic, photoelectrocatalytic, and photovoltaic-photoelectrocatalytic devices have established a coherent molecular toolkit for transducing solar photons into redox enzymes, metalloclusters, and whole-cell factories with turnover numbers exceeding 10^5 and solar-to-chemical efficiencies approaching the percent range. The convergence of materials science (e.g., molecular dyes, ordered redox-polymers, quantum dots, oxide semiconductors), device-level system engineering (e.g., multijunction photoabsorber stacks, waste-valorizing electrocatalysts), and enzymology (e.g., reductases, oxygenases, oxidases, dehydrogenases, metalloenzymes) provides a versatile design space for bias-free solar synthesis of fuels, fine chemicals, and polymer precursors. In the following subchapter, we discuss the research challenges and opportunities that must be addressed for biocatalytic artificial photosynthesis to evolve from proof-of-concept systems into scalable platforms.

6.1. Broad-Spectrum Solar Energy Capture and Efficient Charge Transfer

Solar-driven biocatalysis requires photo(electro)catalysts capable of harvesting the widest possible range of the solar spectrum and quickly transferring photogenerated charge carriers to oxidoreductases before charge recombination occurs. We propose that these goals can be achieved through two complementary approaches: (i) modulation of the absorber's electronic structure to expand the spectral response and (ii) acceleration of carrier extraction to minimize charge losses.

Deliberate tailoring of the band structure—often termed bandgap engineering—offers a rational means to utilize both high- and low-energy photons through bandgap narrowing or grading. Bandgap narrowing is typically achieved through substitutional doping or alloying. These processes introduce new electronic states that raise the VB or lower the CB.[382,383] In contrast, bandgap grading uses multilayer heterojunctions with descending bandgaps and carefully aligned band-edge energies.[384−386] In such architectures, the top layer absorbs high-energy photons, and the underlying layer absorbs red and near-infrared light, thereby increasing the cumulative V_{ph} beyond the threshold required for biocatalysis [e.g., 1.34 V (NADH-dependent FDH catalysis with H_2O oxidation),[61]

https://doi.org/10.1021/acs.chemrev.5c01010
Chem. Rev. 2026, 126, 4857−4899

0.55 V (H_2O_2-dependent UPO catalysis with H_2O oxidation)[350]].

Complementary to bandgap modulation, rapid carrier extraction represents another crucial frontier for the development of biosolar devices. Built-in electric fields generated by gradient doping or homojunctions[387,388] enhance the drift of photoexcited holes and electrons in opposite directions. In addition, carrier-selective contacts or heterojunction buffers offer another charge transport pathway. These interfaces transport target charge carriers to the material interface and block the opposite type of carriers, thereby minimizing interfacial recombination.[389] Further strategy is the introduction of redox-polymer interlayers[390−394] grafted at the electrode−electrolyte interface, enabling efficient charge extraction. Collectively, these interfacial and structural design principles will provide a roadmap toward photocatalysts that can efficiently couple solar energy with redox biocatalysts.

6.2. Tailoring Material-Enzyme Interface for Electron Transfer

Despite substantial strides in coupling semiconductor materials with redox enzymes, electron transfer across abiotic−biotic interfaces remains a major kinetic bottleneck. We envisage that transformative breakthroughs will arise from the convergence of thermodynamic alignment and molecular-level spatial control. Thermodynamic alignment between the material's quasi-Fermi levels and the redox potentials of biological components (e.g., coenzymes or prosthetic groups) is centrally important to provide a sufficient driving force for both direct and mediated electron transfer.

Once thermodynamic conditions are met, the design focus shifts based on the electron transfer mechanism. For DET, because efficient biological electron transfer typically occurs across distances of 4 to 14 Å,[395] achieving such nanoscale control will be instrumental in maximizing quantum tunneling efficiency and minimizing resistive losses at the interface. This requirement often necessitates site-specific immobilization strategies[396] to position enzymatic redox cofactors within the critical tunneling range of the conductive substrate. In addition, the interface should be precisely engineered to favor enzyme orientations. This enhances the interfacial electronic coupling between the material surface and the active site, which eliminates the cost and complexity of external components (e.g., mediators, coenzymes). Conversely, for mediated electron transfer, the priority shifts toward electrochemical kinetics and the concentration of redox shuttles at the catalyst surface to ensure a rapid charge diffusion.

In parallel, the adoption of hierarchically structured electrodes offers a significant advantage for both direct and mediated electron transfer pathways. Architectures integrating mesoporous films, inverse-opal frameworks, or nanopillar arrays embedded with conductive materials[397−400] can increase enzyme loading and effective surface area while maintaining efficient substrate transport. For DET, these multiscale structures are instrumental in establishing continuous electron-transport networks to maximize active tunneling sites, current density, and catalytic turnover. For mediated electron transfer, they provide a large reaction volume that mitigates diffusional bottlenecks and ensures a rapid interaction between mediators and biocatalysts.

Ultimately, distinguishing these design determinants clarifies which factors are critical for biosolar performance by contrasting the requirements of each mode. In mediated electron transfer, design efforts prioritize mediator solubility and long-range diffusion kinetics, while precise subnanometer alignment and protein orientation are relatively less important because diffusing mediators bridge the electronic gap. In contrast, for DET, these spatial parameters are the paramount factors that must be tailored, whereas mediator-related kinetics become secondary or less important in establishing a direct solid-state electronic connection.

6.3. Shielding Redox Biocatalysts from Abiotic Photodamage

Despite recent advances in integrating redox enzymes with photoactive materials, the long-term stability of these hybrid systems remains a critical issue. Abiotic photodamage—irreversible loss of catalytic activity of redox enzymes caused by the oxidative stress generated by abiotic photo(electro)catalysts—limits the operational lifetime of biosolar devices. Upon illumination, many photoactivated catalysts produce reactive oxygen species (e.g., $^{\bullet}OH$, $O_2^{\bullet-}$, $^1O_2$), which indiscriminately oxidize enzymes' active sites, cofactors, and structures.[401,402] Overcoming such degradation is essential for establishing robust solar-to-chemical conversion platforms.

We propose the use of antioxidant-rich scaffolds to mitigate oxidative damage[403] induced by reactive oxygen species. In this design, photo(electro)catalysts are interfaced with antioxidant molecular environments that dynamically scavenge reactive oxygen species at the abiotic−biotic interface. Antioxidant moieties, such as phenolic hydroxyl groups, thiols, and aromatic amines, engage in hydrogen atom or electron transfer, thereby quenching hydroxyl and superoxide radicals at the enzyme-material interface. Phenolic hydroxyl groups[314,404,405] yield resonance-stabilized phenoxy radicals upon hydrogen atom (or single-electron) donation; similarly, thiols[406−408] donate hydrogen atoms to reduce reactive oxygen species and then are oxidized to disulfides. Aromatic amine substituents[409,410] also participate in antioxidant reactions by lowering bond dissociation energies, thereby facilitating hydrogen-atom or electron transfer. In addition to the integrated material design, encapsulation of redox enzymes within sol−gel matrices may offer a means to enhance structural resilience by spatially confining protein molecules within rigid, nanoporous architectures.[411] This confinement helps preserve the enzyme's tertiary structure and protects buried residues from oxidative quenching.[412]

6.4. Enhancing Photo(electro)catalyst Stability in Biosolar Devices

Achieving long-term operational stability remains a formidable challenge in photobiocatalytic systems. Photo(electro)catalysts, although highly efficient in initial operation, are vulnerable to multiple intertwined degradation pathways, including charge accumulation and morphological deterioration. The uncontrolled buildup of charge carriers induces irreversible structural and compositional damage in photo(electro)catalysts.[53,350,413,414] For example, inefficient charge extraction allows photoexcited holes to oxidize lattice anions (e.g., O^{2-} in oxides), causing oxidative lattice degradation. In contrast, an accumulation of excess electrons reduces metal cations, which irreversibly alters the catalyst's stoichiometry and disrupts active sites. Consequently, charge accumulation leads to progressive disintegration of crystal frameworks and the loss of catalytic functionality.[415]

To mitigate the issue, future research needs to engineer the interfacial charge dynamics to accelerate carrier extraction and

https://doi.org/10.1021/acs.chemrev.5c01010
Chem. Rev. 2026, 126, 4857−4899

suppress self-degradation processes. Incorporating conductive interlayers or cocatalysts (e.g., Al_2O_3,[416,417] FeOOH,[59,61] $Ni(OH)_x$,[371,418] $[Cp^*Rh(bpy)Cl]^+$[419,420]) can achieve rapid carrier transfer to proximal biological components (e.g., $NAD(P)^+$, FMN, metal clusters, electron-relaying centers) and electron donors (e.g., H_2O, alcohols, lignin, microplastics). By minimizing the residence time of charge carriers within the semiconductor lattice, these hybrid interfaces can suppress self-oxidation and self-reduction events, thereby preserving photo-(electro)catalyst's composition and its long-term functionality.

In parallel, morphological stabilization is another task for the development of next-generation biosolar devices. Nanostructured photo(electro)catalysts, despite their favorable surface area and reactivity, are often susceptible to reshaping, fragmentation, and loss of crystallinity. Such degradation arises from surface dissolution, bond cleavage, structural reconstruction induced by reactive oxygen species and/or photoexcited charges.[421] Conformal surface coatings (e.g., silica,[422] Al_2O_3[423]) can suppress the degradation as (i) chemical passivation layer that isolates the catalyst lattice from corrosive intermediates and reactive radicals and (ii) physical diffusion barrier that blocks oxidative and reductive species.[424] Consequently, such protective layers preserve the crystalline integrity and mechanical cohesion of the underlying photocatalyst, thereby extending its operational lifetime without compromising its photoactivity.

6.5. Device-Level Development for Practical Biosolar Conversion

The transition from the proof-of-concept stage to practically viable solar-to-chemical conversion platforms depends on scalability. Large-area configurations are essential to realistically assess photon-to-chemical conversion efficiencies under natural solar light and to integrate upstream light-harvesting with downstream catalytic or biological processes. At present, prototype biosolar devices typically operate at the centimeter scale (about 1 cm^2 of geometrical surface area).[59,109,110,350] Progressing toward meter-scale operation will necessitate advanced processing strategies (e.g., screen printing,[425] spin coating,[426,427] precursor engineering[428]) to achieve structural uniformity and electronic continuity across large catalytic areas.[429,430]

In parallel with scaling abiotic components, the integration of biologicals with extended photoelectrode surfaces represents a defining challenge for biosolar device architectures. The development of large-area electrode platforms must therefore involve biointerface tailoring strategies[222,431−433] (e.g., covalent anchoring, redox-polymer wiring, and nanoporous or hierarchical scaffolds) to maintain enzyme orientation, activity, and electronic connectivity over macroscopic areas. Such an integrated architecture will be pivotal to translating the molecular precision of enzymatic catalysis into device-level functionality, ultimately bridging the gap between biological selectivity and technological scalability in next-generation biosolar systems.

The realization of practical biosolar conversion also demands a transition from static batch-type architectures toward dynamic and continuous operation modes. Most reported photobiocatalytic platforms operate in closed batch cells,[18,107,233,276,352,368,434] where limited mass transport, restricted photon penetration, and product accumulation[435,436] collectively constrain overall catalytic efficiency and stability. Implementing flow-cell architectures may overcome these limitations by enabling controlled reactant delivery, efficient product removal, and steady-state operation under continuous illumination—conditions essential for industrially relevant productivity and long-term enzyme functionality.[437]

Beyond improving biocatalytic single-step reactions, flow-based biosolar architectures offer a promising framework for multienzyme cascade catalysis,[438−446] in which reaction intermediates can be continuously transferred between spatially organized biocatalytic modules. Such modular configurations would enable the stepwise transformation of simple feedstocks into complex, value-added molecules (e.g., chiral fine chemicals, pharmaceutical precursors, and nutrient compounds). By combining solar energy capture with enzymatic selectivity in a continuous flow regime, these systems could bridge the gap between laboratory-scale prototypes and sustainable biosolar chemical manufacturing. In addition to constructive biosynthetic pathways, device-level photobiocatalytic systems hold significant potential for enabling degradation-driven multienzymatic cascade reactions. Building on the recent advances in multienzymatic cascade depolymerization of complex substrates,[447,448] the photo-(electro)catalytic-device-enabled regeneration of redox cofactors could be integrated with such depolymerization cascades to facilitate sequential bond cleavage and downstream upgrading under mild conditions.

To bridge laboratory-scale demonstrations and industrial implementation, solar-to-chemical biotransformation platforms should be assessed within a techno-economic analysis framework. The primary metric for assessing economic feasibility is the levelized cost of product, which relates discounted/annualized capital expenditures (e.g., light-harvesting components and device fabrication) and operating expenditures (e.g., biocatalyst replacement, utilities, and maintenance) to the annual product output.[449] From this perspective, competitiveness is governed by several device-level metrics (e.g., solar-to-chemical efficiency, operational stability, TTN, product concentration, and downstream processing) that directly control throughput and cost. First, the solar-to-chemical efficiency is a central driver of area-related costs. Efficiency values on the order of ∼10% are often cited as a useful benchmark for reducing land area and balance-of-system burdens.[450−452] Nevertheless, acceptable efficiency thresholds are application-specific and depend on selectivity/purity requirements and the cost intensity of downstream processing. Second, the operational stability remains a critical bottleneck. Commercial viability in many cases demands continuous operation for thousands of hours to achieve economically meaningful capital cost recovery and stable output. In biohybrid devices, cumulative productivity metrics such as enzyme TTN are therefore essential,[453,454] because they constrain replacement frequency and can strongly influence operating expenditures. Furthermore, product concentration and downstream processing can dominate the levelized cost of product.[308,455] Low product concentrations necessitate energy-intensive separation processes. To improve the overall economic outlook of biosolar conversion, device design should focus on maximizing product density and enabling *in situ* product recovery.

https://doi.org/10.1021/acs.chemrev.5c01010
Chem. Rev. 2026, 126, 4857−4899

AUTHOR INFORMATION

Corresponding Authors

Frank Hollmann − *Department of Biotechnology, Delft University of Technology, Delft 2629 HZ, The Netherlands;* orcid.org/0000-0003-4821-756X; Email: f.hollmann@tudelft.nl

Chan Beum Park − *Department of Materials Science and Engineering, Korea Advanced Institute of Science and Technology (KAIST), Daejeon 305-701, Republic of Korea;* orcid.org/0000-0002-0767-8629; Email: parkcb@kaist.ac.kr

Authors

Jinhyun Kim − *Department of Materials Science and Engineering, Ulsan National Institute of Science and Technology (UNIST), Ulsan 44919, Republic of Korea; Graduate School of Semiconductor Materials and Devices Engineering, Ulsan National Institute of Science and Technology (UNIST), Ulsan 44919, Republic of Korea;* orcid.org/0000-0002-1616-1891

Chang Hyun Kim − *Department of Materials Science and Engineering, Korea Advanced Institute of Science and Technology (KAIST), Daejeon 305-701, Republic of Korea;* orcid.org/0000-0003-2591-4426

Complete contact information is available at: https://pubs.acs.org/10.1021/acs.chemrev.5c01010

Author Contributions

#J.K. and C.H.K. contributed equally to this work. CRediT: **Jinhyun Kim** conceptualization, investigation, visualization, writing—original draft, writing—review and editing; **Chang Hyun Kim** conceptualization, investigation, visualization, writing—original draft, writing—review and editing; **Frank Hollmann** investigation, supervision, writing—review and editing; **Chan Beum Park** conceptualization, project administration, supervision, writing—review and editing.

Notes

The authors declare no competing financial interest.

Biographies

Jinhyun Kim is an Assistant Professor in Materials Science and Engineering at Ulsan National Institute of Science and Technology (UNIST). He received his B.S. in Chemistry from Gwangju Institute of Science and Technology (GIST) in 2016. He then earned his M.S. (2018) and Ph.D. (2022) in Materials Science and Engineering from Korea Advanced Institute of Science and Technology (KAIST) under the mentorship of Prof. Chan Beum Park. He conducted postdoctoral research at the University of California, Berkeley (UC Berkeley) from 2022 to 2024 in Chemical & Biomolecular Engineering and Chemistry under the mentorship of Professors Douglas S. Clark and Peidong Yang. His research focuses on integrating abiotic nanocatalysts with biological catalysts to enable waste valorization in photocatalytic, electrocatalytic, and photoelectrocatalytic systems.

Chang Hyun Kim received his B.S. in Materials Science and Engineering from Korea University in 2021 and his M.S. (2023) in Materials Science and Engineering from Korea Advanced Institute of Science and Technology (KAIST). He is currently pursuing a Ph.D. in Materials Science and Engineering at Korea Advanced Institute of Science and Technology (KAIST) under the mentorship of Prof. Chan Beum Park. His thesis study focuses on designing photo-(electro)catalytic materials and architectures for semiartificial photosynthetic processes.

Frank Hollmann studied Chemistry at the University of Bonn (Germany). After completing his Ph.D. at the Swiss Federal Institute of Technology in Zurich in 2004, he joined the Reetz group in Mülheim (Germany) as a postdoctoral fellow. Following several years as an R&D manager at Evonik Industries in Essen (Germany), he moved to Delft University of Technology (The Netherlands) in 2008 to join the Biocatalysis group. His research focuses on applying oxidoreductases for sustainable chemical synthesis.

Chan Beum Park received his B.S. (1991), M.S. (1995), and Ph.D. (1999) degrees in Chemical Engineering from POSTECH, then joined the Clark group at the University of California, Berkeley, as a postdoctoral researcher (1999−2002). He worked as an assistant professor at Arizona State University (2002−2006) before moving to KAIST. Since 2015, he serves as a director of the Creative Research Initiative (CRI) Center supported by the Korean Government. Dr. Park's research group focuses on coupling redox biocatalysis with abiotic catalysis (e.g., photocatalysis, electrocatalysis, piezocatalysis, thermocatalysis) toward the development of sustainable catalytic processes.

ACKNOWLEDGMENTS

This work was supported by the National Research Foundation of Korea (NRF) grants funded by the Ministry of Science and ICT (Grant No. RS-2024-00440681, RS-2024-00460425, RS-2025-00513045). F.H. acknowledges funding by the European Union (ERC, PeroxyZyme, No. 101054658). Views and opinions expressed are however those of the authors only and do not necessarily reflect those of the European Union or the European Research Council. Neither the European Union nor the granting authority can be held responsible for them.

ABBREVIATIONS

1,4-NADH	1,4-Dihydronicotinamide adenine dinucleotide
1,4-NADPH	Phosphorylated form of 1,4-dihydronicotinamide adenine dinucleotide
AM 1.5G	Air Mass 1.5 G
CB	Conduction band
*Cb*FDH	Formate dehydrogenase from *Candida boidinii*
CPO	Chloroperoxidase
CYP	Cytochrome P450s
DET	Direct electron transfer
E_{CB}	Conduction-band minimum
EDTA	Ethylenediaminetetraacetic acid
ee	Enantiomeric excess
E_F	Fermi level
E_g	Bandgap
E_{VB}	Valence-band maximum
FAD	Flavin adenine dinucleotide
FDH	Formate dehydrogenases
FE	Faradaic efficiency
FMN	Flavin mononucleotide
$FMNH_2$	Flavin mononucleotide hydroquinone
GDH	Glutamate dehydrogenase
H_2ase	Hydrogenases
HOMO	Highest occupied molecular orbital
LUMO	Lowest unoccupied molecular orbital
MMOH	Methane monooxygenase hydroxylase
M_{ox}	$[Cp^*Rh(III)(bpy)(H_2O)]^{2+}$
M_{red}	$[Cp^*Rh(III)(bpy)H]^{+}$

https://doi.org/10.1021/acs.chemrev.5c01010
Chem. Rev. 2026, 126, 4857−4899

MV^{2+}	Methyl viologen
$NAD(P)^+$	Nicotinamide adenine dinucleotide (phosphate)
NrfA	Cytochrome *c* nitrite reductase
*Nv*HFDH	[W]-Formate dehydrogenase from *Nitratidesulfovibrio vulgaris* Hildenborough
PET	Photoinduced electron transfer
RF	Riboflavin
r*Aae*UPO	Unspecific peroxygenase from *Agrocybe aegerita*, which was expressed recombinantly in *Pichia pastoris*
TEOA	Triethanolamine
TOF	Turnover frequency
*Ts*OYE	Old yellow enzyme homologue from *Thermus scotoductus* SA-01
TTN	Total turnover number
UPO	Unspecific peroxygenase
VB	Valence band
V_{ph}	Photovoltage
V_{th}	Thermodynamic voltage

REFERENCES

(1) Hanefeld, U.; Hollmann, F.; Paul, C. E. Biocatalysis making waves in organic chemistry. *Chem. Soc. Rev.* **2022**, *51* (2), 594−627.

(2) Dong, J.; Fernández-Fueyo, E.; Hollmann, F.; Paul, C. E.; Pesic, M.; Schmidt, S.; Wang, Y.; Younes, S.; Zhang, W. Biocatalytic Oxidation Reactions: A Chemist's Perspective. *Angew. Chem., Int. Ed.* **2018**, *57* (30), 9238−9261.

(3) Hollmann, F.; Opperman, D. J.; Paul, C. E. Biocatalytic Reduction Reactions from a Chemist's Perspective. *Angew. Chem., Int. Ed.* **2021**, *60* (11), 5644−5665.

(4) Litman, Z. C.; Wang, Y.; Zhao, H.; Hartwig, J. F. Cooperative asymmetric reactions combining photocatalysis and enzymatic catalysis. *Nature* **2018**, *560* (7718), 355−359.

(5) Han, X.; Chen, F.; Li, H.; Ge, R.; Shen, Q.; Duan, P.; Sheng, X.; Zhang, W. Reaction engineering blocks ether cleavage for synthesizing chiral cyclic hemiacetals catalyzed by unspecific peroxygenase. *Nat. Commun.* **2024**, *15* (1), 1235.

(6) Rehdorf, J.; Mihovilovic, M. D.; Bornscheuer, U. T. Exploiting the Regioselectivity of Baeyer-Villiger Monooxygenases for the Formation of β-Amino Acids and β-Amino Alcohols. *Angew. Chem., Int. Ed.* **2010**, *49* (26), 4506−4508.

(7) Lee, J.; Kim, S. M.; Jeon, B. W.; Hwang, H. W.; Poloniataki, E. G.; Kang, J.; Lee, S.; Ra, H. W.; Na, J.; Na, J.-G.; et al. Molar-scale formate production via enzymatic hydration of industrial off-gases. *Nat. Chem. Eng.* **2024**, *1* (5), 354−364.

(8) Jeon, B. W.; Phan, U. T.; Heo, Y.; Lee, H. H.; Ryu, J.; Kim, Y. H. Enzymatic conversion of CO_2 to formate: The potential of tungsten-containing formate dehydrogenase in flow reactor system. *J. CO2 Util.* **2024**, *82*, 102754.

(9) Moreno, D.; Omosebi, A.; Jeon, B. W.; Abad, K.; Kim, Y. H.; Thompson, J.; Liu, K. Decoupling Charge Carrier Electroreduction and Enzymatic CO_2 Conversion to Formate Using a Dual-Cell Flow Reactor System. *ACS Omega* **2024**, *9* (38), 39353−39364.

(10) Weliwatte, N. S.; Minteer, S. D. Photo-bioelectrocatalytic CO_2 reduction for a circular energy landscape. *Joule* **2021**, *5* (10), 2564−2592.

(11) Kim, S. M.; Kang, S. H.; Jeon, B. W.; Kim, Y. H. Tunnel engineering of gas-converting enzymes for inhibitor retardation and substrate acceleration. *Bioresour. Technol.* **2024**, *394*, 130248.

(12) Yoon, J.; Kim, J.; Tieves, F.; Zhang, W.; Alcalde, M.; Hollmann, F.; Park, C. B. Piezobiocatalysis: Ultrasound-Driven Enzymatic Oxyfunctionalization of C-H Bonds. *ACS Catal.* **2020**, *10* (9), 5236−5242.

(13) Yoon, J.; Jang, H.; Oh, M.-W.; Hilberath, T.; Hollmann, F.; Jung, Y. S.; Park, C. B. Heat-fueled enzymatic cascade for selective oxyfunctionalization of hydrocarbons. *Nat. Commun.* **2022**, *13* (1), 3741.

(14) Madjarov, J.; Soares, R.; Paquete, C. M.; Louro, R. O. *Sporomusa ovata* as Catalyst for Bioelectrochemical Carbon Dioxide Reduction: A Review Across Disciplines From Microbiology to Process Engineering. *Front. Microbiol.* **2022**, *13*, 913311.

(15) Chen, H.; Simoska, O.; Lim, K.; Grattieri, M.; Yuan, M.; Dong, F.; Lee, Y. S.; Beaver, K.; Weliwatte, S.; Gaffney, E. M.; et al. Fundamentals, Applications, and Future Directions of Bioelectrocatalysis. *Chem. Rev.* **2020**, *120* (23), 12903−12993.

(16) He, Y.; Wang, S.; Han, X.; Shen, J.; Lu, Y.; Zhao, J.; Shen, C.; Qiao, L. Photosynthesis of Acetate by *Sporomusa ovata*-CdS Biohybrid System. *ACS Appl. Mater. Interfaces* **2022**, *14* (20), 23364−23374.

(17) Zhang, L.; Beaton, S. E.; Carr, S. B.; Armstrong, F. A. Direct visible light activation of a surface cysteine-engineered [NiFe]-hydrogenase by silver nanoclusters. *Energy Environ. Sci.* **2018**, *11* (12), 3342−3348.

(18) Zhang, L.; Can, M.; Ragsdale, S. W.; Armstrong, F. A. Fast and Selective Photoreduction of CO_2 to CO Catalyzed by a Complex of Carbon Monoxide Dehydrogenase, TiO_2, and Ag Nanoclusters. *ACS Catal.* **2018**, *8* (4), 2789−2795.

(19) Siritanaratkul, B.; Islam, S. T. A.; Schubert, T.; Kunze, C.; Goris, T.; Diekert, G.; Armstrong, F. A. Selective, light-driven enzymatic dehalogenations of organic compounds. *RSC Adv.* **2016**, *6* (88), 84882−84886.

(20) Cobb, S. J.; Pornrungroj, C.; Andrei, V.; Badiani, V. M.; Su, L.; Manuel, R. R.; Pereira, I. A. C.; Reisner, E. A photoelectrochemical-thermoelectric device for semi-artificial CO_2 fixation employing full solar spectrum utilization. *Device* **2024**, *2* (11), 100505.

(21) Kornienko, N.; Zhang, J. Z.; Sakimoto, K. K.; Yang, P.; Reisner, E. Interfacing nature's catalytic machinery with synthetic materials for semi-artificial photosynthesis. *Nat. Nanotechnol.* **2018**, *13* (10), 890−899.

(22) Rahaman, M.; Pulignani, C.; Miller, M.; Bhattacharjee, S.; Bin Mohamad Annuar, A.; Manuel, R. R.; Pereira, I. A. C.; Reisner, E. Solar-Driven Paired CO_2 Reduction-Alcohol Oxidation Using Semi-artificial Suspension, Photocatalyst Sheet, and Photoelectrochemical Devices. *J. Am. Chem. Soc.* **2025**, *147* (10), 8168−8177.

(23) Tschörtner, J.; Lai, B.; Krömer, J. O. Biophotovoltaics: Green Power Generation From Sunlight and Water. *Front. Microbiol.* **2019**, *10*, 866.

(24) Rosenbaum, M.; He, Z.; Angenent, L. T. Light energy to bioelectricity: photosynthetic microbial fuel cells. *Curr. Opin. Biotechnol.* **2010**, *21* (3), 259−264.

(25) Megarity, C. F.; Esselborn, J.; Hexter, S. V.; Wittkamp, F.; Apfel, U.-P.; Happe, T.; Armstrong, F. A. Electrochemical Investigations of the Mechanism of Assembly of the Active-Site H-Cluster of [FeFe]-Hydrogenases. *J. Am. Chem. Soc.* **2016**, *138* (46), 15227−15233.

(26) Armstrong, F. A.; Evans, R. M.; Hexter, S. V.; Murphy, B. J.; Roessler, M. M.; Wulff, P. Guiding Principles of Hydrogenase Catalysis Instigated and Clarified by Protein Film Electrochemistry. *Acc. Chem. Res.* **2016**, *49* (5), 884−892.

(27) Evans, R. M.; Ash, P. A.; Beaton, S. E.; Brooke, E. J.; Vincent, K. A.; Carr, S. B.; Armstrong, F. A. Mechanistic Exploitation of a Self-Repairing, Blocked Proton Transfer Pathway in an O_2-Tolerant [NiFe]-Hydrogenase. *J. Am. Chem. Soc.* **2018**, *140* (32), 10208−10220.

(28) Evans, R. M.; Krahn, N.; Weiss, J.; Vincent, K. A.; Söll, D.; Armstrong, F. A. Replacing a Cysteine Ligand by Selenocysteine in a [NiFe]-Hydrogenase Unlocks Hydrogen Production Activity and Addresses the Role of Concerted Proton-Coupled Electron Transfer in Electrocatalytic Reversibility. *J. Am. Chem. Soc.* **2024**, *146* (25), 16971−16976.

(29) Evans, R. M.; Beaton, S. E.; Rodriguez Macia, P.; Pang, Y.; Wong, K. L.; Kertess, L.; Myers, W. K.; Bjornsson, R.; Ash, P. A.; Vincent, K. A.; et al. Comprehensive structural, infrared spectroscopic and kinetic investigations of the roles of the active-site arginine in bidirectional hydrogen activation by the [NiFe]-hydrogenase 'Hyd-2' from *Escherichia coli*. *Chem. Sci.* **2023**, *14* (32), 8531−8551.

https://doi.org/10.1021/acs.chemrev.5c01010
Chem. Rev. 2026, 126, 4857−4899

(30) Evans, R. M.; Krahn, N.; Murphy, B. J.; Lee, H.; Armstrong, F. A.; Söll, D. Selective cysteine-to-selenocysteine changes in a [NiFe]-hydrogenase confirm a special position for catalysis and oxygen tolerance. *Proc. Natl. Acad. Sci. U. S. A.* **2021**, *118* (13), No. e2100921118.
(31) Pandey, K.; Islam, S. T. A.; Happe, T.; Armstrong, F. A. Frequency and potential dependence of reversible electrocatalytic hydrogen interconversion by [FeFe]-hydrogenases. *Proc. Natl. Acad. Sci. U. S. A.* **2017**, *114* (15), 3843−3848.
(32) Ash, P. A.; Carr, S. B.; Reeve, H. A.; Skorupskaitė, A.; Rowbotham, J. S.; Shutt, R.; Frogley, M. D.; Evans, R. M.; Cinque, G.; Armstrong, F. A.; et al. Generating single metalloprotein crystals in well-defined redox states: electrochemical control combined with infrared imaging of a NiFe hydrogenase crystal. *Chem. Commun.* **2017**, *53* (43), 5858−5861.
(33) Brooke, E. J.; Evans, R. M.; Islam, S. T. A.; Roberts, G. M.; Wehlin, S. A. M.; Carr, S. B.; Phillips, S. E. V.; Armstrong, F. A. Importance of the Active Site "Canopy" Residues in an O_2-Tolerant [NiFe]-Hydrogenase. *Biochemistry* **2017**, *56* (1), 132−142.
(34) Wulff, P.; Thomas, C.; Sargent, F.; Armstrong, F. A. How the oxygen tolerance of a [NiFe]-hydrogenase depends on quaternary structure. *J. Biol. Inorg. Chem.* **2016**, *21* (1), 121−134.
(35) Kim, S. M.; Kang, S. H.; Lee, J.; Heo, Y.; Poloniataki, E. G.; Kang, J.; Yoon, H.-J.; Kong, S. Y.; Yun, Y.; Kim, H.; et al. Identifying a key spot for electron mediator-interaction to tailor CO dehydrogenase's affinity. *Nat. Commun.* **2024**, *15* (1), 2732.
(36) Moreno, D.; Omosebi, A.; Jeon, B. W.; Abad, K.; Kim, Y. H.; Thompson, J.; Liu, K. Electrochemical CO_2 conversion to formic acid using engineered enzymatic catalysts in a batch reactor. *J. CO2 Util.* **2023**, *70*, 102441.
(37) Proppe, A. H.; Li, Y. C.; Aspuru-Guzik, A.; Berlinguette, C. P.; Chang, C. J.; Cogdell, R.; Doyle, A. G.; Flick, J.; Gabor, N. M.; van Grondelle, R.; et al. Bioinspiration in light harvesting and catalysis. *Nat. Rev. Mater.* **2020**, *5* (11), 828−846.
(38) Yang, N.; Tian, Y.; Zhang, M.; Peng, X.; Li, F.; Li, J.; Li, Y.; Fan, B.; Wang, F.; Song, H. Photocatalyst-enzyme hybrid systems for light-driven biotransformation. *Biotechnol. Adv.* **2022**, *54*, 107808.
(39) Bissaro, B.; Forsberg, Z.; Ni, Y.; Hollmann, F.; Vaaje-Kolstad, G.; Eijsink, V. G. H. Fueling biomass-degrading oxidative enzymes by light-driven water oxidation. *Green Chem.* **2016**, *18* (19), 5357−5366.
(40) Linley, S.; Pornrungroj, C.; Reisner, E. Floating solar technologies for sustainable chemical synthesis on open water. *Nat. Chem. Eng.* **2026**, *3* (1), 34−46.
(41) Willkomm, J.; Orchard, K. L.; Reynal, A.; Pastor, E.; Durrant, J. R.; Reisner, E. Dye-sensitised semiconductors modified with molecular catalysts for light-driven H_2 production. *Chem. Soc. Rev.* **2016**, *45* (1), 9−23.
(42) Le, T.-K.; Kim, J.; Anh Nguyen, N.; Huong Ha Nguyen, T.; Sun, E.-G.; Yee, S.-M.; Kang, H.-S.; Yeom, S.-J.; Beum Park, C.; Yun, C.-H. Solar-Powered Whole-Cell P450 Catalytic Platform for C-Hydroxylation Reactions. *ChemSusChem* **2021**, *14* (15), 3054−3058.
(43) Romero, N. A.; Nicewicz, D. A. Organic Photoredox Catalysis. *Chem. Rev.* **2016**, *116* (17), 10075−10166.
(44) Kim, J.; Park, C. B. Shedding light on biocatalysis: photoelectrochemical platforms for solar-driven biotransformation. *Curr. Opin. Chem. Biol.* **2019**, *49*, 122−129.
(45) Andrei, V.; Ucoski, G. M.; Pornrungroj, C.; Uswachoke, C.; Wang, Q.; Achilleos, D. S.; Kasap, H.; Sokol, K. P.; Jagt, R. A.; Lu, H.; et al. Floating perovskite-$BiVO_4$ devices for scalable solar fuel production. *Nature* **2022**, *608* (7923), 518−522.
(46) Andrei, V.; Jagt, R. A.; Rahaman, M.; Lari, L.; Lazarov, V. K.; MacManus-Driscoll, J. L.; Hoye, R. L. Z.; Reisner, E. Long-term solar water and CO_2 splitting with photoelectrochemical BiOI-$BiVO_4$ tandems. *Nat. Mater.* **2022**, *21* (8), 864−868.
(47) Li, Z.; Luo, L.; Li, M.; Chen, W.; Liu, Y.; Yang, J.; Xu, S.-M.; Zhou, H.; Ma, L.; Xu, M.; et al. Photoelectrocatalytic C-H halogenation over an oxygen vacancy-rich TiO_2 photoanode. *Nat. Commun.* **2021**, *12* (1), 6698.
(48) Liang, K.; Yang, J.; Ye, M.; Zhang, Y.; Jang, Y. J.; Zhang, H. Hematite photoanode for efficient photoelectrochemical water splitting: recent advances and outlook. *Chem. Commun.* **2025**, *61* (43), 7724−7736.
(49) Kim, T. W.; Choi, K.-S. Nanoporous $BiVO_4$ Photoanodes with Dual-Layer Oxygen Evolution Catalysts for Solar Water Splitting. *Science* **2014**, *343* (6174), 990−994.
(50) Jiang, Y.; Tian, B. Inorganic semiconductor biointerfaces. *Nat. Rev. Mater.* **2018**, *3* (12), 473−490.
(51) Zhang, Z.; Yates, J. T., Jr. Band Bending in Semiconductors: Chemical and Physical Consequences at Surfaces and Interfaces. *Chem. Rev.* **2012**, *112* (10), 5520−5551.
(52) Kang, U.; Park, H. A facile synthesis of $CuFeO_2$ and CuO composite photocatalyst films for the production of liquid formate from CO_2 and water over a month. *J. Mater. Chem. A* **2017**, *5* (5), 2123−2131.
(53) Kuk, S. K.; Jang, J.; Kim, J.; Lee, Y.; Kim, Y. S.; Koo, B.; Lee, Y. W.; Ko, J. W.; Shin, B.; Lee, J.-K.; et al. CO_2-Reductive, Copper Oxide-Based Photobiocathode for Z-Scheme Semi-Artificial Leaf Structure. *ChemSusChem* **2020**, *13* (11), 2940−2944.
(54) Lee, C.-Y.; Park, H. S.; Fontecilla-Camps, J. C.; Reisner, E. Photoelectrochemical H_2 Evolution with a Hydrogenase Immobilized on a TiO_2-Protected Silicon Electrode. *Angew. Chem., Int. Ed.* **2016**, *55* (20), 5971−5974.
(55) Lineberry, E.; Kim, J.; Kim, J.; Roh, I.; Lin, J.-A.; Yang, P. High-Photovoltage Silicon Nanowire for Biological Cofactor Production. *J. Am. Chem. Soc.* **2023**, *145* (36), 19508−19512.
(56) Kim, J.; Lin, J.-A.; Kim, J.; Roh, I.; Lee, S.; Yang, P. A red-light-powered silicon nanowire biophotochemical diode for simultaneous CO_2 reduction and glycerol valorization. *Nat. Catal.* **2024**, *7* (9), 977−986.
(57) Bachmeier, A.; Hall, S.; Ragsdale, S. W.; Armstrong, F. A. Selective Visible-Light-Driven CO_2 Reduction on a p-Type Dye-Sensitized NiO Photocathode. *J. Am. Chem. Soc.* **2014**, *136* (39), 13518−13521.
(58) Chen, Z.; Huyền, N.; Miller, E.; Deutsch, T.; Domen, K.; Emery, K.; Forman, A.; Gaillard, N.; Garland, R.; Heske, C.; et al. *Photoelectrochemical Water Splitting: Standards, Experimental Methods, and Protocols*; Springer New York, 2013.
(59) Kim, C. H.; Kim, J.; Hollmann, F.; Park, C. B. Photoelectrocatalytic N_2 fixation and C-H oxyfunctionalization driven by H_2O oxidation. *Appl. Catal., B Environ.* **2023**, *336*, 122925.
(60) Wang, D.; Lee, S. H.; Han, S.; Kim, J.; Trang, N. V. T.; Kim, K.; Choi, E.-G.; Boonmongkolras, P.; Lee, Y. W.; Shin, B.; et al. Lignin-fueled photoelectrochemical platform for light-driven redox biotransformation. *Green Chem.* **2020**, *22* (15), 5151−5160.
(61) Kim, J.; Lee, Y. W.; Choi, E.-G.; Boonmongkolras, P.; Jeon, B. W.; Lee, H.; Kim, S. T.; Kuk, S. K.; Kim, Y. H.; Shin, B.; et al. Robust FeOOH/$BiVO_4$/Cu(In, Ga)Se_2 tandem structure for solar-powered biocatalytic CO_2 reduction. *J. Mater. Chem. A* **2020**, *8* (17), 8496−8502.
(62) Andrei, V.; Roh, I.; Lin, J.-A.; Lee, J.; Shan, Y.; Lin, C.-K.; Shelton, S.; Reisner, E.; Yang, P. Perovskite-driven solar C_2 hydrocarbon synthesis from CO_2. *Nat. Catal.* **2025**, *8* (2), 137−146.
(63) Andrei, V.; Chiang, Y.-H.; Rahaman, M.; Anaya, M.; Kang, T.; Ruggeri, E.; Stranks, S. D.; Reisner, E. Modular perovskite-$BiVO_4$ artificial leaves towards syngas synthesis on a m^2 scale. *Energy Environ. Sci.* **2025**, *18* (8), 3623−3632.
(64) Rahaman, M.; Andrei, V.; Pornrungroj, C.; Wright, D.; Baumberg, J. J.; Reisner, E. Selective CO production from aqueous CO_2 using a $Cu_{96}In_4$ catalyst and its integration into a bias-free solar perovskite-$BiVO_4$ tandem device. *Energy Environ. Sci.* **2020**, *13* (10), 3536−3543.
(65) Pornrungroj, C.; Andrei, V.; Rahaman, M.; Uswachoke, C.; Joyce, H. J.; Wright, D. S.; Reisner, E. Bifunctional Perovskite-$BiVO_4$ Tandem Devices for Uninterrupted Solar and Electrocatalytic Water Splitting Cycles. *Adv. Funct. Mater.* **2021**, *31* (15), 2008182.

https://doi.org/10.1021/acs.chemrev.5c01010
Chem. Rev. 2026, 126, 4857−4899

(66) Andrei, V.; Reuillard, B.; Reisner, E. Bias-free solar syngas production by integrating a molecular cobalt catalyst with perovskite-$BiVO_4$ tandems. *Nat. Mater.* **2020**, *19* (2), 189−194.
(67) Zhou, Y.; Herz, L. M.; Jen, A. K. Y.; Saliba, M. Advances and challenges in understanding the microscopic structure-property-performance relationship in perovskite solar cells. *Nat. Energy* **2022**, *7* (9), 794−807.
(68) Saga, T. Advances in crystalline silicon solar cell technology for industrial mass production. *NPG Asia Mater.* **2010**, *2* (3), 96−102.
(69) Kim, J.; Park, C. B. Artificial photosynthetic biohybrids for CO_2 and N_2 fixation. *Chem. Catal.* **2022**, *2* (10), 2425−2427.
(70) Moon, C.; Kim, C. H.; Min, J.; Koh, J.; Boonmongkolras, P.; Asare, G. K.; Hollmann, F.; Park, H. H.; Park, C. B.; Shin, B. Halide perovskite stabilized in a photoelectrochemical environment by impermeable single crystal TiO_2 for semi-artificial photosynthesis. *J. Mater. Chem. A* **2025**, *13* (47), 40908−40918.
(71) Noh, Y. I.; Kim, C. U.; Choi, K. J. Perovskite/homojunction-silicon tandem solar cells with optimized silicon nitride passivation and advanced double-sided ohmic contacts. *Mater. Today Energy* **2025**, *52*, 101917.
(72) Lee, M. H.; Kim, D. W.; Noh, Y. W.; Kim, H. S.; Han, J.; Lee, H.; Choi, K. J.; Cho, S.; Song, M. H. Controlled Crystal Growth of All-Inorganic CsPbI2Br via Sequential Vacuum Deposition for Efficient Perovskite Solar Cells. *ACS Nano* **2024**, *18* (27), 17764−17773.
(73) Lee, Y.; Kim, C. U.; Woo, Y.; Kim, W.-M.; Jeong, J.-h.; Kim, D.-h.; Lee, D.-K.; Choi, K. J.; Kim, I. Lithography-free fabrication of a local contact interlayer for Si-based tandem solar cells. *Prog. Photovolt.* **2024**, *32* (6), 406−416.
(74) Salimzhanov, B.; Kang, J. E.; Raju, N. A.; Kang, S. B.; Choi, K. J. Highly Stretchable Photovoltaic Module with Improved Mechanical Robustness through Elastomeric Interconnections. *Sol. RRL* **2024**, *8* (5), 2300973.
(75) Jeong, G.; Choi, Y.; Kim, Y.; Jung, S.; Koo, D.; Son, E.; Jeong, S.; Choi, K.-J.; Park, H. Stepwise Tailoring of Perovskite Nucleation Dynamics and Defect Formation Using a Supersaturation-Suppression Layer for Developing Efficient and Stable Perovskite Solar Cells. *Sol. RRL* **2024**, *8* (5), 2301025.
(76) Jung, E. D.; Kim, C. U.; Noh, Y. W.; Seo, S. K.; Noh, Y. I.; Choi, K. J.; Song, M. H. Aesthetic and efficient perovskite/Si tandem solar cells using luminescent down-shifting textured anti-reflection films. *EcoMat* **2023**, *5* (10), No. e12399.
(77) Koo, D.; Kim, U.; Cho, Y.; Lee, J.; Seo, J.; Choi, Y.; Choi, K. J.; Baik, J. M.; Yang, C.; Park, H. Graphene-Assisted Zwitterionic Conjugated Polycyclic Molecular Interfacial Layer Enables Highly Efficient and Stable Inverted Perovskite Solar Cells. *Chem. Mater.* **2021**, *33* (14), 5563−5571.
(78) Kim, C. U.; Jung, E. D.; Noh, Y. W.; Seo, S. K.; Choi, Y.; Park, H.; Song, M. H.; Choi, K. J. Strategy for large-scale monolithic Perovskite/Silicon tandem solar cell: A review of recent progress. *EcoMat* **2021**, *3* (2), No. e12084.
(79) Kang, S. B.; Park, W. J.; Jeong, M. H.; Kang, S.-H.; Yang, C.; Choi, K. J. Ambipolar Passivated Back Surface Field Layer for Silicon Photovoltaics. *Adv. Funct. Mater.* **2020**, *30* (50), 2004943.
(80) Choi, I. Y.; Kim, C. U.; Park, W.; Lee, H.; Song, M. H.; Hong, K. K.; Seok, S. I.; Choi, K. J. Two-terminal mechanical perovskite/silicon tandem solar cells with transparent conductive adhesives. *Nano Energy* **2019**, *65*, 104044.
(81) Kwon, J.; Im, M. J.; Kim, C. U.; Won, S. H.; Kang, S. B.; Kang, S. H.; Choi, I. T.; Kim, H. K.; Kim, I. H.; Park, J. H.; et al. Two-terminal DSSC/silicon tandem solar cells exceeding 18% efficiency. *Energy Environ. Sci.* **2016**, *9* (12), 3657−3665.
(82) Kim, C. U.; Yu, J. C.; Jung, E. D.; Choi, I. Y.; Park, W.; Lee, H.; Kim, I.; Lee, D.-K.; Hong, K. K.; Song, M. H.; et al. Optimization of device design for low cost and high efficiency planar monolithic perovskite/silicon tandem solar cells. *Nano Energy* **2019**, *60*, 213−221.
(83) Ha, J. M.; Kim, N.; Lee, D.; Lee, D. G.; Kim, H. Y.; Koh, C. W.; Kim, Y. I.; Park, S.; Lee, T. K.; Song, M. H.; et al. Multifunctional Conjugated Ligand with Intimate Binding Improves Luminescence, Charge Transport, and Stability in $CsPbBr_3$ Perovskite Nanocrystals. *Adv. Opt. Mater.* **2025**, *13* (31), No. e01640.
(84) Park, S.; Jeong, S. Y.; Kim, J.; Lee, H.; Kim, H. S.; Noh, Y. W.; Kim, Y. I.; Cho, S.; Kang, J. S.; Woo, H. Y.; et al. Synergistic enhancement of charge extraction and heat dissipation in inverted perovskite solar cells via n-doped top interlayers. *Energy Environ. Sci.* **2024**, *17* (21), 8304−8312.
(85) Kim, H. S.; Cho, Y.; Lee, H.; Kim, S.; Jung, E. D.; Noh, Y. W.; Park, S.; Cho, S.; Lee, B. R.; Yang, C.; et al. Vacuum-assisted reforming cathode interlayer orientation for efficient and stable perovskite solar cells. *Nano Energy* **2024**, *125*, 109584.
(86) Noh, Y. W.; Ha, J. M.; Son, J. G.; Han, J.; Lee, H.; Kim, D. W.; Jee, M. H.; Shin, W. G.; Cho, S.; Kim, J. Y.; et al. Improved photovoltaic performance and stability of perovskite solar cells by adoption of an n-type zwitterionic cathode interlayer. *Mater. Horiz.* **2024**, *11* (12), 2926−2936.
(87) Park, J. H.; Noh, Y. W.; Ha, J. M.; Harit, A. K.; Tripathi, A.; Lee, J.; Lee, B. R.; Song, M. H.; Woo, H. Y. Anionic Conjugated Polyelectrolyte as a Semiconducting Additive for Efficient and Stable Perovskite Solar Cells. *ACS Appl. Mater. Interfaces* **2024**, *16* (16), 19937−19946.
(88) Kim, D. W.; Noh, Y. W.; Han, J.; Kim, H. S.; Jang, C. H.; Hong, J. A.; Park, S.; Lee, M. H.; Kim, Y. I.; Song, M. H. Efficient $MAPbI_3$-based perovskite solar cells exceeding 21% efficiency via aging treatment. *Chem. Eng. J.* **2023**, *475*, 146451.
(89) Hong, J. A.; Jeong, M.; Park, S.; Lee, A.-Y.; Kim, H. S.; Jeong, S.; Kim, D. W.; Cho, S.; Yang, C.; Song, M. H. Efficient and Moisture-Stable Inverted Perovskite Solar Cells via n-Type Small-Molecule-Assisted Surface Treatment. *Adv. Sci.* **2023**, *10* (3), 2205127.
(90) Bae, S.; Noh, Y. W.; Park, D.-S.; Song, M. H.; Choi, S.-W. Development of colored perovskite solar cells using cholesteric helicoidal superstructures. *Nano Energy* **2022**, *93*, 106801.
(91) Harit, A. K.; Jung, E. D.; Ha, J. M.; Park, J. H.; Tripathi, A.; Noh, Y. W.; Song, M. H.; Woo, H. Y. Triphenylamine-Based Conjugated Polyelectrolyte as a Hole Transport Layer for Efficient and Scalable Perovskite Solar Cells. *Small* **2022**, *18* (5), 2104933.
(92) Jung, E. D.; Harit, A. K.; Kim, D. H.; Jang, C. H.; Park, J. H.; Cho, S.; Song, M. H.; Woo, H. Y. Multiply Charged Conjugated Polyelectrolytes as a Multifunctional Interlayer for Efficient and Scalable Perovskite Solar Cells. *Adv. Mater.* **2020**, *32* (30), 2002333.
(93) Hong, J. A.; Jung, E. D.; Yu, J. C.; Kim, D. W.; Nam, Y. S.; Oh, I.; Lee, E.; Yoo, J.-W.; Cho, S.; Song, M. H. Improved Efficiency of Perovskite Solar Cells Using a Nitrogen-Doped Graphene-Oxide-Treated Tin Oxide Layer. *ACS Appl. Mater. Interfaces* **2020**, *12* (2), 2417−2423.
(94) Lee, S.; Jang, C. H.; Nguyen, T. L.; Kim, S. H.; Lee, K. M.; Chang, K.; Choi, S. S.; Kwak, S. K.; Woo, H. Y.; Song, M. H. Conjugated Polyelectrolytes as Multifunctional Passivating and Hole-Transporting Layers for Efficient Perovskite Light-Emitting Diodes. *Adv. Mater.* **2019**, *31* (24), 1900067.
(95) Yu, J. C.; Badgujar, S.; Jung, E. D.; Singh, V. K.; Kim, D. W.; Gierschner, J.; Lee, E.; Kim, Y. S.; Cho, S.; Kwon, M. S.; et al. Highly Efficient and Stable Inverted Perovskite Solar Cell Obtained via Treatment by Semiconducting Chemical Additive. *Adv. Mater.* **2019**, *31* (6), 1805554.
(96) Kang, S. B.; Jeong, M. H.; Choi, I. Y.; Sohn, S.-D.; Kim, S. H.; Shin, H.-J.; Park, W. I.; Shin, J. C.; Song, M. H.; Choi, K. J. Self-assembled, highly crystalline porous ferroelectric poly(vinylidene fluoride-co-trifluoroethylene) interlayer for Si/organic hybrid solar cells. *Nano Energy* **2017**, *41*, 243−250.
(97) Andrei, V.; Wang, Q.; Uekert, T.; Bhattacharjee, S.; Reisner, E. Solar Panel Technologies for Light-to-Chemical Conversion. *Acc. Chem. Res.* **2022**, *55* (23), 3376−3386.
(98) Kim, S.; Kim, K. H.; Oh, C.; Zhang, K.; Park, J. H. Artificial photosynthesis for high-value-added chemicals: Old material, new opportunity. *Carbon Energy* **2022**, *4* (1), 21−44.

https://doi.org/10.1021/acs.chemrev.5c01010
Chem. Rev. 2026, 126, 4857−4899

(99) Lv, J.; Xie, J.; Mohamed, A. G. A.; Zhang, X.; Feng, Y.; Jiao, L.; Zhou, E.; Yuan, D.; Wang, Y. Solar utilization beyond photosynthesis. *Nat. Rev. Chem.* **2023**, *7* (2), 91−105.
(100) Fang, X.; Kalathil, S.; Reisner, E. Semi-biological approaches to solar-to-chemical conversion. *Chem. Soc. Rev.* **2020**, *49* (14), 4926−4952.
(101) Blankenship, R. E.; Tiede, D. M.; Barber, J.; Brudvig, G. W.; Fleming, G.; Ghirardi, M.; Gunner, M. R.; Junge, W.; Kramer, D. M.; Melis, A.; et al. Comparing Photosynthetic and Photovoltaic Efficiencies and Recognizing the Potential for Improvement. *Science* **2011**, *332* (6031), 805−809.
(102) Croce, R.; Carmo-Silva, E.; Cho, Y. B.; Ermakova, M.; Harbinson, J.; Lawson, T.; McCormick, A. J.; Niyogi, K. K.; Ort, D. R.; Patel-Tupper, D.; et al. Perspectives on improving photosynthesis to increase crop yield. *Plant Cell* **2024**, *36* (10), 3944−3973.
(103) Batista-Silva, W.; da Fonseca-Pereira, P.; Martins, A. O.; Zsögön, A.; Nunes-Nesi, A.; Araújo, W. L. Engineering Improved Photosynthesis in the Era of Synthetic Biology. *Plant Commun.* **2020**, *1* (2), 100032.
(104) Liu, C.; Colón, B. C.; Ziesack, M.; Silver, P. A.; Nocera, D. G. Water splitting-biosynthetic system with CO_2 reduction efficiencies exceeding photosynthesis. *Science* **2016**, *352* (6290), 1210−1213.
(105) Su, Y.; Cestellos-Blanco, S.; Kim, J. M.; Shen, Y.-x.; Kong, Q.; Lu, D.; Liu, C.; Zhang, H.; Cao, Y.; Yang, P. Close-Packed Nanowire-Bacteria Hybrids for Efficient Solar-Driven CO_2 Fixation. *Joule* **2020**, *4* (4), 800−811.
(106) Liu, C.; Gallagher, J. J.; Sakimoto, K. K.; Nichols, E. M.; Chang, C. J.; Chang, M. C. Y.; Yang, P. Nanowire-Bacteria Hybrids for Unassisted Solar Carbon Dioxide Fixation to Value-Added Chemicals. *Nano Lett.* **2015**, *15* (5), 3634−3639.
(107) Edwardes Moore, E.; Andrei, V.; Oliveira, A. R.; Coito, A. M.; Pereira, I. A. C.; Reisner, E. A Semi-artificial Photoelectrochemical Tandem Leaf with a CO_2-to-Formate Efficiency Approaching 1%. *Angew. Chem., Int. Ed.* **2021**, *60* (50), 26303−26307.
(108) Kuk, S. K.; Ham, Y.; Gopinath, K.; Boonmongkolras, P.; Lee, Y.; Lee, Y. W.; Kondaveeti, S.; Ahn, C.; Shin, B.; Lee, J.-K.; et al. Continuous 3D Titanium Nitride Nanoshell Structure for Solar-Driven Unbiased Biocatalytic CO_2 Reduction. *Adv. Energy Mater.* **2019**, *9* (25), 1900029.
(109) Edwardes Moore, E.; Andrei, V.; Zacarias, S.; Pereira, I. A. C.; Reisner, E. Integration of a Hydrogenase in a Lead Halide Perovskite Photoelectrode for Tandem Solar Water Splitting. *ACS Energy Lett.* **2020**, *5* (1), 232−237.
(110) Sokol, K. P.; Robinson, W. E.; Warnan, J.; Kornienko, N.; Nowaczyk, M. M.; Ruff, A.; Zhang, J. Z.; Reisner, E. Bias-free photoelectrochemical water splitting with photosystem II on a dye-sensitized photoanode wired to hydrogenase. *Nat. Energy* **2018**, *3* (11), 944−951.
(111) Guo, J.; Suástegui, M.; Sakimoto, K. K.; Moody, V. M.; Xiao, G.; Nocera, D. G.; Joshi, N. S. Light-driven fine chemical production in yeast biohybrids. *Science* **2018**, *362* (6416), 813−816.
(112) Kumar, M.; Meena, B.; Subramanyam, P.; Suryakala, D.; Subrahmanyam, C. Recent trends in photoelectrochemical water splitting: the role of cocatalysts. *NPG Asia Mater.* **2022**, *14* (1), 88.
(113) Harris-Lee, T. R.; Marken, F.; Bentley, C. L.; Zhang, J.; Johnson, A. L. A chemist's guide to photoelectrode development for water splitting - the importance of molecular precursor design. *EES Catal.* **2023**, *1* (6), 832−873.
(114) Zhang, L.; Wang, Y. Decoupled Artificial Photosynthesis. *Angew. Chem., Int. Ed.* **2023**, *62* (23), No. e202219076.
(115) Pawar, A. U.; Kim, C. W.; Nguyen-Le, M.-T.; Kang, Y. S. General Review on the Components and Parameters of Photoelectrochemical System for CO_2 Reduction with in Situ Analysis. *ACS Sustain. Chem. Eng.* **2019**, *7* (8), 7431−7455.
(116) Kozuch, S.; Martin, J. M. L. "Turning Over" Definitions in Catalytic Cycles. *ACS Catal.* **2012**, *2* (12), 2787−2794.
(117) Lagerman, C. E.; Blum, J. K.; Rogers, T. A.; Grover, M. A.; Rousseau, R. W.; Bommarius, A. S. Total turnover number prediction of an aggregating biocatalyst: Amino ester hydrolase (AEH). *Chem. Eng. Sci.* **2023**, *277*, 118804.
(118) Rogers, T. A.; Bommarius, A. S. Utilizing simple biochemical measurements to predict lifetime output of biocatalysts in continuous isothermal processes. *Chem. Eng. Sci.* **2010**, *65* (6), 2118−2124.
(119) Roskoski, R. Michaelis-Menten Kinetics. In *Reference Module in Biomedical Sciences*; Elsevier, 2015.
(120) Bligaard, T.; Bullock, R. M.; Campbell, C. T.; Chen, J. G.; Gates, B. C.; Gorte, R. J.; Jones, C. W.; Jones, W. D.; Kitchin, J. R.; Scott, S. L. Toward Benchmarking in Catalysis Science: Best Practices, Challenges, and Opportunities. *ACS Catal.* **2016**, *6* (4), 2590−2602.
(121) Faber, K. *Biotransformations in Organic Chemistry: A Textbook*; Springer Cham, 2018.
(122) Fard, P. T.; Albert, S. K.; Ko, J.; Lee, S.; Park, S.-J.; Kim, J. Spatial Organization of Photocatalysts and Enzymes on Janus-Type DNA Nanosheets for Efficient CO_2 Conversion. *ACS Catal.* **2022**, *12* (15), 9698−9705.
(123) Ji, X.; Su, Z.; Wang, P.; Ma, G.; Zhang, S. Integration of Artificial Photosynthesis System for Enhanced Electronic Energy-Transfer Efficacy: A Case Study for Solar-Energy Driven Bioconversion of Carbon Dioxide to Methanol. *Small* **2016**, *12* (34), 4753−4762.
(124) Noji, T.; Jin, T.; Nango, M.; Kamiya, N.; Amao, Y. CO_2 Photoreduction by Formate Dehydrogenase and a Ru-Complex in a Nanoporous Glass Reactor. *ACS Appl. Mater. Interfaces* **2017**, *9* (4), 3260−3265.
(125) Kim, S.; Lee, S.; Anjong, T. F.; Jang, H. Y.; Kim, J.-Y.; Lee, C.; Park, S.; Lee, H. J.; Yoon, J.; Kim, J. Artificial Photocatalytic System Using Polydiacetylene-(-NH-phen)$Ru(bpy)_2$ for Cofactor Regeneration and CO_2 Reduction. *J. Phys. Chem. C* **2016**, *120* (50), 28407−28414.
(126) Ikeyama, S.; Amao, Y. A novel electron carrier molecule based on a viologen derivative for visible light-driven CO_2 reduction to formic acid with the system of zinc porphyrin and formate dehydrogenase. *Sustain. Energy Fuels* **2017**, *1* (8), 1730−1733.
(127) Lee, S. H.; Kwon, Y.-C.; Kim, D.-M.; Park, C. B. Cytochrome P450-catalyzed O-dealkylation coupled with photochemical NADPH regeneration. *Biotechnol. Bioeng.* **2013**, *110* (2), 383−390.
(128) Lee, S. H.; Lee, H. J.; Won, K.; Park, C. B. Artificial Electron Carriers for Photoenzymatic Synthesis under Visible Light. *Chem.—Eur. J.* **2012**, *18* (18), 5490−5495.
(129) Nam, D. H.; Park, C. B. Visible Light-Driven NADH Regeneration Sensitized by Proflavine for Biocatalysis. *ChemBioChem.* **2012**, *13* (9), 1278−1282.
(130) Biegasiewicz, K. F.; Cooper, S. J.; Emmanuel, M. A.; Miller, D. C.; Hyster, T. K. Catalytic promiscuity enabled by photoredox catalysis in nicotinamide-dependent oxidoreductases. *Nat. Chem.* **2018**, *10* (7), 770−775.
(131) Lee, S. H.; Nam, D. H.; Kim, J. H.; Baeg, J.-O.; Park, C. B. Eosin Y-Sensitized Artificial Photosynthesis by Highly Efficient Visible-Light-Driven Regeneration of Nicotinamide Cofactor. *ChemBioChem.* **2009**, *10* (10), 1621−1624.
(132) Lee, S. H.; Nam, D. H.; Park, C. B. Screening Xanthene Dyes for Visible Light-Driven Nicotinamide Adenine Dinucleotide Regeneration and Photoenzymatic Synthesis. *Adv. Synth. Catal.* **2009**, *351* (16), 2589−2594.
(133) Jang, J.; Das, D.; Lestari, R.; Lee, J.-K.; Park, C. B. Solar-hybrid biocatalyst for methane hydroxylation to methanol. *Nat. Commun.* **2025**, *16* (1), 9310.
(134) Yu, S.; Zhang, S.; Li, K.; Yang, Q.; Wang, M.; Cai, D.; Tan, T.; Chen, B. Furfuryl Alcohol Production with High Selectivity by a Novel Visible-Light Driven Biocatalysis Process. *ACS Sustain. Chem. Eng.* **2020**, *8* (42), 15980−15988.
(135) Tan, Y.; Ma, J.; Zhang, F.; Wang, S.; Lan, F.; Liu, H.; Li, R. Polymer Photocatalyst-Enzyme Coupled Artificial Photosynthesis System for CO_2 Reduction into Formate Using Water as the Electron Donor. *ACS Sustain. Chem. Eng.* **2022**, *10* (37), 12065−12071.

https://doi.org/10.1021/acs.chemrev.5c01010
Chem. Rev. 2026, 126, 4857−4899

(136) Zhang, N.; Trépout, S.; Chen, H.; Li, M.-H. AIE Polymer Micelle/Vesicle Photocatalysts Combined with Native Enzymes for Aerobic Photobiocatalysis. *J. Am. Chem. Soc.* **2023**, *145* (1), 288−299.
(137) Burai, T. N.; Panay, A. J.; Zhu, H.; Lian, T.; Lutz, S. Light-Driven, Quantum Dot-Mediated Regeneration of FMN To Drive Reduction of Ketoisophorone by Old Yellow Enzyme. *ACS Catal.* **2012**, *2* (4), 667−670.
(138) Honda, Y.; Hagiwara, H.; Ida, S.; Ishihara, T. Application to Photocatalytic H_2 Production of a Whole-Cell Reaction by Recombinant *Escherichia coli* Cells Expressing [FeFe]-Hydrogenase and Maturases Genes. *Angew. Chem., Int. Ed.* **2016**, *55* (28), 8045−8048.
(139) Wei, P.; Dong, J.; Gao, X.; Chang, L.; Huang, Z.; Zheng, H.; Lee, S. M.-Y.; Lou, W.-Y.; Peng, C. Efficient NADH Regeneration without Electron Mediator toward Enzymatic CO_2 Reduction Enabled by a Lawn-like TP-COFs/$Ti_3C_2T_x$ (MXene) Photocatalyst. *ACS Sustain. Chem. Eng.* **2024**, *12* (18), 6881−6893.
(140) Wei, P.; Zhang, Y.; Dong, J.; Cao, Y.; Lee, S. M.-Y.; Lou, W.; Peng, C. Engineering MXene-based photocatalyst for efficient NADH regeneration and photoenzymatic CO_2 reduction without electron mediator. *Appl. Catal., B Environ.* **2024**, *357*, 124257.
(141) Yadav, D.; Kumar, A.; Kim, J. Y.; Park, N.-J.; Baeg, J.-O. Interfacially synthesized 2D COF thin film photocatalyst: efficient photocatalyst for solar formic acid production from CO_2 and fine chemical synthesis. *J. Mater. Chem. A* **2021**, *9* (15), 9573−9580.
(142) Zhao, H.; Huang, F.; Liu, G.; Liu, Y.; Wang, Y.; Liu, X.; Xing, C.; Gao, J.; Yue, X.; Jiang, Y. Rh-Functionalized Donor-π-Acceptor Covalent Organic Framework for Efficient Photocatalytic Nicotinamide Cofactor Regeneration. *ACS Sustain. Chem. Eng.* **2024**, *12* (34), 12775−12785.
(143) Qu, J.; Yang, T.; Zhang, P.; Yang, F.; Cai, Y.; Yang, X.; Li, C. M.; Hu, J. Artificial photosynthesis platform of 2D/2D MXene/crystalline covalent organic frameworks heterostructure for efficient photoenzymatic CO_2 reduction. *Appl. Catal., B Environ.* **2024**, *348*, 123827.
(144) Zhao, Y.; Liu, H.; Wu, C.; Zhang, Z.; Pan, Q.; Hu, F.; Wang, R.; Li, P.; Huang, X.; Li, Z. Fully Conjugated Two-Dimensional sp^2-Carbon Covalent Organic Frameworks as Artificial Photosystem I with High Efficiency. *Angew. Chem., Int. Ed.* **2019**, *58* (16), 5376−5381.
(145) Lin, G.; Zhang, Y.; Hua, Y.; Zhang, C.; Jia, C.; Ju, D.; Yu, C.; Li, P.; Liu, J. Bioinspired Metalation of the Metal-Organic Framework MIL-125-NH_2 for Photocatalytic NADH Regeneration and Gas-Liquid-Solid Three-Phase Enzymatic CO_2 Reduction. *Angew. Chem., Int. Ed.* **2022**, *61* (31), No. e202206283.
(146) Zhang, S.; Shi, J.; Sun, Y.; Wu, Y.; Zhang, Y.; Cai, Z.; Chen, Y.; You, C.; Han, P.; Jiang, Z. Artificial Thylakoid for the Coordinated Photoenzymatic Reduction of Carbon Dioxide. *ACS Catal.* **2019**, *9* (5), 3913−3925.
(147) Zhang, Y.; Liu, J. Bioinspired Photocatalytic NADH Regeneration by Covalently Metalated Carbon Nitride for Enhanced CO_2 Reduction. *Chem.—Eur. J.* **2022**, *28* (55), No. e202201430.
(148) Yadav, R. K.; Kumar, A.; Yadav, D.; Park, N.-J.; Kim, J. Y.; Baeg, J.-O. In Situ Prepared Flexible 3D Polymer Film Photocatalyst for Highly Selective Solar Fuel Production from CO_2. *ChemCatChem.* **2018**, *10* (9), 2024−2029.
(149) Zhao, Z.; Zheng, D.; Guo, M.; Yu, J.; Zhang, S.; Zhang, Z.; Chen, Y. Engineering Olefin-Linked Covalent Organic Frameworks for Photoenzymatic Reduction of CO_2. *Angew. Chem., Int. Ed.* **2022**, *61* (12), No. e202200261.
(150) Singh, N.; Yadav, D.; Mulay, S. V.; Kim, J. Y.; Park, N.-J.; Baeg, J.-O. Band Gap Engineering in Solvochromic 2D Covalent Organic Framework Photocatalysts for Visible Light-Driven Enhanced Solar Fuel Production from Carbon Dioxide. *ACS Appl. Mater. Interfaces* **2021**, *13* (12), 14122−14131.
(151) Meng, J.; Tian, Y.; Li, C.; Lin, X.; Wang, Z.; Sun, L.; Zhou, Y.; Li, J.; Yang, N.; Zong, Y.; et al. A thiophene-modified doubleshell hollow g-C_3N_4 nanosphere boosts NADH regeneration via synergistic enhancement of charge excitation and separation. *Catal. Sci. Technol.* **2019**, *9* (8), 1911−1921.
(152) Zhao, H.; Qi, Y.; Zhan, P.; Zhu, Q.; Liu, X.; Guan, X.; Zhang, C.; Su, C.; Qin, P.; Cai, D. Artificial Photoenzymatic Reduction of Carbon Dioxide to Methanol by Using Electron Mediator and Co-factorAssembled $ZnIn_2S_4$ Nanoflowers. *ChemSusChem* **2023**, *16* (12), No. e202300061.
(153) Gu, X.; Huang, T.; Hong, Y.; Wu, Y.; Wang, Z.; Zhang, Y.; Liu, S.; Han, J. Boosting the photocatalytic CO_2 conversion efficiency of MOFs using a solid electron conveyor. *J. Mater. Chem. A* **2023**, *11* (18), 9784−9790.
(154) Yadav, R. K.; Kumar, A.; Park, N.-J.; Kong, K.-J.; Baeg, J.-O. A highly efficient covalent organic framework film photocatalyst for selective solar fuel production from CO_2. *J. Mater. Chem. A* **2016**, *4* (24), 9413−9418.
(155) Wang, Y.; Gong, M.; Wang, H.; Xiao, G.; Su, H.; Xing, J. Photocatalytic CO_2 Fixation into Formate under Visible Light by the Photo-Enzyme Hybrid of Gold Nanocapsules and Formate Dehydrogenase. *Photocatal. Res. Potential* **2024**, *1*, 10011−10011.
(156) Ryu, J.; Lee, S. H.; Nam, D. H.; Park, C. B. Rational Design and Engineering of Quantum-Dot-Sensitized TiO_2 Nanotube Arrays for Artificial Photosynthesis. *Adv. Mater.* **2011**, *23* (16), 1883−1888.
(157) Gunner, M. R.; Madeo, J.; Zhu, Z. Modification of quinone electrochemistry by the proteins in the biological electron transfer chains: examples from photosynthetic reaction centers. *J. Bioenerg. Biomembr.* **2008**, *40* (5), 509−519.
(158) Zhang, X.; Wu, J.; Wang, J.; He, H.; Liu, A.; Hong, X.; Yu, Y.; Pei, X.; Fang, X.; Xin, Y.; et al. Structural basis of menaquinone reduction by succinate dehydrogenase from *Chloroflexus aurantiacus*. *Nat. Commun.* **2025**, *16* (1), 10782.
(159) Buckel, W.; Thauer, R. K. Flavin-Based Electron Bifurcation, Ferredoxin, Flavodoxin, and Anaerobic Respiration With Protons (Ech) or NAD^+ (Rnf) as Electron Acceptors: A Historical Review. *Front. Microbiol.* **2018**, *9*, 401.
(160) Ko, J. W.; Choi, W. S.; Kim, J.; Kuk, S. K.; Lee, S. H.; Park, C. B. Self-Assembled Peptide-Carbon Nitride Hydrogel as a Light-Responsive Scaffold Material. *Biomacromolecules* **2017**, *18* (11), 3551−3556.
(161) Wang, D.; Kim, J.; Park, C. B. Lignin-Induced $CaCO_3$ Vaterite Structure for Biocatalytic Artificial Photosynthesis. *ACS Appl. Mater. Interfaces* **2021**, *13* (49), 58522−58531.
(162) Wang, Y.; Jin, Y.; Wang, Z.; Xiao, G.; Su, H. A Light-Dark Cascade Procedure for the Regeneration of NADH using Graphitic Carbon Nitride Nanosheets. *ChemPhotoChem* **2022**, *6* (8), No. e202200067.
(163) Liu, W.; Hu, W.; Yang, L.; Liu, J. Single cobalt atom anchored on carbon nitride with well-defined active sites for photo-enzyme catalysis. *Nano Energy* **2020**, *73*, 104750.
(164) Kim, J.; Lee, S. H.; Tieves, F.; Choi, D. S.; Hollmann, F.; Paul, C. E.; Park, C. B. Biocatalytic C═C Bond Reduction through Carbon Nanodot-Sensitized Regeneration of NADH Analogues. *Angew. Chem., Int. Ed.* **2018**, *57* (42), 13825−13828.
(165) Ji, X.; Kang, Y.; Fan, T.; Xiong, Q.; Zhang, S.; Tao, W.; Zhang, H. An antimonene/Cp*Rh(phen)Cl/black phosphorus hybrid nanosheet-based Z-scheme artificial photosynthesis for enhanced photo/bio-catalytic CO_2 reduction. *J. Mater. Chem. A* **2020**, *8* (1), 323−333.
(166) Höfler, G. T.; Fernández-Fueyo, E.; Pesic, M.; Younes, S. H.; Choi, E.-G.; Kim, Y. H.; Urlacher, V. B.; Arends, I. W. C. E.; Hollmann, F. A Photoenzymatic NADH Regeneration System. *ChemBioChem.* **2018**, *19* (22), 2344−2347.
(167) Lee, J. S.; Nam, D. H.; Kuk, S. K.; Park, C. B. Near-Infrared-Light-Driven Artificial Photosynthesis by Nanobiocatalytic Assemblies. *Chem.—Eur. J.* **2014**, *20* (13), 3584−3588.
(168) Kim, J. H.; Lee, M.; Lee, J. S.; Park, C. B. Self-Assembled Light-Harvesting Peptide Nanotubes for Mimicking Natural Photosynthesis. *Angew. Chem., Int. Ed.* **2012**, *51* (2), 517−520.
(169) Kim, J. H.; Lee, S. H.; Lee, J. S.; Lee, M.; Park, C. B. Zn-containing porphyrin as a biomimetic light-harvesting molecule for

https://doi.org/10.1021/acs.chemrev.5c01010
Chem. Rev. 2026, 126, 4857−4899

biocatalyzed artificial photosynthesis. *Chem. Commun.* **2011**, *47* (37), 10227−10229.
(170) Lee, J. S.; Lee, S. H.; Kim, J. H.; Park, C. B. Artificial photosynthesis on a chip: microfluidic cofactor regeneration and photoenzymatic synthesis under visible light. *Lab Chip* **2011**, *11* (14), 2309−2311.
(171) Lee, M.; Kim, J. H.; Lee, S. H.; Lee, S. H.; Park, C. B. Biomimetic Artificial Photosynthesis by Light-Harvesting Synthetic Wood. *ChemSusChem* **2011**, *4* (5), 581−586.
(172) Lee, S. H.; Ryu, J.; Nam, D. H.; Park, C. B. Photoenzymatic synthesis through sustainable NADH regeneration by SiO_2-supported quantum dots. *Chem. Commun.* **2011**, *47* (16), 4643−4645.
(173) Nam, D. H.; Lee, S. H.; Park, C. B. CdTe, CdSe, and CdS Nanocrystals for Highly Efficient Regeneration of Nicotinamide Cofactor Under Visible Light. *Small* **2010**, *6* (8), 922−926.
(174) Aamer, E.; Thöming, J.; Baune, M.; Reimer, N.; Dringen, R.; Romero, M.; Bösing, I. Influence of electrode potential, pH and NAD^+ concentration on the electrochemical NADH regeneration. *Sci. Rep.* **2022**, *12* (1), 16380.
(175) Sharma, V. K.; Hutchison, J. M.; Allgeier, A. M. Redox Biocatalysis: Quantitative Comparisons of Nicotinamide Cofactor Regeneration Methods. *ChemSusChem* **2022**, *15* (22), No. e202200888.
(176) Burnett, J. W. H.; Chen, H.; Li, J.; Li, Y.; Huang, S.; Shi, J.; McCue, A. J.; Howe, R. F.; Minteer, S. D.; Wang, X. Supported Pt Enabled Proton-Driven $NAD(P)^+$ Regeneration for Biocatalytic Oxidation. *ACS Appl. Mater. Interfaces* **2022**, *14* (18), 20943−20952.
(177) Jayasinghe, L.; Wei, J.; Kim, J.; Lineberry, E.; Yang, P. Particle on a Rod: Surface-Tethered Catalyst on CdS Nanorods for Enzymatically Active Nicotinamide Cofactor Generation. *Nano Lett.* **2024**, *24* (42), 13269−13276.
(178) Chen, Y.; Li, P.; Zhou, J.; Buru, C. T.; Đorđević, L.; Li, P.; Zhang, X.; Cetin, M. M.; Stoddart, J. F.; Stupp, S. I.; et al. Integration of Enzymes and Photosensitizers in a Hierarchical Mesoporous Metal-Organic Framework for Light-Driven CO_2 Reduction. *J. Am. Chem. Soc.* **2020**, *142* (4), 1768−1773.
(179) Chakraborty, I. N.; Jain, V.; Roy, P.; Kumar, P.; Vinod, C. P.; Pillai, P. P. Photocatalytic Regeneration of Reactive Cofactors with InP Quantum Dots for the Continuous Chemical Synthesis. *ACS Catal.* **2024**, *14* (9), 6740−6748.
(180) Sun, Y.; Shi, J.; Wang, Z.; Wang, H.; Zhang, S.; Wu, Y.; Wang, H.; Li, S.; Jiang, Z. Thylakoid Membrane-Inspired Capsules with Fortified Cofactor Shuttling for Enzyme-Photocoupled Catalysis. *J. Am. Chem. Soc.* **2022**, *144* (9), 4168−4177.
(181) Bouwens, T.; Cobb, S. J.; Yeung, C. W. S.; Liu, Y.; Martins, G.; Pereira, I. A. C.; Reisner, E. Semiartificial Photoelectrochemistry for CO_2-Mediated Enantioselective Organic Synthesis. *J. Am. Chem. Soc.* **2025**, *147* (16), 13114−13119.
(182) Ryu, J.; Nam, D. H.; Lee, S. H.; Park, C. B. Biocatalytic Photosynthesis with Water as an Electron Donor. *Chem.—Eur. J.* **2014**, *20* (38), 12020−12025.
(183) Luo, F.; Gu, X.; Zhu, Y.; Zhou, J.; Xu, G.; Ni, Y. Photocatalytic regeneration of nicotinamide cofactor biomimetics drives biocatalytic reduction by Old Yellow enzymes. *Bioorg. Chem.* **2024**, *147*, 107418.
(184) Megarity, C. F.; Herold, R. A.; Armstrong, F. A. Extending protein-film electrochemistry across enzymology and biological inorganic chemistry to investigate, track and control the reactions of non-redox enzymes and spectroscopically silent metals. *J. Biol. Inorg. Chem.* **2025**, *30* (3), 209−219.
(185) Herold, R. A.; Schofield, C. J.; Armstrong, F. A. Building Localized NADP(H) Recycling Circuits to Advance Enzyme Cascadetronics. *Angew. Chem., Int. Ed.* **2025**, *64* (10), No. e202414176.
(186) Siritanaratkul, B.; Megarity, C. F.; Herold, R. A.; Armstrong, F. A. Interactive biocatalysis achieved by driving enzyme cascades inside a porous conducting material. *Commun. Chem.* **2024**, *7* (1), 132.
(187) Herold, R. A.; Schofield, C. J.; Armstrong, F. A. Electrochemical Nanoreactor Provides a Comprehensive View of Isocitrate Dehydrogenase Cancer-drug Kinetics. *Angew. Chem., Int. Ed.* **2023**, *62* (42), No. e202309149.
(188) Morello, G.; Megarity, C. F.; Armstrong, F. A. The power of electrified nanoconfinement for energising, controlling and observing long enzyme cascades. *Nat. Commun.* **2021**, *12* (1), 340.
(189) Morello, G.; Siritanaratkul, B.; Megarity, C. F.; Armstrong, F. A. Efficient Electrocatalytic CO_2 Fixation by Nanoconfined Enzymes via a C3-to-C4 Reaction That Is Favored over H_2 Production. *ACS Catal.* **2019**, *9* (12), 11255−11262.
(190) Wan, L.; Heath, R. S.; Siritanaratkul, B.; Megarity, C. F.; Sills, A. J.; Thompson, M. P.; Turner, N. J.; Armstrong, F. A. Enzyme-catalysed enantioselective oxidation of alcohols by air exploiting fast electrochemical nicotinamide cycling in electrode nanopores. *Green Chem.* **2019**, *21* (18), 4958−4963.
(191) Megarity, C. F.; Siritanaratkul, B.; Heath, R. S.; Wan, L.; Morello, G.; FitzPatrick, S. R.; Booth, R. L.; Sills, A. J.; Robertson, A. W.; Warner, J. H.; et al. Electrocatalytic Volleyball: Rapid Nanoconfined Nicotinamide Cycling for Organic Synthesis in Electrode Pores. *Angew. Chem., Int. Ed.* **2019**, *58* (15), 4948−4952.
(192) Evans, R. M.; Siritanaratkul, B.; Megarity, C. F.; Pandey, K.; Esterle, T. F.; Badiani, S.; Armstrong, F. A. The value of enzymes in solar fuels research - efficient electrocatalysts through evolution. *Chem. Soc. Rev.* **2019**, *48* (7), 2039−2052.
(193) Wan, L.; Megarity, C. F.; Siritanaratkul, B.; Armstrong, F. A. A hydrogen fuel cell for rapid, enzyme-catalysed organic synthesis with continuous monitoring. *Chem. Commun.* **2018**, *54* (8), 972−975.
(194) Siritanaratkul, B.; Megarity, C. F.; Roberts, T. G.; Samuels, T. O. M.; Winkler, M.; Warner, J. H.; Happe, T.; Armstrong, F. A. Transfer of photosynthetic $NADP^+$/NADPH recycling activity to a porous metal oxide for highly specific, electrochemically-driven organic synthesis. *Chem. Sci.* **2017**, *8* (6), 4579−4586.
(195) Batie, C. J.; Kamin, H. Association of ferredoxin-$NADP^+$ reductase with NADP(H) specificity and oxidation-reduction properties. *J. Biol. Chem.* **1986**, *261* (24), 11214−11223.
(196) Brown, K. A.; Wilker, M. B.; Boehm, M.; Hamby, H.; Dukovic, G.; King, P. W. Photocatalytic Regeneration of Nicotinamide Cofactors by Quantum Dot-Enzyme Biohybrid Complexes. *ACS Catal.* **2016**, *6* (4), 2201−2204.
(197) Jones, J. B.; Taylor, K. E. Use of pyridinium and flavin derivatives for recycling of catalystic amounts of NAD^+ during preparative-scale horse liver alchohol dehydrogenase-catalysed oxidations of alcohols. *J. Chem. Soc., Chem. Commun.* **1973**, No. 6, 205−206.
(198) Gargiulo, S.; Arends, I. W. C. E.; Hollmann, F. A Photoenzymatic System for Alcohol Oxidation. *ChemCatChem.* **2011**, *3* (2), 338−342.
(199) Rauch, M.; Schmidt, S.; Arends, I. W. C. E.; Oppelt, K.; Kara, S.; Hollmann, F. Photobiocatalytic alcohol oxidation using LED light sources. *Green Chem.* **2017**, *19* (2), 376−379.
(200) Son, G.; Kim, J.; Park, C. B. Interference of Solvatochromic Twist in Amyloid Nanostructure for Light-Driven Biocatalysis. *ACS Appl. Energy Mater.* **2020**, *3* (1), 1215−1221.
(201) Su, D.; Kabir, M. P.; Orozco-Gonzalez, Y.; Gozem, S.; Gadda, G. Fluorescence Properties of Flavin Semiquinone Radicals in Nitronate Monooxygenase. *ChemBioChem.* **2019**, *20* (13), 1646−1652.
(202) Beaupre, B. A.; Moran, G. R. N5 Is the New C4a: Biochemical Functionalization of Reduced Flavins at the N5 Position. *Front. Mol. Biosci.* **2020**, *7*, 598912.
(203) Vogt, S.; Schneider, M.; Schäfer-Eberwein, H.; Nöll, G. Determination of the pH Dependent Redox Potential of Glucose Oxidase by Spectroelectrochemistry. *Anal. Chem.* **2014**, *86* (15), 7530−7535.
(204) Nguyen, H. D.; Renslow, R.; Babauta, J.; Ahmed, B.; Beyenal, H. A voltammetric flavin microelectrode for use in biofilms. *Sens. Actuators B: Chem.* **2012**, *161* (1), 929−937.

https://doi.org/10.1021/acs.chemrev.5c01010
Chem. Rev. 2026, 126, 4857−4899

(205) Gonçalves, L. C. P.; Mansouri, H. R.; Bastos, E. L.; Abdellah, M.; Fadiga, B. S.; Sá, J.; Rudroff, F.; Mihovilovic, M. D. Morpholine-based buffers activate aerobic photobiocatalysis via spin correlated ion pair formation. *Catal. Sci. Technol.* **2019**, *9* (6), 1365−1371.
(206) Rudroff, F.; Mihovilovic, M. D.; Gröger, H.; Snajdrova, R.; Iding, H.; Bornscheuer, U. T. Opportunities and challenges for combining chemo- and biocatalysis. *Nat. Catal.* **2018**, *1* (1), 12−22.
(207) Hollmann, F.; Taglieber, A.; Schulz, F.; Reetz, M. T. A Light-Driven Stereoselective Biocatalytic Oxidation. *Angew. Chem., Int. Ed.* **2007**, *46* (16), 2903−2906.
(208) van Schie, M. M. C. H.; Paul, C. E.; Arends, I. W. C. E.; Hollmann, F. Photoenzymatic epoxidation of styrenes. *Chem. Commun.* **2019**, *55* (12), 1790−1792.
(209) Schroeder, L.; Frese, M.; Müller, C.; Sewald, N.; Kottke, T. Photochemically Driven Biocatalysis of Halogenases for the Green Production of Chlorinated Compounds. *ChemCatChem.* **2018**, *10* (15), 3336−3341.
(210) Taglieber, A.; Schulz, F.; Hollmann, F.; Rusek, M.; Reetz, M. T. Light-Driven Biocatalytic Oxidation and Reduction Reactions: Scope and Limitations. *ChemBioChem.* **2008**, *9* (4), 565−572.
(211) Grau, M. M.; van der Toorn, J. C.; Otten, L. G.; Macheroux, P.; Taglieber, A.; Zilly, F. E.; Arends, I. W. C. E.; Hollmann, F. Photoenzymatic Reduction of C═C Double Bonds. *Adv. Synth. Catal.* **2009**, *351* (18), 3279−3286.
(212) Churakova, E.; Kluge, M.; Ullrich, R.; Arends, I.; Hofrichter, M.; Hollmann, F. Specific Photobiocatalytic Oxyfunctionalization Reactions. *Angew. Chem., Int. Ed.* **2011**, *50* (45), 10716−10719.
(213) Mifsud, M.; Gargiulo, S.; Iborra, S.; Arends, I. W. C. E.; Hollmann, F.; Corma, A. Photobiocatalytic chemistry of oxidoreductases using water as the electron donor. *Nat. Commun.* **2014**, *5* (1), 3145.
(214) Rowe, S. F.; Le Gall, G.; Ainsworth, E. V.; Davies, J. A.; Lockwood, C. W. J.; Shi, L.; Elliston, A.; Roberts, I. N.; Waldron, K. W.; Richardson, D. J.; et al. Light-Driven H_2 Evolution and C═C or C═O Bond Hydrogenation by *Shewanella oneidensis*: A Versatile Strategy for Photocatalysis by Nonphotosynthetic Microorganisms. *ACS Catal.* **2017**, *7* (11), 7558−7566.
(215) Cheng, F.; Pavliuk, O.; Hardt, S.; Hunt, L. A.; Cai, B.; Kubart, T.; Hammarström, L.; Plumeré, N.; Berggren, G.; Tian, H. Embedding biocatalysts in a redox polymer enhances the performance of dye-sensitized photocathodes in bias-free photoelectrochemical water splitting. *Nat. Commun.* **2024**, *15* (1), 3202.
(216) Pavliuk, M. V.; Lorenzi, M.; Morado, D. R.; Gedda, L.; Wrede, S.; Mejias, S. H.; Liu, A.; Senger, M.; Glover, S.; Edwards, K.; et al. Polymer Dots as Photoactive Membrane Vesicles for [FeFe]-Hydrogenase Self-Assembly and Solar-Driven Hydrogen Evolution. *J. Am. Chem. Soc.* **2022**, *144* (30), 13600−13611.
(217) Macpherson, S.; Lawson, T.; Abfalterer, A.; Andrich, P.; Lage, A.; Reisner, E.; Euser, T. G.; Stranks, S. D.; Gentleman, A. S. Influence of Electron Donors on the Charge Transfer Dynamics of Carbon Nanodots in Photocatalytic Systems. *ACS Catal.* **2024**, *14* (16), 12006−12015.
(218) Badalyan, A.; Yang, Z.-Y.; Hu, M.; Liu, T. L.; Seefeldt, L. C. Tailoring electron transfer pathway for photocatalytic N_2-to-NH_3 reduction in a CdS quantum dots-nitrogenase system. *Sustain. Energy Fuels* **2022**, *6* (9), 2256−2263.
(219) Chen, H.; Cai, R.; Patel, J.; Dong, F.; Chen, H.; Minteer, S. D. Upgraded Bioelectrocatalytic N_2 Fixation: From N_2 to Chiral Amine Intermediates. *J. Am. Chem. Soc.* **2019**, *141* (12), 4963−4971.
(220) Chen, H.; Prater, M. B.; Cai, R.; Dong, F.; Chen, H.; Minteer, S. D. Bioelectrocatalytic Conversion from N_2 to Chiral Amino Acids in a H_2/α-Keto Acid Enzymatic Fuel Cell. *J. Am. Chem. Soc.* **2020**, *142* (8), 4028−4036.
(221) Wang, B.; Zhang, Y.; Minteer, S. D. Renewable electron-driven bioinorganic nitrogen fixation: a superior route toward green ammonia? *Energy Environ. Sci.* **2023**, *16* (2), 404−420.
(222) Dong, F.; Lee, Y. S.; Gaffney, E. M.; Liou, W.; Minteer, S. D. Engineering Cyanobacterium with Transmembrane Electron Transfer Ability for Bioelectrochemical Nitrogen Fixation. *ACS Catal.* **2021**, *11* (21), 13169−13179.
(223) Fussell, K. C.; Udasin, R. G.; Gray, J. P.; Mishin, V.; Smith, P. J. S.; Heck, D. E.; Laskin, J. D. Redox cycling and increased oxygen utilization contribute to diquat-induced oxidative stress and cytotoxicity in Chinese hamster ovary cells overexpressing NADPH-cytochrome P450 reductase. *Free Radic. Biol. Med.* **2011**, *50* (7), 874−882.
(224) Koomson, D. A.; Nicholson, J. H.; Brogan, A. P. S.; Aldous, L. Re-assessing viologens for modern bio-electrocatalysis. *Chem. Sci.* **2024**, *15* (24), 9325−9332.
(225) Peers, M. K.; Toogood, H. S.; Heyes, D. J.; Mansell, D.; Coe, B. J.; Scrutton, N. S. Light-driven biocatalytic reduction of α,β-unsaturated compounds by ene reductases employing transition metal complexes as photosensitizers. *Catal. Sci. Technol.* **2016**, *6* (1), 169−177.
(226) Jones, R. W.; Garland, P. B. Sites and specificity of the reaction of bipyridylium compounds with anaerobic respiratory enzymes of *Escherichia coli*. Effects of permeability barriers imposed by the cytoplasmic membrane. *Biochem. J.* **1977**, *164* (1), 199−211.
(227) Liu, Y.; Rodríguez-Jiménez, S.; Song, H.; Pannwitz, A.; Kim, D.; Coito, A. M.; Manuel, R. R.; Webb, S.; Su, L.; Bonke, S. A.; et al. Bio-Inspired Self-Assembly of Enzyme-Micelle Systems for Semi-Artificial Photosynthesis. *Angew. Chem., Int. Ed.* **2025**, *64* (18), No. e202424222.
(228) Liu, Y.; Pulignani, C.; Webb, S.; Cobb, S. J.; Rodríguez-Jiménez, S.; Kim, D.; Milton, R. D.; Reisner, E. Electrostatic [FeFe]-hydrogenase-carbon nitride assemblies for efficient solar hydrogen production. *Chem. Sci.* **2024**, *15* (16), 6088−6094.
(229) Jang, J.; Lestari, R.; Jo, Y.; Lee, J.-K.; Park, C. B. Photobiocatalytic methane hydroxylation driven by organosilica nanodots. *Appl. Catal., B Environ.* **2025**, *365*, 124999.
(230) Chaudhary, Y. S.; Woolerton, T. W.; Allen, C. S.; Warner, J. H.; Pierce, E.; Ragsdale, S. W.; Armstrong, F. A. Visible light-driven CO_2 reduction by enzyme coupled CdS nanocrystals. *Chem. Commun.* **2012**, *48* (1), 58−60.
(231) Woolerton, T. W.; Sheard, S.; Chaudhary, Y. S.; Armstrong, F. A. Enzymes and bio-inspired electrocatalysts in solar fuel devices. *Energy Environ. Sci.* **2012**, *5* (6), 7470−7490.
(232) Woolerton, T. W.; Sheard, S.; Pierce, E.; Ragsdale, S. W.; Armstrong, F. A. CO_2 photoreduction at enzyme-modified metal oxide nanoparticles. *Energy Environ. Sci.* **2011**, *4* (7), 2393−2399.
(233) Woolerton, T. W.; Sheard, S.; Reisner, E.; Pierce, E.; Ragsdale, S. W.; Armstrong, F. A. Efficient and Clean Photoreduction of CO_2 to CO by Enzyme-Modified TiO_2 Nanoparticles Using Visible Light. *J. Am. Chem. Soc.* **2010**, *132* (7), 2132−2133.
(234) Wang, Q.; Kalathil, S.; Pornrungroj, C.; Sahm, C. D.; Reisner, E. Bacteria-photocatalyst sheet for sustainable carbon dioxide utilization. *Nat. Catal.* **2022**, *5* (7), 633−641.
(235) Wang, B.; Jiang, Z.; Yu, J. C.; Wang, J.; Wong, P. K. Enhanced CO_2 reduction and valuable C_{2+} chemical production by a CdS-photosynthetic hybrid system. *Nanoscale* **2019**, *11* (19), 9296−9301.
(236) Reisner, E.; Powell, D. J.; Cavazza, C.; Fontecilla-Camps, J. C.; Armstrong, F. A. Visible Light-Driven H_2 Production by Hydrogenases Attached to Dye-Sensitized TiO_2 Nanoparticles. *J. Am. Chem. Soc.* **2009**, *131* (51), 18457−18466.
(237) Zhang, L.; Morello, G.; Carr, S. B.; Armstrong, F. A. Aerobic Photocatalytic H_2 Production by a [NiFe] Hydrogenase Engineered to Place a Silver Nanocluster in the Electron Relay. *J. Am. Chem. Soc.* **2020**, *142* (29), 12699−12707.
(238) Lam, E.; Miller, M.; Linley, S.; Manuel, R. R.; Pereira, I. A. C.; Reisner, E. Comproportionation of CO_2 and Cellulose to Formate Using a Floating Semiconductor-Enzyme Photoreforming Catalyst. *Angew. Chem., Int. Ed.* **2023**, *62* (20), No. e202215894.
(239) Hamby, H.; Li, B.; Shinopoulos, K. E.; Keller, H. R.; Elliott, S. J.; Dukovic, G. Light-driven carbon-carbon bond formation via CO_2 reduction catalyzed by complexes of CdS nanorods and a 2-oxoacid oxidoreductase. *Proc. Natl. Acad. Sci. U. S. A.* **2020**, *117* (1), 135−140.

https://doi.org/10.1021/acs.chemrev.5c01010
Chem. Rev. 2026, 126, 4857−4899

(240) Brown, K. A.; Harris, D. F.; Wilker, M. B.; Rasmussen, A.; Khadka, N.; Hamby, H.; Keable, S.; Dukovic, G.; Peters, J. W.; Seefeldt, L. C.; et al. Light-driven dinitrogen reduction catalyzed by a CdS:nitrogenase MoFe protein biohybrid. *Science* **2016**, *352* (6284), 448−450.
(241) Zhang, H.; Jaenecke, J.; Bishara-Robertson, I. L.; Casadevall, C.; Redman, H. J.; Winkler, M.; Berggren, G.; Plumeré, N.; Butt, J. N.; Reisner, E.; et al. Semiartificial Photosynthetic Nanoreactors for H_2 Generation. *J. Am. Chem. Soc.* **2024**, *146* (50), 34260−34264.
(242) Cobb, S. J.; Rodríguez-Jiménez, S.; Reisner, E. Connecting Biological and Synthetic Approaches for Electrocatalytic CO_2 Reduction. *Angew. Chem., Int. Ed.* **2024**, *63* (8), No. e202310547.
(243) Cobb, S. J.; Dharani, A. M.; Oliveira, A. R.; Pereira, I. A. C.; Reisner, E. Carboxysome-Inspired Electrocatalysis using Enzymes for the Reduction of CO_2 at Low Concentrations. *Angew. Chem., Int. Ed.* **2023**, *62* (26), No. e202218782.
(244) Cobb, S. J.; Badiani, V. M.; Dharani, A. M.; Wagner, A.; Zacarias, S.; Oliveira, A. R.; Pereira, I. A. C.; Reisner, E. Fast CO_2 hydration kinetics impair heterogeneous but improve enzymatic CO_2 reduction catalysis. *Nat. Chem.* **2022**, *14* (4), 417−424.
(245) Edwardes Moore, E.; Cobb, S. J.; Coito, A. M.; Oliveira, A. R.; Pereira, I. A. C.; Reisner, E. Understanding the local chemical environment of bioelectrocatalysis. *Proc. Natl. Acad. Sci. U. S. A.* **2022**, *119* (4), No. e2114097119.
(246) Badiani, V. M.; Cobb, S. J.; Wagner, A.; Oliveira, A. R.; Zacarias, S.; Pereira, I. A. C.; Reisner, E. Elucidating Film Loss and the Role of Hydrogen Bonding of Adsorbed Redox Enzymes by Electrochemical Quartz Crystal Microbalance Analysis. *ACS Catal.* **2022**, *12* (3), 1886−1897.
(247) Sokol, K. P.; Robinson, W. E.; Oliveira, A. R.; Zacarias, S.; Lee, C.-Y.; Madden, C.; Bassegoda, A.; Hirst, J.; Pereira, I. A. C.; Reisner, E. Reversible and Selective Interconversion of Hydrogen and Carbon Dioxide into Formate by a Semiartificial Formate Hydrogenlyase Mimic. *J. Am. Chem. Soc.* **2019**, *141* (44), 17498−17502.
(248) Kornienko, N.; Ly, K. H.; Robinson, W. E.; Heidary, N.; Zhang, J. Z.; Reisner, E. Advancing Techniques for Investigating the Enzyme-Electrode Interface. *Acc. Chem. Res.* **2019**, *52* (5), 1439−1448.
(249) Robinson, W. E.; Bassegoda, A.; Reisner, E.; Hirst, J. Oxidation-State-Dependent Binding Properties of the Active Site in a Mo-Containing Formate Dehydrogenase. *J. Am. Chem. Soc.* **2017**, *139* (29), 9927−9936.
(250) Wombwell, C.; Caputo, C. A.; Reisner, E. [NiFeSe]-Hydrogenase Chemistry. *Acc. Chem. Res.* **2015**, *48* (11), 2858−2865.
(251) Wombwell, C.; Reisner, E. Synthetic Active Site Model of the [NiFeSe] Hydrogenase. *Chem.—Eur. J.* **2015**, *21* (22), 8096−8104.
(252) Bassegoda, A.; Madden, C.; Wakerley, D. W.; Reisner, E.; Hirst, J. Reversible Interconversion of CO_2 and Formate by a Molybdenum-Containing Formate Dehydrogenase. *J. Am. Chem. Soc.* **2014**, *136* (44), 15473−15476.
(253) Wombwell, C.; Reisner, E. Synthesis, structure and reactivity of Ni site models of [NiFeSe] hydrogenases. *Dalton Trans.* **2014**, *43* (11), 4483−4493.
(254) Bachmeier, A.; Armstrong, F. Solar-driven proton and carbon dioxide reduction to fuels — lessons from metalloenzymes. *Curr. Opin. Chem. Biol.* **2015**, *25*, 141−151.
(255) Wang, V. C. C.; Islam, S. T. A.; Can, M.; Ragsdale, S. W.; Armstrong, F. A. Investigations by Protein Film Electrochemistry of Alternative Reactions of Nickel-Containing Carbon Monoxide Dehydrogenase. *J. Phys. Chem. B* **2015**, *119* (43), 13690−13697.
(256) Hexter, S. V.; Chung, M.-W.; Vincent, K. A.; Armstrong, F. A. Unusual Reaction of [NiFe]-Hydrogenases with Cyanide. *J. Am. Chem. Soc.* **2014**, *136* (29), 10470−10477.
(257) Hexter, S. V.; Esterle, T. F.; Armstrong, F. A. A unified model for surface electrocatalysis based on observations with enzymes. *Phys. Chem. Chem. Phys.* **2014**, *16* (24), 11822−11833.
(258) Wulff, P.; Day, C. C.; Sargent, F.; Armstrong, F. A. How oxygen reacts with oxygen-tolerant respiratory [NiFe]-hydrogenases. *Proc. Natl. Acad. Sci. U. S. A.* **2014**, *111* (18), 6606−6611.
(259) Murphy, B. J.; Sargent, F.; Armstrong, F. A. Transforming an oxygen-tolerant [NiFe] uptake hydrogenase into a proficient, reversible hydrogen producer. *Energy Environ. Sci.* **2014**, *7* (4), 1426−1433.
(260) Wang, V. C.-C.; Ragsdale, S. W.; Armstrong, F. A. Investigations of Two Bidirectional Carbon Monoxide Dehydrogenases from *Carboxydothermus hydrogenoformans* by Protein Film Electrochemistry. *ChemBioChem.* **2013**, *14* (14), 1845−1851.
(261) Roessler, M. M.; Evans, R. M.; Davies, R. A.; Harmer, J.; Armstrong, F. A. EPR Spectroscopic Studies of the Fe-S Clusters in the O_2-Tolerant [NiFe]-Hydrogenase Hyd-1 from *Escherichia coli* and Characterization of the Unique [4Fe-3S] Cluster by HYSCORE. *J. Am. Chem. Soc.* **2012**, *134* (37), 15581−15594.
(262) Evans, R. M.; Parkin, A.; Roessler, M. M.; Murphy, B. J.; Adamson, H.; Lukey, M. J.; Sargent, F.; Volbeda, A.; Fontecilla-Camps, J. C.; Armstrong, F. A. Principles of Sustained Enzymatic Hydrogen Oxidation in the Presence of Oxygen - The Crucial Influence of High Potential Fe-S Clusters in the Electron Relay of [NiFe]-Hydrogenases. *J. Am. Chem. Soc.* **2013**, *135* (7), 2694−2707.
(263) Wang, V. C. C.; Can, M.; Pierce, E.; Ragsdale, S. W.; Armstrong, F. A. A Unified Electrocatalytic Description of the Action of Inhibitors of Nickel Carbon Monoxide Dehydrogenase. *J. Am. Chem. Soc.* **2013**, *135* (6), 2198−2206.
(264) Armstrong, F. A. Copying Biology's Ways with Hydrogen. *Science* **2013**, *339* (6120), 658−659.
(265) Hexter, S. V.; Grey, F.; Happe, T.; Climent, V.; Armstrong, F. A. Electrocatalytic mechanism of reversible hydrogen cycling by enzymes and distinctions between the major classes of hydrogenases. *Proc. Natl. Acad. Sci. U. S. A.* **2012**, *109* (29), 11516−11521.
(266) Foster, C. E.; Krämer, T.; Wait, A. F.; Parkin, A.; Jennings, D. P.; Happe, T.; McGrady, J. E.; Armstrong, F. A. Inhibition of [FeFe]-Hydrogenases by Formaldehyde and Wider Mechanistic Implications for Biohydrogen Activation. *J. Am. Chem. Soc.* **2012**, *134* (17), 7553−7557.
(267) Lukey, M. J.; Roessler, M. M.; Parkin, A.; Evans, R. M.; Davies, R. A.; Lenz, O.; Friedrich, B.; Sargent, F.; Armstrong, F. A. Oxygen-Tolerant [NiFe]-Hydrogenases: The Individual and Collective Importance of Supernumerary Cysteines at the Proximal Fe-S Cluster. *J. Am. Chem. Soc.* **2011**, *133* (42), 16881−16892.
(268) Armstrong, F. A.; Hirst, J. Reversibility and efficiency in electrocatalytic energy conversion and lessons from enzymes. *Proc. Natl. Acad. Sci. U. S. A.* **2011**, *108* (34), 14049−14054.
(269) Goldet, G.; Brandmayr, C.; Stripp, S. T.; Happe, T.; Cavazza, C.; Fontecilla-Camps, J. C.; Armstrong, F. A. Electrochemical Kinetic Investigations of the Reactions of [FeFe]-Hydrogenases with Carbon Monoxide and Oxygen: Comparing the Importance of Gas Tunnels and Active-Site Electronic/Redox Effects. *J. Am. Chem. Soc.* **2009**, *131* (41), 14979−14989.
(270) Kim, S. M.; Kong, S. Y.; Kang, J.; Ji, J. S.; Kang, S. H.; Yoon, H.-J.; Kim, H.; Ryu, J.; Lee, H. H.; Kim, Y. H. Fortification of FeS Clusters Reshapes Anaerobic CO Dehydrogenase into an Air-Viable Enzyme Through Multilayered Sealing of O_2 Tunnels. *Angew. Chem., Int. Ed.* **2025**, *64* (33), No. e202508565.
(271) Park, J.; Heo, Y.; Jeon, B. W.; Jung, M.; Kim, Y. H.; Lee, H. H.; Roh, S.-H. Structure of recombinant formate dehydrogenase from *Methylobacterium extorquens* (MeFDH1). *Sci. Rep.* **2024**, *14* (1), 3819.
(272) Kim, S. M.; Lee, J.; Kang, S. H.; Heo, Y.; Yoon, H.-J.; Hahn, J.-S.; Lee, H. H.; Kim, Y. H. O_2-tolerant CO dehydrogenase via tunnel redesign for the removal of CO from industrial flue gas. *Nat. Catal.* **2022**, *5* (9), 807−817.
(273) Liu, Y.; Bin Mohamad Annuar, A.; Rodríguez-Jiménez, S.; Yeung, C. W. S.; Wang, Q.; Coito, A. M.; Manuel, R. R.; Pereira, I. A. C.; Reisner, E. Solar Fuel Synthesis Using a Semiartificial Colloidal Z-Scheme. *J. Am. Chem. Soc.* **2024**, *146* (43), 29865−29876.
(274) Badiani, V. M.; Casadevall, C.; Miller, M.; Cobb, S. J.; Manuel, R. R.; Pereira, I. A. C.; Reisner, E. Engineering Electro- and Photocatalytic Carbon Materials for CO_2 Reduction by Formate Dehydrogenase. *J. Am. Chem. Soc.* **2022**, *144* (31), 14207−14216.

https://doi.org/10.1021/acs.chemrev.5c01010
Chem. Rev. 2026, 126, 4857−4899

(275) Miller, M.; Robinson, W. E.; Oliveira, A. R.; Heidary, N.; Kornienko, N.; Warnan, J.; Pereira, I. A. C.; Reisner, E. Interfacing Formate Dehydrogenase with Metal Oxides for the Reversible Electrocatalysis and Solar-Driven Reduction of Carbon Dioxide. *Angew. Chem., Int. Ed.* **2019**, *58* (14), 4601−4605.
(276) Sokol, K. P.; Robinson, W. E.; Oliveira, A. R.; Warnan, J.; Nowaczyk, M. M.; Ruff, A.; Pereira, I. A. C.; Reisner, E. Photoreduction of CO_2 with a Formate Dehydrogenase Driven by Photosystem II Using a Semi-artificial Z-Scheme Architecture. *J. Am. Chem. Soc.* **2018**, *140* (48), 16418−16422.
(277) Hutton, G. A. M.; Reuillard, B.; Martindale, B. C. M.; Caputo, C. A.; Lockwood, C. W. J.; Butt, J. N.; Reisner, E. Carbon Dots as Versatile Photosensitizers for Solar-Driven Catalysis with Redox Enzymes. *J. Am. Chem. Soc.* **2016**, *138* (51), 16722−16730.
(278) Caputo, C. A.; Wang, L.; Beranek, R.; Reisner, E. Carbon nitride-TiO_2 hybrid modified with hydrogenase for visible light driven hydrogen production. *Chem. Sci.* **2015**, *6* (10), 5690−5694.
(279) Caputo, C. A.; Gross, M. A.; Lau, V. W.; Cavazza, C.; Lotsch, B. V.; Reisner, E. Photocatalytic Hydrogen Production using Polymeric Carbon Nitride with a Hydrogenase and a Bioinspired Synthetic Ni Catalyst. *Angew. Chem., Int. Ed.* **2014**, *53* (43), 11538−11542.
(280) Sakai, T.; Mersch, D.; Reisner, E. Photocatalytic Hydrogen Evolution with a Hydrogenase in a Mediator-Free System under High Levels of Oxygen. *Angew. Chem., Int. Ed.* **2013**, *52* (47), 12313−12316.
(281) Reisner, E. Solar Hydrogen Evolution with Hydrogenases: From Natural to Hybrid Systems. *Eur. J. Inorg. Chem.* **2011**, *2011* (7), 1005−1016.
(282) Wilker, M. B.; Shinopoulos, K. E.; Brown, K. A.; Mulder, D. W.; King, P. W.; Dukovic, G. Electron Transfer Kinetics in CdS Nanorod-[FeFe]-Hydrogenase Complexes and Implications for Photochemical H_2 Generation. *J. Am. Chem. Soc.* **2014**, *136* (11), 4316−4324.
(283) Brown, K. A.; Wilker, M. B.; Boehm, M.; Dukovic, G.; King, P. W. Characterization of Photochemical Processes for H_2 Production by CdS Nanorod-[FeFe] Hydrogenase Complexes. *J. Am. Chem. Soc.* **2012**, *134* (12), 5627−5636.
(284) Brown, K. A.; Dayal, S.; Ai, X.; Rumbles, G.; King, P. W. Controlled Assembly of Hydrogenase-CdTe Nanocrystal Hybrids for Solar Hydrogen Production. *J. Am. Chem. Soc.* **2010**, *132* (28), 9672−9680.
(285) Gao, Y.; Li, W.; Sun, X.; Zhao, Y.; Ji, H.; Luo, H.; Wu, G.; Wan, L.; Zhang, L. Boosting the Performance of Formate Dehydrogenase by Silver Nanoclusters for Photoreduction of CO_2 to Formate. *ACS Sustain. Chem. Eng.* **2022**, *10* (45), 14888−14896.
(286) Li, Q.; Lu, H.; Cheng, M.; Meckenstock, R. U.; Zhou, J.; Zhang, H. Insights into the Direct Photoelectron Transfer Mechanism in Cofactor-free Redox Carbon Dots and Cytochrome *c* Nitrite Reductase Biohybrids Responsible for Ammonia Synthesis. *Environ. Sci. Technol.* **2025**, *59* (13), 6686−6695.
(287) Yoon, J.; Lee, S. H.; Tieves, F.; Rauch, M.; Hollmann, F.; Park, C. B. Light-Harvesting Dye-Alginate Hydrogel for Solar-Driven, Sustainable Biocatalysis of Asymmetric Hydrogenation. *ACS Sustain. Chem. Eng.* **2019**, *7* (6), 5632−5637.
(288) Tucci, F. J.; Rosenzweig, A. C. Direct Methane Oxidation by Copper- and Iron-Dependent Methane Monooxygenases. *Chem. Rev.* **2024**, *124* (3), 1288−1320.
(289) Schulz, C. E.; Castillo, R. G.; Pantazis, D. A.; DeBeer, S.; Neese, F. Structure-Spectroscopy Correlations for Intermediate Q of Soluble Methane Monooxygenase: Insights from QM/MM Calculations. *J. Am. Chem. Soc.* **2021**, *143* (17), 6560−6577.
(290) Tran, N.-H.; Huynh, N.; Bui, T.; Nguyen, Y.; Huynh, P.; Cooper, M. E.; Cheruzel, L. E. Light-initiated hydroxylation of lauric acid using hybrid P450 BM3 enzymes. *Chem. Commun.* **2011**, *47* (43), 11936−11938.
(291) Tran, N.-H.; Huynh, N.; Chavez, G.; Nguyen, A.; Dwaraknath, S.; Nguyen, T.-A.; Nguyen, M.; Cheruzel, L. A series of hybrid P450 BM3 enzymes with different catalytic activity in the light-initiated hydroxylation of lauric acid. *J. Inorg. Biochem.* **2012**, *115*, 50−56.
(292) Tran, N.-H.; Nguyen, D.; Dwaraknath, S.; Mahadevan, S.; Chavez, G.; Nguyen, A.; Dao, T.; Mullen, S.; Nguyen, T.-A.; Cheruzel, L. E. An Efficient Light-Driven P450 BM3 Biocatalyst. *J. Am. Chem. Soc.* **2013**, *135* (39), 14484−14487.
(293) Kato, M.; Nguyen, D.; Gonzalez, M.; Cortez, A.; Mullen, S. E.; Cheruzel, L. E. Regio- and stereoselective hydroxylation of 10-undecenoic acid with a light-driven P450 BM3 biocatalyst yielding a valuable synthon for natural product synthesis. *Bioorg. Med. Chem.* **2014**, *22* (20), 5687−5691.
(294) Zilly, F. E.; Taglieber, A.; Schulz, F.; Hollmann, F.; Reetz, M. T. Deazaflavins as mediators in light-driven cytochrome P450 catalyzed hydroxylations. *Chem. Commun.* **2009**, *46*, 7152−7154.
(295) Park, J. H.; Lee, S. H.; Cha, G. S.; Choi, D. S.; Nam, D. H.; Lee, J. H.; Lee, J.-K.; Yun, C.-H.; Jeong, K. J.; Park, C. B. Cofactor-Free Light-Driven Whole-Cell Cytochrome P450 Catalysis. *Angew. Chem., Int. Ed.* **2015**, *54* (3), 969−973.
(296) Le, T.-K.; Park, J. H.; Choi, D. S.; Lee, G.-Y.; Choi, W. S.; Jeong, K. J.; Park, C. B.; Yun, C.-H. Solar-driven biocatalytic C-hydroxylation through direct transfer of photoinduced electrons. *Green Chem.* **2019**, *21* (3), 515−525.
(297) Vansuch, G. E.; Mulder, D. W.; Chica, B.; Ruzicka, J. L.; Yang, Z.-Y.; Pellows, L. M.; Willis, M. A.; Brown, K. A.; Seefeldt, L. C.; Peters, J. W.; et al. Cryo-annealing of Photoreduced CdS Quantum Dot-Nitrogenase MoFe Protein Complexes Reveals the Kinetic Stability of the E_4(2N2H) Intermediate. *J. Am. Chem. Soc.* **2023**, *145* (39), 21165−21169.
(298) Bachmeier, A.; Murphy, B. J.; Armstrong, F. A. A Multi-Heme Flavoenzyme as a Solar Conversion Catalyst. *J. Am. Chem. Soc.* **2014**, *136* (37), 12876−12879.
(299) De la Rosa, M. A.; Navarro, J. A.; De la Rosa, F. F.; Losada, M. Stabilization by high pH of hydrogen peroxide production with flavin photosystems. *Photobioch. Photobiop.* **1983**, *5* (2), 93−103.
(300) Hockberger, P. E.; Skimina, T. A.; Centonze, V. E.; Lavin, C.; Chu, S.; Dadras, S.; Reddy, J. K.; White, J. G. Activation of flavin-containing oxidases underlies light-induced production of H_2O_2 in mammalian cells. *Proc. Natl. Acad. Sci. U. S. A.* **1999**, *96* (11), 6255−6260.
(301) Choi, D. S.; Ni, Y.; Fernández-Fueyo, E.; Lee, M.; Hollmann, F.; Park, C. B. Photoelectroenzymatic Oxyfunctionalization on Flavin-Hybridized Carbon Nanotube Electrode Platform. *ACS Catal.* **2017**, *7* (3), 1563−1567.
(302) Lee, S. H.; Choi, D. S.; Pesic, M.; Lee, Y. W.; Paul, C. E.; Hollmann, F.; Park, C. B. Cofactor-Free, Direct Photoactivation of Enoate Reductases for the Asymmetric Reduction of C═C Bonds. *Angew. Chem., Int. Ed.* **2017**, *56* (30), 8681−8685.
(303) Kim, J.; Lee, S. H.; Tieves, F.; Paul, C. E.; Hollmann, F.; Park, C. B. Nicotinamide adenine dinucleotide as a photocatalyst. *Sci. Adv.* **2019**, *5* (7), No. eaax0501.
(304) Zhang, H.; Liu, H.; Tian, Z.; Lu, D.; Yu, Y.; Cestellos-Blanco, S.; Sakimoto, K. K.; Yang, P. Bacteria photosensitized by intracellular gold nanoclusters for solar fuel production. *Nat. Nanotechnol.* **2018**, *13* (10), 900−905.
(305) Kornienko, N.; Sakimoto, K. K.; Herlihy, D. M.; Nguyen, S. C.; Alivisatos, A. P.; Harris, C. B.; Schwartzberg, A.; Yang, P. Spectroscopic elucidation of energy transfer in hybrid inorganic-biological organisms for solar-to-chemical production. *Proc. Natl. Acad. Sci. U. S. A.* **2016**, *113* (42), 11750−11755.
(306) Zhang, K.; Li, R.; Chen, J.; Chai, L.; Lin, Z.; Zou, L.; Shi, Y. Biohybrids of twinning $Cd_{0.8}Zn_{0.2}S$ nanoparticles and *Sporomusa ovata* for efficient solar-driven reduction of CO_2 to acetate. *Appl. Catal., B Environ.* **2024**, *342*, 123375.
(307) Wen, N.; Jiang, Q.; Liu, D. Polymer semiconductor films and bacteria hybrid artificial bio-leaves. *Sci. Adv.* **2024**, *10* (44), No. eadp8567.
(308) Jo, H.-J.; Cha, H.-J.; Kim, J.; Adams, J. D.; Yang, P.; Clark, D. S. Two-stage process and strain engineering for continuous

https://doi.org/10.1021/acs.chemrev.5c01010
Chem. Rev. 2026, 126, 4857−4899

bioconversion of CO_2 to butanol. *Bioresour. Technol.* **2026**, *443*, 133842.
(309) Gai, P.; Yu, W.; Zhao, H.; Qi, R.; Li, F.; Liu, L.; Lv, F.; Wang, S. Solar-Powered Organic Semiconductor-Bacteria Biohybrids for CO_2 Reduction into Acetic Acid. *Angew. Chem., Int. Ed.* **2020**, *59* (18), 7224−7229.
(310) Cestellos-Blanco, S.; Zhang, H.; Kim, J. M.; Shen, Y.-x.; Yang, P. Photosynthetic semiconductor biohybrids for solar-driven biocatalysis. *Nat. Catal.* **2020**, *3* (3), 245−255.
(311) Sakimoto, K. K.; Wong, A. B.; Yang, P. Self-photosensitization of nonphotosynthetic bacteria for solar-to-chemical production. *Science* **2016**, *351* (6268), 74−77.
(312) Zwart, J.; van Wolput, J. H. M. C.; van der Cammen, J. C. J. M.; Koningsberger, D. C. Accumulation and reactions of H_2O_2 during the copper ion catalysed autoxidation of cysteine in alkaline medium. *J. Mol. Catal.* **1981**, *11* (1), 69−82.
(313) Sakimoto, K. K.; Zhang, S. J.; Yang, P. Cysteine-Cystine Photoregeneration for Oxygenic Photosynthesis of Acetic Acid from CO_2 by a Tandem Inorganic-Biological Hybrid System. *Nano Lett.* **2016**, *16* (9), 5883−5887.
(314) Kim, J.; Nguyen, T. V. T.; Kim, Y. H.; Hollmann, F.; Park, C. B. Lignin as a multifunctional photocatalyst for solar-powered biocatalytic oxyfunctionalization of C-H bonds. *Nat. Synth.* **2022**, *1* (3), 217−226.
(315) Wang, Y.; Lan, D.; Durrani, R.; Hollmann, F. Peroxygenases en route to becoming dream catalysts. What are the opportunities and challenges? *Curr. Opin. Chem. Biol.* **2017**, *37*, 1−9.
(316) Hobisch, M.; van Schie, M. M. C. H.; Kim, J.; Røjkjær Andersen, K.; Alcalde, M.; Kourist, R.; Park, C. B.; Hollmann, F.; Kara, S. Solvent-Free Photobiocatalytic Hydroxylation of Cyclohexane. *ChemCatChem.* **2020**, *12* (16), 4009−4013.
(317) Deng, X.; Zheng, X.; Jia, F.; Cao, C.; Song, H.; Jiang, Y.; Liu, Y.; Liu, G.; Li, S.; Wang, L. Unspecific peroxygenases immobilized on Pd-loaded three-dimensional ordered macroporous (3DOM) titania photocatalyst for photo-enzyme integrated catalysis. *Appl. Catal., B Environ.* **2023**, *330*, 122622.
(318) Schmermund, L.; Reischauer, S.; Bierbaumer, S.; Winkler, C. K.; Diaz-Rodriguez, A.; Edwards, L. J.; Kara, S.; Mielke, T.; Cartwright, J.; Grogan, G.; et al. Chromoselective Photocatalysis Enables Stereocomplementary Biocatalytic Pathways. *Angew. Chem., Int. Ed.* **2021**, *60* (13), 6965−6969.
(319) Shen, Q.; Zhang, C.; Chen, L.; Huang, B.; Yu, Y.; Zhang, Z.; Zhang, W. Characterization of Pt/g-C_3N_4-Catalyzed Methanol Oxidation to Drive Peroxygenase-Catalyzed Oxyfunctionalization of Hydrocarbons. *ACS Sustain. Chem. Eng.* **2022**, *10* (37), 12156−12164.
(320) Rotilio, L.; Swoboda, A.; Ebner, K.; Rinnofner, C.; Glieder, A.; Kroutil, W.; Mattevi, A. Structural and Biochemical Studies Enlighten the Unspecific Peroxygenase from Hypoxylon sp. EC38 as an Efficient Oxidative Biocatalyst. *ACS Catal.* **2021**, *11* (18), 11511−11525.
(321) Lee, M.; Jang, J.; Cha, J.; Lee, S. H.; Hollmann, F.; Won, K.; Park, C. B. Fallen-leaf-sensitized biosolar oxygenation of hydrocarbons. *Green Chem.* **2026**, *28* (6), 2822−2833.
(322) Karich, A.; Scheibner, K.; Ullrich, R.; Hofrichter, M. Exploring the catalase activity of unspecific peroxygenases and the mechanism of peroxide-dependent heme destruction. *J. Mol. Catal. B Enzym.* **2016**, *134*, 238−246.
(323) Zhang, W.; Fernández-Fueyo, E.; Ni, Y.; van Schie, M.; Gacs, J.; Renirie, R.; Wever, R.; Mutti, F. G.; Rother, D.; Alcalde, M.; et al. Selective aerobic oxidation reactions using a combination of photocatalytic water oxidation and enzymatic oxyfunctionalizations. *Nat. Catal.* **2018**, *1* (1), 55−62.
(324) Freakley, S. J.; Kochius, S.; van Marwijk, J.; Fenner, C.; Lewis, R. J.; Baldenius, K.; Marais, S. S.; Opperman, D. J.; Harrison, S. T. L.; Alcalde, M.; et al. A chemo-enzymatic oxidation cascade to activate C-H bonds with in situ generated H_2O_2. *Nat. Commun.* **2019**, *10* (1), 4178.
(325) De Santis, P.; Wegstein, D.; Burek, B. O.; Patzsch, J.; Alcalde, M.; Kroutil, W.; Bloh, J. Z.; Kara, S. Robust Light Driven Enzymatic Oxyfunctionalization via Immobilization of Unspecific Peroxygenase. *ChemSusChem* **2023**, *16* (23), No. e202300613.
(326) Aranda, C.; Carro, J.; González-Benjumea, A.; Babot, E. D.; Olmedo, A.; Linde, D.; Martínez, A. T.; Gutiérrez, A. Advances in enzymatic oxyfunctionalization of aliphatic compounds. *Biotechnol. Adv.* **2021**, *51*, 107703.
(327) Zhang, W.; Burek, B. O.; Fernández-Fueyo, E.; Alcalde, M.; Bloh, J. Z.; Hollmann, F. Selective Activation of C-H Bonds in a Cascade Process Combining Photochemistry and Biocatalysis. *Angew. Chem., Int. Ed.* **2017**, *56* (48), 15451−15455.
(328) van Schie, M. M. C. H.; Zhang, W.; Tieves, F.; Choi, D. S.; Park, C. B.; Burek, B. O.; Bloh, J. Z.; Arends, I. W. C. E.; Paul, C. E.; Alcalde, M.; et al. Cascading g-C_3N_4 and Peroxygenases for Selective Oxyfunctionalization Reactions. *ACS Catal.* **2019**, *9* (8), 7409−7417.
(329) Willot, S. J. P.; Fernández-Fueyo, E.; Tieves, F.; Pesic, M.; Alcalde, M.; Arends, I. W. C. E.; Park, C. B.; Hollmann, F. Expanding the Spectrum of Light-Driven Peroxygenase Reactions. *ACS Catal.* **2019**, *9* (2), 890−894.
(330) Lee, J.; Jo, Y.; Yeon, S.; Jang, J.; Ha, J.; Sohn, B.; Cho, H.; Kim, G.-M.; Lee, D. C.; Park, C. B.; et al. All-Inorganic InP/ZnSe/ZnS Quantum Dots with Chalcogenidometallate Ligands for Biosolar Catalysis. *Adv. Funct. Mater.* **2025**, *35* (52), No. e11671.
(331) Lee, C. H.; Park, C. B. Heteroatom-Engineered Linear Conjugated Polymers for Photocatalytic O_2 Reduction and Biocatalytic sp^3 C−H Oxyfunctionalization. *Adv. Funct. Mater.* **2026**, No. e74537.
(332) Schneider, J.; Bahnemann, D. W. Undesired Role of Sacrificial Reagents in Photocatalysis. *J. Phys. Chem. Lett.* **2013**, *4* (20), 3479−3483.
(333) Pellegrin, Y.; Odobel, F. Sacrificial electron donor reagents for solar fuel production. *C. R. Chim.* **2017**, *20* (3), 283−295.
(334) Jang, J.; Aurangzeb Khan, W.; Hollmann, F.; Won, K.; Park, C. B. Biosolar Oxygenation of Hydrocarbons by Photocatalytic Artificial Wood. *ACS Sustain. Chem. Eng.* **2024**, *12* (23), 8950−8957.
(335) Zhang, W.; Liu, H.; van Schie, M. M. C. H.; Hagedoorn, P.-L.; Alcalde, M.; Denkova, A. G.; Djanashvili, K.; Hollmann, F. Nuclear Waste and Biocatalysis: A Sustainable Liaison? *ACS Catal.* **2020**, *10* (23), 14195−14200.
(336) Kumar, N.; He, J.; Rusling, J. F. Electrochemical transformations catalyzed by cytochrome P450s and peroxidases. *Chem. Soc. Rev.* **2023**, *52* (15), 5135−5171.
(337) Chen, H.; Hirao, H.; Derat, E.; Schlichting, I.; Shaik, S. Quantum Mechanical/Molecular Mechanical Study on the Mechanisms of Compound I Formation in the Catalytic Cycle of Chloroperoxidase: An Overview on Heme Enzymes. *J. Phys. Chem. B* **2008**, *112* (31), 9490−9500.
(338) Manoj, K. M.; Hager, L. P. Chloroperoxidase, a Janus Enzyme. *Biochemistry* **2008**, *47* (9), 2997−3003.
(339) Yuan, B.; Mahor, D.; Fei, Q.; Wever, R.; Alcalde, M.; Zhang, W.; Hollmann, F. Water-Soluble Anthraquinone Photocatalysts Enable Methanol-Driven Enzymatic Halogenation and Hydroxylation Reactions. *ACS Catal.* **2020**, *10* (15), 8277−8284.
(340) Jia, J.; Huo, Q.; Yang, D.; Sun, Y.; Zhang, S.; Li, S.; Shi, J.; Jiang, Z. Granum-Inspired Photoenzyme-Coupled Catalytic System via Stacked Polymeric Carbon Nitride. *ACS Catal.* **2021**, *11* (15), 9210−9220.
(341) Zhao, Z.; Wu, Y.; Liu, C.; Li, Y.; Gong, C.; Ning, H.; Zhang, P.; Li, F.; Sun, L.; Li, F. Bio-inspired Catalyst-Modified Photocathode for Bias-Free Photoelectrochemical NADH Regeneration. *Adv. Sci.* **2025**, *12* (8), 2413668.
(342) Lee, Y. W.; Boonmongkolras, P.; Son, E. J.; Kim, J.; Lee, S. H.; Kuk, S. K.; Ko, J. W.; Shin, B.; Park, C. B. Unbiased biocatalytic solar-to-chemical conversion by FeOOH/$BiVO_4$/perovskite tandem structure. *Nat. Commun.* **2018**, *9* (1), 4208.
(343) Kim, J.; Um, Y.; Han, S.; Hilberath, T.; Kim, Y. H.; Hollmann, F.; Park, C. B. Unbiased Photoelectrode Interfaces for Solar Coupling of Lignin Oxidation with Biocatalytic C═C Bond Hydrogenation. *ACS Appl. Mater. Interfaces* **2022**, *14* (9), 11465−11473.

https://doi.org/10.1021/acs.chemrev.5c01010
Chem. Rev. 2026, 126, 4857−4899

(344) Kuk, S. K.; Singh, R. K.; Nam, D. H.; Singh, R.; Lee, J.-K.; Park, C. B. Photoelectrochemical Reduction of Carbon Dioxide to Methanol through a Highly Efficient Enzyme Cascade. *Angew. Chem., Int. Ed.* **2017**, *56* (14), 3827−3832.
(345) Son, E. J.; Lee, S. H.; Kuk, S. K.; Pesic, M.; Choi, D. S.; Ko, J. W.; Kim, K.; Hollmann, F.; Park, C. B. Carbon Nanotube-Graphitic Carbon Nitride Hybrid Films for Flavoenzyme-Catalyzed Photoelectrochemical Cells. *Adv. Funct. Mater.* **2018**, *28* (24), 1705232.
(346) Choi, D. S.; Kim, J.; Hollmann, F.; Park, C. B. Solar-Assisted eBiorefinery: Photoelectrochemical Pairing of Oxyfunctionalization and Hydrogenation Reactions. *Angew. Chem., Int. Ed.* **2020**, *59* (37), 15886−15890.
(347) Ishibashi, T.; Higashi, M.; Ikeda, S.; Amao, Y. Photoelectrochemical CO_2 Reduction to Formate with the Sacrificial Reagent Free System of Semiconductor Photocatalysts and Formate Dehydrogenase. *ChemCatChem.* **2019**, *11* (24), 6227−6235.
(348) Li, N.; You, J.; Huang, L.; Zhang, H.; Wang, X.; He, L.; Gong, C.; Lin, S.; Zhang, B. Photoelectrochemical NADH regeneration on a polymer semiconductor-based photocathode. *Green Chem.* **2023**, *25* (13), 5247−5256.
(349) Kim, J.; Jang, J.; Hilberath, T.; Hollmann, F.; Park, C. B. Photoelectrocatalytic biosynthesis fuelled by microplastics. *Nat. Synth.* **2022**, *1* (10), 776−786.
(350) Lee, C. H.; Kim, J.; Park, C. B. Z-Schematic Artificial Leaf Structure for Biosolar Oxyfunctionalization of Hydrocarbons. *ACS Energy Lett.* **2023**, *8* (6), 2513−2521.
(351) Lee, Y. S.; Gerulskis, R.; Minteer, S. D. Advances in electrochemical cofactor regeneration: enzymatic and non-enzymatic approaches. *Curr. Opin. Biotechnol.* **2022**, *73*, 14−21.
(352) Nam, D. H.; Kuk, S. K.; Choe, H.; Lee, S.; Ko, J. W.; Son, E. J.; Choi, E.-G.; Kim, Y. H.; Park, C. B. Enzymatic photosynthesis of formate from carbon dioxide coupled with highly efficient photoelectrochemical regeneration of nicotinamide cofactors. *Green Chem.* **2016**, *18* (22), 5989−5993.
(353) Nam, D. H.; Ryu, G. M.; Kuk, S. K.; Choi, D. S.; Son, E. J.; Park, C. B. Water oxidation-coupled, photoelectrochemical redox biocatalysis toward mimicking natural photosynthesis. *Appl. Catal., B Environ.* **2016**, *198*, 311−317.
(354) Xu, K.; Chatzitakis, A.; Backe, P. H.; Ruan, Q.; Tang, J.; Rise, F.; Bjørås, M.; Norby, T. In situ cofactor regeneration enables selective CO_2 reduction in a stable and efficient enzymatic photoelectrochemical cell. *Appl. Catal., B Environ.* **2021**, *296*, 120349.
(355) Higashi, M.; Toyodome, T.; Kano, K.; Amao, Y. Photoelectrochemical lactate production from pyruvate via in situ NADH regeneration over a hybrid system of CdS photoanode and lactate dehydrogenase. *Electrochim. Acta* **2023**, *460*, 142590.
(356) Mukha, D.; Cohen, Y.; Yehezkeli, O. Bismuth Vanadate/Bilirubin Oxidase Photo(bio)electrochemical Cells for Unbiased, Light-Triggered Electrical Power Generation. *ChemSusChem* **2020**, *13* (10), 2684−2692.
(357) Zhao, J.; Zhang, H.; Sun, X.; Hao, S.; Zhao, P.; Zhu, X.; Dong, S. Bifunctional bio-photoelectrochemical cells: a "trading" platform for simultaneous production of electric power and hydrogen peroxide. *J. Mater. Chem. A* **2023**, *11* (2), 600−608.
(358) Zhao, Z.; Li, Z.; Zou, Z. Electronic structure and optical properties of monoclinic clinobisvanite $BiVO_4$. *Phys. Chem. Chem. Phys.* **2011**, *13* (10), 4746−4753.
(359) Xing, F.; Xue, X.; Li, J.; Liu, J.; Wang, W.; Dong, W.; Yuan, H.; Liu, J. Sustainable Photocatalytic Biological Cofactor Regeneration Fueled by Selective Alcohol Oxidation over Polarized $ZnIn_2S_4$. *ACS Catal.* **2024**, *14* (15), 11366−11377.
(360) Wang, X.; Saba, T.; Yiu, H. H. P.; Howe, R. F.; Anderson, J. A.; Shi, J. Cofactor NAD(P)H Regeneration Inspired by Heterogeneous Pathways. *Chem.* **2017**, *2* (5), 621−654.
(361) Poizat, M.; Arends, I. W. C. E.; Hollmann, F. On the nature of mutual inactivation between $[Cp^*Rh(bpy)(H_2O)]^{2+}$ and enzymes - analysis and potential remedies. *J. Mol. Catal. B Enzym.* **2010**, *63* (3), 149−156.
(362) Lin, Q.; Li, Q.; Batchelor-McAuley, C.; Compton, R. G. Use of 'split waves' for the measurement of electrocatalytic kinetics: methyl viologen mediated oxygen reduction on a boron-doped diamond electrode. *Phys. Chem. Chem. Phys.* **2013**, *15* (20), 7760−7767.
(363) Zhao, F.; Wang, P.; Ruff, A.; Hartmann, V.; Zacarias, S.; Pereira, I. A. C.; Nowaczyk, M. M.; Rögner, M.; Conzuelo, F.; Schuhmann, W. A photosystem I monolayer with anisotropic electron flow enables Z-scheme like photosynthetic water splitting. *Energy Environ. Sci.* **2019**, *12* (10), 3133−3143.
(364) Mersch, D.; Lee, C.-Y.; Zhang, J. Z.; Brinkert, K.; Fontecilla-Camps, J. C.; Rutherford, A. W.; Reisner, E. Wiring of Photosystem II to Hydrogenase for Photoelectrochemical Water Splitting. *J. Am. Chem. Soc.* **2015**, *137* (26), 8541−8549.
(365) Zhang, J. Z.; Reisner, E. Advancing photosystem II photoelectrochemistry for semi-artificial photosynthesis. *Nat. Rev. Chem.* **2020**, *4* (1), 6−21.
(366) Nayak, P. K.; Mahesh, S.; Snaith, H. J.; Cahen, D. Photovoltaic solar cell technologies: analysing the state of the art. *Nat. Rev. Mater.* **2019**, *4* (4), 269−285.
(367) Green, M. A.; Ho-Baillie, A.; Snaith, H. J. The emergence of perovskite solar cells. *Nat. Photonics* **2014**, *8* (7), 506−514.
(368) Antón-García, D.; Edwardes Moore, E.; Bajada, M. A.; Eisenschmidt, A.; Oliveira, A. R.; Pereira, I. A. C.; Warnan, J.; Reisner, E. Photoelectrochemical hybrid cell for unbiased CO_2 reduction coupled to alcohol oxidation. *Nat. Synth.* **2022**, *1* (1), 77−86.
(369) Bhattacharjee, S.; Rahaman, M.; Andrei, V.; Miller, M.; Rodríguez-Jiménez, S.; Lam, E.; Pornrungroj, C.; Reisner, E. Photoelectrochemical CO_2-to-fuel conversion with simultaneous plastic reforming. *Nat. Synth.* **2023**, *2* (2), 182−192.
(370) Boucher, D. G.; Minteer, S. D. Making molecules with microplastics. *Nat. Synth.* **2022**, *1* (10), 751−752.
(371) Liu, Y.; Yeung, C. W. S.; Reisner, E. Photoelectrochemical comproportionation of pre-treated PET plastics and CO_2 to formate. *Energy Environ. Sci.* **2025**, *18*, 7023.
(372) Kim, J.; Cestellos-Blanco, S.; Shen, Y.-x.; Cai, R.; Yang, P. Enhancing Biohybrid CO_2 to Multicarbon Reduction via Adapted Whole-Cell Catalysts. *Nano Lett.* **2022**, *22* (13), 5503−5509.
(373) Cestellos-Blanco, S.; Chan, R. R.; Shen, Y.-x.; Kim, J. M.; Tacken, T. A.; Ledbetter, R.; Yu, S.; Seefeldt, L. C.; Yang, P. Photosynthetic biohybrid coculture for tandem and tunable CO_2 and N_2 fixation. *Proc. Natl. Acad. Sci. U. S. A.* **2022**, *119* (26), No. e2122364119.
(374) Lee, W.; Liu, A.; Lin, J.-A.; Leng, T.; Kim, J.; Guo, N.; Kim, J.; Jayasinghe, L.; Shan, Y.; Yang, P. Red-Light-Driven Biophotochemical Diode Based on a Microorganism-Silicon Nanowire Interface for Stable and Efficient Bias-Free CO_2 Reduction. *Nano Lett.* **2025**, *25* (49), 17129−17137.
(375) Yang, P. Liquid Sunlight: The Evolution of Photosynthetic Biohybrids. *Nano Lett.* **2021**, *21* (13), 5453−5456.
(376) Andrei, V.; Roh, I.; Yang, P. Nanowire photochemical diodes for artificial photosynthesis. *Sci. Adv.* **2023**, *9* (6), No. eade9044.
(377) Kim, J.; Park, C. B. Collaborative catalysis for solar biosynthesis. *Trends Chem.* **2023**, *5* (2), 133−146.
(378) Chen, C.; Takumu, N.; Cai, W.; Zhang, Q.; Ohno, T. Visible Light-Driven H_2O_2 Photoelectrocatalytic Synthesis Over a Tandem Electrode Strategy. *Photocatal. Res. Potential* **2024**, *1*, 10003.
(379) Choi, D. S.; Lee, H.; Tieves, F.; Lee, Y. W.; Son, E. J.; Zhang, W.; Shin, B.; Hollmann, F.; Park, C. B. Bias-Free In Situ H_2O_2 Generation in a Photovoltaic-Photoelectrochemical Tandem Cell for Biocatalytic Oxyfunctionalization. *ACS Catal.* **2019**, *9* (11), 10562−10566.
(380) Ko, M.; Pham, L. T. M.; Sa, Y. J.; Woo, J.; Nguyen, T. V. T.; Kim, J. H.; Oh, D.; Sharma, P.; Ryu, J.; Shin, T. J.; et al. Unassisted solar lignin valorisation using a compartmented photo-electro-biochemical cell. *Nat. Commun.* **2019**, *10* (1), 5123.
(381) Kim, C. H.; Lee, C. H.; Lee, M.; Oh, D.; Hong, Y.; Yu, H.-M.; Jung, W.; Hollmann, F.; Park, C. B. Hydrated CO2-mediated redox

https://doi.org/10.1021/acs.chemrev.5c01010
Chem. Rev. 2026, 126, 4857−4899

chemistry for biophotoelectrocatalytic oxyfunctionalization of C-H bonds. *Nat. Synth.* **2026**, DOI: 10.1038/s44160-026-00998-6.
(382) Ning, C.-Z.; Dou, L.; Yang, P. Bandgap engineering in semiconductor alloy nanomaterials with widely tunable compositions. *Nat. Rev. Mater.* **2017**, *2* (12), 17070.
(383) Chaves, A.; Azadani, J. G.; Alsalman, H.; da Costa, D. R.; Frisenda, R.; Chaves, A. J.; Song, S. H.; Kim, Y. D.; He, D.; Zhou, J.; et al. Bandgap engineering of two-dimensional semiconductor materials. *npj 2D Mater. Appl.* **2020**, *4* (1), 29.
(384) Young, J. L.; Steiner, M. A.; Döscher, H.; France, R. M.; Turner, J. A.; Deutsch, T. G. Direct solar-to-hydrogen conversion via inverted metamorphic multi-junction semiconductor architectures. *Nat. Energy* **2017**, *2* (4), 17028.
(385) Jia, J.; Seitz, L. C.; Benck, J. D.; Huo, Y.; Chen, Y.; Ng, J. W. D.; Bilir, T.; Harris, J. S.; Jaramillo, T. F. Solar water splitting by photovoltaic-electrolysis with a solar-to-hydrogen efficiency over 30%. *Nat. Commun.* **2016**, *7* (1), 13237.
(386) Guo, H.; Meng, R.; Wang, G.; Wang, S.; Wu, L.; Li, J.; Wang, Z.; Dong, J.; Hao, X.; Zhang, Y. Band-gap-graded $Cu_2ZnSn(S,Se)_4$ drives highly efficient solar cells. *Energy Environ. Sci.* **2022**, *15* (2), 693−704.
(387) Vilanova, A.; Dias, P.; Lopes, T.; Mendes, A. The route for commercial photoelectrochemical water splitting: a review of large-area devices and key upscaling challenges. *Chem. Soc. Rev.* **2024**, *53* (5), 2388−2434.
(388) Huang, H.; Dai, B.; Wang, W.; Lu, C.; Kou, J.; Ni, Y.; Wang, L.; Xu, Z. Oriented Built-in Electric Field Introduced by Surface Gradient Diffusion Doping for Enhanced Photocatalytic H_2 Evolution in CdS Nanorods. *Nano Lett.* **2017**, *17* (6), 3803−3808.
(389) Oener, S. Z.; Cavalli, A.; Sun, H.; Haverkort, J. E. M.; Bakkers, E. P. A. M.; Garnett, E. C. Charge carrier-selective contacts for nanowire solar cells. *Nat. Commun.* **2018**, *9* (1), 3248.
(390) Lim, K.; Sima, M.; Stewart, R. J.; Minteer, S. D. Direct bioelectrocatalysis by redox enzymes immobilized in electrostatically condensed oppositely charged polyelectrolyte electrode coatings. *Analyst* **2020**, *145* (4), 1250−1257.
(391) VandeZande, G. R.; Olvany, J. M.; Rutherford, J. L.; Rasmussen, M. Enzyme Immobilization and Mediation with Osmium Redox Polymers. In *Enzyme Stabilization and Immobilization: Methods and Protocols*; Minteer, S. D., Ed.; Springer New York, 2017; pp 165−179.
(392) Grattieri, M.; Patterson, S.; Copeland, J.; Klunder, K.; Minteer, S. D. Purple Bacteria and 3D Redox Hydrogels for Bioinspired Photo-bioelectrocatalysis. *ChemSusChem* **2020**, *13* (1), 230−237.
(393) Yuan, M.; Kummer, M. J.; Milton, R. D.; Quah, T.; Minteer, S. D. Efficient NADH Regeneration by a Redox Polymer-Immobilized Enzymatic System. *ACS Catal.* **2019**, *9* (6), 5486−5495.
(394) Lee, Y. S.; Yuan, M.; Cai, R.; Lim, K.; Minteer, S. D. Nitrogenase Bioelectrocatalysis: ATP-Independent Ammonia Production Using a Redox Polymer/MoFe Protein System. *ACS Catal.* **2020**, *10* (12), 6854−6861.
(395) Moser, C. C.; Anderson, J. L. R.; Dutton, P. L. Guidelines for tunneling in enzymes. *Biochim. Biophys. Acta - Bioenerg.* **2010**, *1797* (9), 1573−1586.
(396) Algov, I.; Alfonta, L. Use of Protein Engineering to Elucidate Electron Transfer Pathways between Proteins and Electrodes. *ACS Meas. Sci. Au* **2022**, *2* (2), 78−90.
(397) Flexer, V.; Chen, J.; Donose, B. C.; Sherrell, P.; Wallace, G. G.; Keller, J. The nanostructure of three-dimensional scaffolds enhances the current density of microbial bioelectrochemical systems. *Energy Environ. Sci.* **2013**, *6* (4), 1291−1298.
(398) Riedel, M.; Lisdat, F. Integration of Enzymes in Polyaniline-Sensitized 3D Inverse Opal TiO_2 Architectures for Light-Driven Biocatalysis and Light-to-Current Conversion. *ACS Appl. Mater. Interfaces* **2018**, *10* (1), 267−277.
(399) Riedel, M.; Wersig, J.; Ruff, A.; Schuhmann, W.; Zouni, A.; Lisdat, F. A Z-Scheme-Inspired Photobioelectrochemical H_2O/O_2 Cell with a 1 V Open-Circuit Voltage Combining Photosystem II and PbS Quantum Dots. *Angew. Chem., Int. Ed.* **2019**, *58* (3), 801−805.
(400) Guo, J.; Yang, L.; Zhao, C.; Gao, Z.; Song, Y.-Y.; Schmuki, P. Constructing a photo-enzymatic cascade reaction and its in situ monitoring: enzymes hierarchically trapped in titania meso-porous MOFs as a new photosynthesis platform. *J. Mater. Chem. A* **2021**, *9* (26), 14911−14919.
(401) Dumanović, J.; Nepovimova, E.; Natić, M.; Kuča, K.; Jaćević, V. The Significance of Reactive Oxygen Species and Antioxidant Defense System in Plants: A Concise Overview. *Front. Plant Sci.* **2021**, *11*, 552969.
(402) Li, K.; Zou, H.; Tong, X.; Yang, H. Enhanced Photo-biocatalytic Cascades at Pickering Droplet Interfaces. *J. Am. Chem. Soc.* **2024**, *146* (25), 17054−17065.
(403) He, L.; Guo, H.; Lu, J.; Liu, Q.; Qiu, X. Enhanced Antioxidation and UV-Absorption Ability of Industrial Lignin via Promoting Phenolic Contents and Hydrophilicity. *ACS Omega* **2025**, *10* (7), 6745−6752.
(404) Kiokias, S.; Varzakas, T.; Oreopoulou, V. In Vitro Activity of Vitamins, Flavonoids, and Natural Phenolic Antioxidants Against the Oxidative Deterioration of Oil-Based Systems. *Crit. Rev. Food Sci. Nutr.* **2008**, *48* (1), 78−93.
(405) Sang, S.; Lapsley, K.; Jeong, W.-S.; Lachance, P. A.; Ho, C.-T.; Rosen, R. T. Antioxidative Phenolic Compounds Isolated from Almond Skins (*Prunus amygdalus* Batsch). *J. Agric. Food Chem.* **2002**, *50* (8), 2459−2463.
(406) Cervato, G.; Viani, P.; Gatti, P.; Cestaro, B. Studies on lipid peroxidation in different model membranes: role of cysteamine. *Chem. Phys. Lipids* **1992**, *62* (1), 31−38.
(407) Uribe, P.; Meriño, J.; Bravo, A.; Zambrano, F.; Schulz, M.; Villegas, J. V.; Sánchez, R. Antioxidant effects of penicillamine against in vitro-induced oxidative stress in human spermatozoa. *Andrologia* **2020**, *52* (5), No. e13553.
(408) Mirzahosseini, A.; Noszál, B. Species-Specific Standard Redox Potential of Thiol-Disulfide Systems: A Key Parameter to Develop Agents against Oxidative Stress. *Sci. Rep.* **2016**, *6* (1), 37596.
(409) Bakheit, A. H.; Wani, T. A.; Al-Majed, A. A.; Alkahtani, H. M.; Alanazi, M. M.; Alqahtani, F. R.; Zargar, S. Theoretical study of the antioxidant mechanism and structure-activity relationships of 1,3,4-oxadiazol-2-ylthieno[2,3-d]pyrimidin-4-amine derivatives: a computational approach. *Front. Chem.* **2024**, *12*, 1443718.
(410) Iuga, C.; Campero, A.; Vivier-Bunge, A. Antioxidant vs. prooxidant action of phenothiazine in a biological environment in the presence of hydroxyl and hydroperoxyl radicals: a quantum chemistry study. *RSC Adv.* **2015**, *5* (19), 14678−14689.
(411) David, A. E.; Yang, A. J.; Wang, N. S. Enzyme Stabilization and Immobilization by Sol-Gel Entrapment. In *Enzyme Stabilization and Immobilization: Methods and Protocols*; Minteer, S. D., Ed.; Humana Press, 2011; pp 49−66.
(412) Le, T.; Chan, S.; Ebaid, B.; Sommerhalter, M. Silica Sol-Gel Entrapment of the Enzyme Chloroperoxidase. *J. Nanotechnol.* **2015**, *2015* (1), 632076.
(413) Samu, G. F.; Janáky, C. Photocorrosion at Irradiated Perovskite/Electrolyte Interfaces. *J. Am. Chem. Soc.* **2020**, *142* (52), 21595−21614.
(414) Luo, Z.; Zhang, S.; Ye, X.; Xue, S.; Chen, J.; Huang, M.; Yang, C.; Zhang, J.; Hou, Y.; Yu, Z.; et al. Direct Conversion of Passivated Photo-Corroded Sites into Active Co-Catalysts via In Situ Targeting. *Adv. Funct. Mater.* **2026**, *36* (5), No. e13976.
(415) Xiao, M.; Wang, Z.; Maeda, K.; Liu, G.; Wang, L. Addressing the stability challenge of photo(electro)catalysts towards solar water splitting. *Chem. Sci.* **2023**, *14* (13), 3415−3427.
(416) Kim, W.; Tachikawa, T.; Majima, T.; Choi, W. Photocatalysis of Dye-Sensitized TiO_2 Nanoparticles with Thin Overcoat of Al_2O_3: Enhanced Activity for H_2 Production and Dechlorination of CCl_4. *J. Phys. Chem. C* **2009**, *113* (24), 10603−10609.
(417) Fan, Z.; Xu, Z.; Yan, S.; Zou, Z. Tuning the ion permeability of an Al_2O_3 coating layer on Fe_2O_3 photoanodes for improved

photoelectrochemical water oxidation. *J. Mater. Chem. A* **2017**, *5* (18), 8402−8407.
(418) Li, X.; Wang, J.; Zhang, T.; Wang, T.; Zhao, Y. Photoelectrochemical Catalysis of Waste Polyethylene Terephthalate Plastic to Coproduce Formic Acid and Hydrogen. *ACS Sustain. Chem. Eng.* **2022**, *10* (29), 9546−9552.
(419) Zhang, L.; Etienne, M.; Vilà, N.; Le, T. X. H.; Kohring, G.-W.; Walcarius, A. Electrocatalytic Biosynthesis using a Bucky Paper Functionalized by $[Cp^*Rh(bpy)Cl]^+$ and a Renewable Enzymatic Layer. *ChemCatChem.* **2018**, *10* (18), 4067−4073.
(420) Chen, M.; Liu, F.; Wu, Y.; Li, Y.; Liu, C.; Zhao, Z.; Zhang, P.; Zhao, Y.; Sun, L.; Li, F. Bioinspired photoelectrochemical NADH regeneration based on a molecular catalyst-modified photocathode. *Chem. Commun.* **2024**, *60* (24), 3319−3322.
(421) Weng, B.; Qi, M.-Y.; Han, C.; Tang, Z.-R.; Xu, Y.-J. Photocorrosion Inhibition of Semiconductor-Based Photocatalysts: Basic Principle, Current Development, and Future Perspective. *ACS Catal.* **2019**, *9* (5), 4642−4687.
(422) Yan, W.; Zhou, L.; Luo, Z.; Ding, S.; Li, D.; Lin, X. Cell-Membrane-Inspired Ultrathin Silica Nanochannels Coating for Long-Term Stable Photoelectrocatalysis with Enhanced Performance. *Adv. Sci.* **2024**, *11* (44), 2407686.
(423) Cao, Y.-Q.; Zi, T.-Q.; Zhao, X.-R.; Liu, C.; Ren, Q.; Fang, J.-B.; Li, W.-M.; Li, A.-D. Enhanced visible light photocatalytic activity of Fe_2O_3 modified TiO_2 prepared by atomic layer deposition. *Sci. Rep.* **2020**, *10* (1), 13437.
(424) Sathe, P.; Laxman, K.; Myint, M. T. Z.; Dobretsov, S.; Richter, J.; Dutta, J. Bioinspired nanocoatings for biofouling prevention by photocatalytic redox reactions. *Sci. Rep.* **2017**, *7* (1), 3624.
(425) Wang, Q.; Hisatomi, T.; Jia, Q.; Tokudome, H.; Zhong, M.; Wang, C.; Pan, Z.; Takata, T.; Nakabayashi, M.; Shibata, N.; et al. Scalable water splitting on particulate photocatalyst sheets with a solar-to-hydrogen energy conversion efficiency exceeding 1%. *Nat. Mater.* **2016**, *15* (6), 611−615.
(426) Bu, T.; Liu, X.; Zhou, Y.; Yi, J.; Huang, X.; Luo, L.; Xiao, J.; Ku, Z.; Peng, Y.; Huang, F.; et al. A novel quadruple-cation absorber for universal hysteresis elimination for high efficiency and stable perovskite solar cells. *Energy Environ. Sci.* **2017**, *10* (12), 2509−2515.
(427) Kakavelakis, G.; Paradisanos, I.; Paci, B.; Generosi, A.; Papachatzakis, M.; Maksudov, T.; Najafi, L.; Del Rio Castillo, A. E.; Kioseoglou, G.; Stratakis, E.; et al. Extending the Continuous Operating Lifetime of Perovskite Solar Cells with a Molybdenum Disulfide Hole Extraction Interlayer. *Adv. Energy Mater.* **2018**, *8* (12), 1702287.
(428) Zhang, W.; Saliba, M.; Moore, D. T.; Pathak, S. K.; Hörantner, M. T.; Stergiopoulos, T.; Stranks, S. D.; Eperon, G. E.; Alexander-Webber, J. A.; Abate, A.; et al. Ultrasmooth organic-inorganic perovskite thin-film formation and crystallization for efficient planar heterojunction solar cells. *Nat. Commun.* **2015**, *6* (1), 6142.
(429) Andrei, V.; Hoye, R. L. Z.; Crespo-Quesada, M.; Bajada, M.; Ahmad, S.; De Volder, M.; Friend, R.; Reisner, E. Scalable Triple Cation Mixed Halide Perovskite-$BiVO_4$ Tandems for Bias-Free Water Splitting. *Adv. Energy Mater.* **2018**, *8* (25), 1801403.
(430) Karak, S.; Liu, Y.; Annuar, A. B. M.; Reisner, E. Covalent Organic Framework and Carbon Nitride Composite for Scalable Solar Reforming. *Adv. Mater.* **2026**, *38*, No. e13457.
(431) Willner, I.; Katz, E. Integration of Layered Redox Proteins and Conductive Supports for Bioelectronic Applications. *Angew. Chem., Int. Ed.* **2000**, *39* (7), 1180−1218.
(432) Lee, Y. S.; Ruff, A.; Cai, R.; Lim, K.; Schuhmann, W.; Minteer, S. D. Electroenzymatic Nitrogen Fixation Using a MoFe Protein System Immobilized in an Organic Redox Polymer. *Angew. Chem., Int. Ed.* **2020**, *59* (38), 16511−16516.
(433) Weliwatte, N. S.; Grattieri, M.; Simoska, O.; Rhodes, Z.; Minteer, S. D. Unbranched Hybrid Conducting Redox Polymers for Intact Chloroplast-Based Photobioelectrocatalysis. *Langmuir* **2021**, *37* (25), 7821−7833.
(434) Bachmeier, A.; Wang, V. C. C.; Woolerton, T. W.; Bell, S.; Fontecilla-Camps, J. C.; Can, M.; Ragsdale, S. W.; Chaudhary, Y. S.; Armstrong, F. A. How Light-Harvesting Semiconductors Can Alter the Bias of Reversible Electrocatalysts in Favor of H_2 Production and CO_2 Reduction. *J. Am. Chem. Soc.* **2013**, *135* (40), 15026−15032.
(435) Weekes, D. M.; Salvatore, D. A.; Reyes, A.; Huang, A.; Berlinguette, C. P. Electrolytic CO_2 Reduction in a Flow Cell. *Acc. Chem. Res.* **2018**, *51* (4), 910−918.
(436) Li, S. Chapter 13 - Introduction to Electrochemical Reaction Engineering. In *Reaction Engineering*, Li, S., Ed.; Butterworth-Heinemann, 2017; pp 599−651.
(437) Britton, J.; Majumdar, S.; Weiss, G. A. Continuous flow biocatalysis. *Chem. Soc. Rev.* **2018**, *47* (15), 5891−5918.
(438) Arshi, S.; Madane, K.; Shortall, K.; Hailo, G.; Alvarez-Malmagro, J.; Xiao, X.; Szymańska, K.; Belochapkine, S.; Ranade, V. V.; Magner, E. Controlled Delivery of H_2O_2: A Three-Enzyme Cascade Flow Reactor for Peroxidase-Catalyzed Reactions. *ACS Sustain. Chem. Eng.* **2024**, *12* (28), 10555−10566.
(439) Oeggl, R.; Glaser, J.; von Lieres, E.; Rother, D. Continuous enzymatic stirred tank reactor cascade with unconventional medium yielding high concentrations of (*S*)-2-hydroxyphenyl propanone and its derivatives. *Catal. Sci. Technol.* **2021**, *11* (24), 7886−7897.
(440) Hartley, C. J.; Williams, C. C.; Scoble, J. A.; Churches, Q. I.; North, A.; French, N. G.; Nebl, T.; Coia, G.; Warden, A. C.; Simpson, G.; et al. Engineered enzymes that retain and regenerate their cofactors enable continuous-flow biocatalysis. *Nat. Catal.* **2019**, *2* (11), 1006−1015.
(441) Benítez-Mateos, A. I.; Roura Padrosa, D.; Paradisi, F. Multistep enzyme cascades as a route towards green and sustainable pharmaceutical syntheses. *Nat. Chem.* **2022**, *14* (5), 489−499.
(442) Kowalczykiewicz, D.; Przypis, M.; Mestrom, L.; Kumpf, A.; Tischler, D.; Hagedoorn, P.-L.; Hanefeld, U.; Jarzębski, A.; Szymańska, K. Engineering of continuous bienzymatic cascade process using monolithic microreactors - In flow synthesis of trehalose. *Chem. Eng. J.* **2022**, *427*, 131439.
(443) Lee, Y. S.; Lim, K.; Minteer, S. D. Cascaded Biocatalysis and Bioelectrocatalysis: Overview and Recent Advances. *Annu. Rev. Phys. Chem.* **2021**, *72*, 467−488.
(444) Chen, H.; Tang, T.; Malapit, C. A.; Lee, Y. S.; Prater, M. B.; Weliwatte, N. S.; Minteer, S. D. One-Pot Bioelectrocatalytic Conversion of Chemically Inert Hydrocarbons to Imines. *J. Am. Chem. Soc.* **2022**, *144* (9), 4047−4056.
(445) Weliwatte, N. S.; Chen, H.; Tang, T.; Minteer, S. D. Three-Stage Conversion of Chemically Inert *n*-Heptane to *α*-Hydrazino Aldehyde Based on Bioelectrocatalytic C-H Bond Oxyfunctionalization. *ACS Catal.* **2023**, *13* (1), 563−572.
(446) Dong, F.; Chen, H.; Malapit, C. A.; Prater, M. B.; Li, M.; Yuan, M.; Lim, K.; Minteer, S. D. Biphasic Bioelectrocatalytic Synthesis of Chiral *β*-Hydroxy Nitriles. *J. Am. Chem. Soc.* **2020**, *142* (18), 8374−8382.
(447) Yeom, S.-J.; Le, T.-K.; Yun, C.-H. P450-driven plastic-degrading synthetic bacteria. *Trends Biotechnol.* **2022**, *40* (2), 166−179.
(448) Oiffer, T.; Leipold, F.; Süss, P.; Breite, D.; Griebel, J.; Khurram, M.; Branson, Y.; de Vries, E.; Schulze, A.; Helm, C. A.; et al. Chemo-Enzymatic Depolymerization of Functionalized Low-Molecular-Weight Polyethylene. *Angew. Chem., Int. Ed.* **2024**, *63* (50), No. e202415012.
(449) Pinaud, B. A.; Benck, J. D.; Seitz, L. C.; Forman, A. J.; Chen, Z.; Deutsch, T. G.; James, B. D.; Baum, K. N.; Baum, G. N.; Ardo, S.; et al. Technical and economic feasibility of centralized facilities for solar hydrogen production via photocatalysis and photoelectrochemistry. *Energy Environ. Sci.* **2013**, *6* (7), 1983−2002.
(450) Cox, C. R.; Lee, J. Z.; Nocera, D. G.; Buonassisi, T. Ten-percent solar-to-fuel conversion with nonprecious materials. *Proc. Natl. Acad. Sci. U. S. A.* **2014**, *111* (39), 14057−14061.
(451) Shaner, M. R.; Atwater, H. A.; Lewis, N. S.; McFarland, E. W. A comparative technoeconomic analysis of renewable hydrogen production using solar energy. *Energy Environ. Sci.* **2016**, *9* (7), 2354−2371.

https://doi.org/10.1021/acs.chemrev.5c01010
Chem. Rev. 2026, 126, 4857−4899

(452) Fehr, A. M. K.; Deutsch, T. G.; Toma, F. M.; Wong, M. S.; Mohite, A. D. Technoeconomic Model and Pathway to < $2/kg Green Hydrogen Using Integrated Halide Perovskite Photoelectrochemical Cells. *ACS Energy Lett.* **2023**, *8* (12), 4976−4983.
(453) Wu, S.; Snajdrova, R.; Moore, J. C.; Baldenius, K.; Bornscheuer, U. T. Biocatalysis: Enzymatic Synthesis for Industrial Applications. *Angew. Chem., Int. Ed.* **2021**, *60* (1), 88−119.
(454) Bommarius, A. S. Total Turnover Number - a Key Criterion for Process Evaluation. *Chem. Ing. Technol.* **2023**, *95* (4), 491−497.
(455) Adams, J. D.; Clark, D. S. Techno-Economic Assessment of Electromicrobial Production of *n*-Butanol from Air-Captured CO_2. *Environ. Sci. Technol.* **2024**, *58* (17), 7302−7313.

https://doi.org/10.1021/acs.chemrev.5c01010
Chem. Rev. 2026, 126, 4857−4899